Feasibility study of a hot carrier photovoltaic device

Arthur Le Bris

Thèse de doctorat de l'École Centrale Paris

ED 287 – Sciences pour l'Ingénieur

présentée par

Arthur LE BRIS

pour l'obtention du grade de docteur de l'École Centrale Paris

Etude de faisabilité de dispositifs photovoltaïques à porteurs chauds : conception, modélisation, caractérisation

dirigée par Jean-François Guillemoles et Jean-Jacques Greffet, et soutenue le 09 septembre 2011 devant le jury composé de :

Pr. X. Marie	Rapporteur
Pr. N. Ekins-Daukes	Rapporteur
Pr. Y. Okada	Examinateur
Pr. O. Durand	Examinateur
Pr. JF. Guillemoles	Directeur de thèse
Pr. JJ. Greffet	Directeur de thèse

Les portes de l'avenir sont ouvertes à ceux qui savent les pousser.

Coluche

Remerciements

Je remercie bien évidemment en premier lieu Jean-François Guillemoles pour m'avoir encadré pendant cette thèse, présent (presque) tous les jours et fournissant toujours des idées, parfois trop nombreuses mais toujours pertinentes, pour comprendre et avancer. Merci également à Jean-Jacques Greffet pour avoir co-encadré cette thèse d'un peu plus loin, mais avec une clairvoyance qui ne s'est jamais démentie. Viennent ensuite Daniel Lincot, directeur de l'Institut de Recherche et Développement sur l'Énergie Photovoltaïque, et son prédécesseur à la tête de l'IRDEP Olivier Kerrec, qui m'ont accueilli dans leur équipe.

Je tiens à remercier Xavier Marie, Ned Ekins-Daukes, Yoshitaka Okada et Olivier Durand pour m'avoir fait l'honneur de participer au jury de cette thèse, avec une mention spéciale au Pr Okada, qui a fait le déplacement depuis le Japon pour l'occasion. Je suis également très reconnaissant envers Gavin Conibeer qui est passé par Paris entre deux avions pour assister à ma présentation.

Remercions également les différents laboratoires partenaires du projet Très Haut Rendement et Innovations pour le PhotoVoltaïque (THRIPV) (par ordre alphabétique) : Institut d'Électronique du Sud (IES), Institut Lavoisier de Versailles (ILV), Laboratoire Charles Fabry de l'Institut d'Optique (LCFIO), Laboratoire de Chimie de la Matière Condensée de Paris (LCMCP), Laboratoire de Génie Électrique de Paris (LGEP), Laboratoire de Photonique et Nanostructures (LPN). Je remercie en particulier Philippe Christol, Ruben Esteban, Stéphane Collin et Clément Colin, pour leur implication personnelle et l'utilisation que j'ai pu faire de leurs résultats.

Je souligne également le rôle des bailleurs de fond que furent l'Agence Nationale de la Recherche (ANR), qui a financé le projet THRIPV, et l'Université de Standford, à l'origine du Global Climate and Energy Project (GCEP), qui m'ont permi de manger pendant trois ans, et même un peu plus, et qui m'ont offert l'opportunité de communiquer mes travaux dans des endroits tels que Valence, Honolulu, Hambourg, Seattle ou Nice. Merci aussi au CNRS et à EDF qui ont participé aux frais d'une manière ou d'une autre, même si je n'ai jamais trop compris qui payait

quoi dans l'histoire.

Ce travail a également bénéficié de l'aide précieuse de mes collègues ou ex-collègues de l'IRDEP, notamment de Pär Olsson, Huang Lun Mei, et Sana Laribi pour les questions de modélisation et autres problèmes informatiques, et de Laurent Lombez quand il a fallu entrer malgré tout dans les laboratoires. Au delà des relations strictement professionnelles, je tiens à remercier l'ensemble du personnel de l'IRDEP pour l'ambiance chaleureuse qui y règne. Malgré mon interaction limitée avec le genre humain durant ces trois ans (les plus bienveillants diront que j'ai fait preuve d'une certaine autonomie), j'ai réussi à établir des contacts avec quelques personnes. Citons pour l'exemple, de manière non exhaustive et dans le désordre : Jean R., pourvoyeur de pépites musicales, Servane H., meilleure cliente de la SNCF, Zac(harie) J. (prononcez Y.), meilleur client pour mes contrepéteries, Marie J. et Fredérique D., binôme inséparable et grandes prétresses du vide, Myriam P., à la gifle redoutable et redoutée. Merci à eux pour les bons moments passés sur l'île de Chatou, ou en conférence, ou ailleurs, pour avoir supporté mon rigorisme exarcerbé à la coinche et subi mon humour trop souvent désastreux, mais bon, on est pas toujours au top.

J'aimerais aussi remercier ceux qui, d'un peu plus loin, ont contribué à mes travaux : Frédéric Aniel et Eric Téa de l'Institut d'Électronique Fondamentale (IEF), Ned Ekins-Daukes, Markus Führer, Louise Hirst du Quantum Photovoltaic Group à l'Imperial College à Londres, Gavin Conibeer de l'University of New South Wales (UNSW), Tim Schmidt et Raphael Claddy de l'Université de Sydney.

Un grand merci à Jacqueline Destombes et Claire Vialette, et plus récemment Nicole Jacob, pour leur aide sur les questions administratives à l'IRDEP. Merci également à Géraldine Carbonel et Catherine Lhopital qui, malgré la distance et un manque d'appetence de ma part pour la paperasse en général, ont su me guider dans les procédures administratives de l'École Centrale.

Je signale également l'implication de ma soeur Charlotte, qui a réalisé certaines des figures que vous trouverez dans ces pages, et qui m'ont vallu des commentaires admiratifs partout où je les ai montrées.

Enfin, je remercie tous ceux qui ont assisté à ma soutenance, en particulier mes parents et mon frère pour leur aide dans la préparation du buffet qui l'a suivie, ainsi que Servane, Anne et Thibaud pour leurs contributions patissières, et tous ceux qui m'ont soutenu d'une manière ou d'une autre, famille ou amis, pendant la durée de ma thèse.

Résumé

La cellule photovoltaïque à porteurs chauds se caractérise par une population électronique hors équilibre thermique avec le réseau, ce qui se traduit par une température électronique supérieure à la température du matériau. Il devient alors possible de récupérer non seulement l'énergie potentielle des porteurs, mais également leur énergie cinétique, et donc d'extraire un surcroît de puissance qui n'est pas exploitée dans des cellules conventionnelles. Cela permet d'atteindre des rendements potentiels proches de la limite thermodynamique. L'extraction des porteurs hors équilibre se fait au moyen de membranes sélectives en énergie afin de limiter les pertes thermiques.

Dans cette thèse, l'influence de la sélectivité des contacts sur les performances de la cellule est analysée par des simulations de rendement. Il apparaît que ce paramètre est moins critique qu'annoncé dans la littérature, et que des rendements élevés sont possibles avec des contacts semi-sélectifs, permettant l'extraction de porteurs au dessus d'un seuil d'énergie. De tels contacts sont non seulement beaucoup plus facilement réalisables en pratique que des contacts sélectifs, mais sont également plus compatibles avec les densités de courant élevées qui sont attendues dans de tels dispositifs.

Une méthodologie expérimentale est également proposée pour analyser la vitesse de thermalisation des porteurs hors équilibre. Des porteurs sont photogénérés par un laser continu et leur température en régime stationnaire est sondée par photoluminescence en fonction de la densité de puissance excitatrice. Un modèle empirique est obtenu reliant la puissance dissipée par thermalisation à la température électronique. Ce modèle est ensuite utilisé pour simuler le rendement de cellules présentant une thermalisation partielle des porteurs.

Enfin, un rendement de cellule réaliste présentant une absorption non idéale, une vitesse de thermalisation mesurée sur des matériaux réels et des contacts semi-sélectifs est calculé. Il ressort qu'une augmentation substantielle de rendement est possible en comparaison d'une simple jonction ayant le même seuil d'absorption, mais que la vitesse de thermalisation observée est néanmoins trop élevée pour

permettre de dépasser les records de rendement actuels. Des idées sont proposées afin d'améliorer les performances des structures étudiées.

Abstract

A hot carrier solar cell is characterized by a carrier population in thermal non equilibrium with the lattice, that translates into carriers having a temperature higher than the material temperature. It then becomes possible to collect not only the carrier potential energy but also their kinetic energy, and thus to extract an additional power that is not used in conventional solar cells. This enables to reach a potential efficiency close to the thermodynamical limit. The extraction of carriers is made through energy selective membranes in order to reduce the heat loss.

In this thesis, the impact of contact selectivity on the cell behaviour is investigated by simulating its efficiency. It appears that this parameter is not as crucial as what was said in the literature, and that a high efficiency is indeed possible with semi-selective contacts allowing carrier extraction above an energy threshold. Such contacts would not only be much easier to fabricate in practice, but are also more compatible with the high current densities that are expected in such devices.

An experimental method is also proposed to determine the non equilibrium carrier cooling rate. Carriers are photogenerated by a continuous wave laser and their temperature in steady state conditions is probed by photoluminescence as a function of the excitation power density. An empirical model is obtained that relates the power dissipation due to carrier thermalization to the electron temperature. Such model can then be used in a hot carrier solar cell model to take heat losses into account.

Finally, the efficiency of a realistic cell having non ideal absorption, a cooling rate measured on real materials and semi-selective contacts is simulated. It turns out that a substantial efficiency enhancement is possible compared to single junction cells with the same band gap, but that the cooling rate measured on samples is nevertheless too high to exceed today's efficiency records. Ideas are proposed to improve the performance of the structure under investigation.

Contents

List of Figures

List of Tables

Introduction

Motivation

Electricity from photovoltaics has a double advantage: an abundant, renewable and free energy source, and a low environmental impact. However, it is so far underexploited because of high production costs compared to other electricity production technologies (fossil and nuclear). Economic competitiveness is the key issue to enable a massive deployment of photovoltaic energy. It is related to the system production cost in €/m^2 and to the module efficiency.

In figure 1, different technologies of solar cells are represented in a production cost - cell efficiency map. A first generation of bulk silicon solar cells had decent efficiency ranging from 18 to 23% (as modules [1]) but high production cost. This is mainly due to the material consumption of such technology: silicon having an indirect band gap, a thickness of 200 μm is necessary to absorb light efficiently. The waste of material in the standard production process (sawing of Si wafers from a Si ingot) is also a major limitation. A second generation composed of thin film solar cells using new materials (for instance CdTe and Cu(In,Ga)Se_2 or amorphous silicon) was developed with a slightly lower efficiency (between 11 and 15% module efficiency depending on the material [1]) but a strongly reduced production cost. Cost reduction was achieved using a reduced absorbing layer thickness down to about 2 μm. These technologies have successfully brought energy production cost in the economic competitiveness range. CdTe based thin film cells have already reached the targeted 1 €/W, and CIGS cells are following the same trend.

However, further improvement on the module production cost is difficult. Half of the module final cost is not related to the cell fabrication but comes from all components other than the photovoltaic cell, known as balance of system (switches, wiring, inverters, batteries, support racks, land...), so further cost reduction in the cell fabrication would have a minor impact on the overall eletricity cost .Thus, the kWh cost reduction implies efficiency enhancement rather than production cost reduction. One can see on figure 1 that the conventional devices have an intrinsic

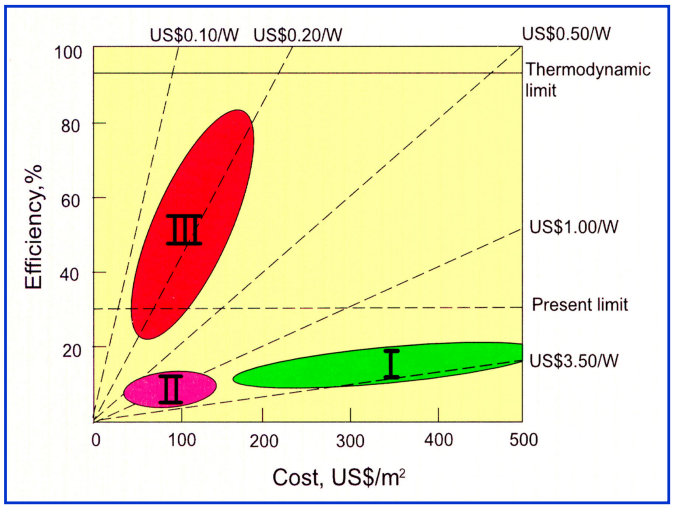

Figure 1: Efficiency - production cost map of different solar cell technologies: first generation (bulk silicon, green), second generation (thin films,pink) and third generation (red). The third generation would allow efficiency above the present 31% limit. The thermodynamical limit is 86%. Dashed lines represent different values of the energy production cost. The competitiveness threshold of 1$/W is attained in the 2nd generation area.

efficiency limit of 31%, which does not leave much room for improving solar cell efficiencies. However, the thermodynamical limit of solar energy conversion into electricity is 86% [2, 3]. New concepts of cells, with a different working principle, can be proposed to overtake the present limit and approach the fundamental limit.

Overview of high efficiency solar cell concepts

The low efficiency limitation of conventional devices comes from the single band gap absorbing material that is poorly adapted to the polychromatic solar spectrum. With a single p-n junction solar cell, only the photons having the exact band gap energy are optimally converted. Those with lower energy are not absorbed, and those with higher energy only produce the energy of the band gap, the rest being lost as heat (see figure 2): the most energetic carriers are cooled down to the band edges in a process called carrier thermalization.

A quantitative determination of the different types of losses occuring in a single junction can be seen in figure 3. One notices that at the optimal band gap

(1.4 eV for a 31% efficiency), carrier thermalization and non absorption are each responsible for losses representing 30 and 20% of the incident power respectively.

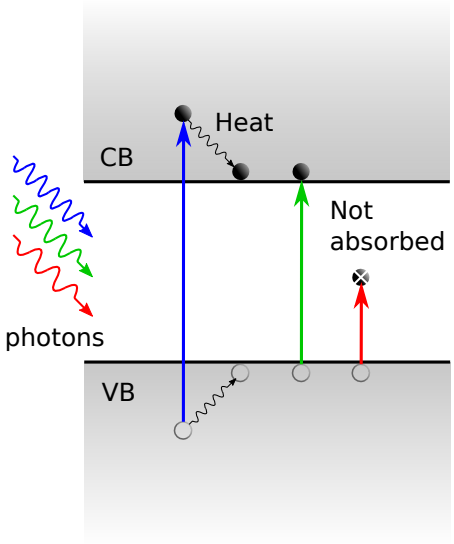

Figure 2: Loss mechanisms in a solar cell: low energy photons are not absorbed (red), high energy photons are absorbed with a part of the energy lost as heat (blue). Only photons with an energy matching the band gap can be efficiently converted (green).

There are therefore two general ideas to increase the efficiency: either increase the absorption, or reduce the thermalization losses. Several ideas have been proposed to achieve one or both of these two goals and are known as third generation photovoltaics [4]. The most promising ideas are listed in table 1. Concerning the absorption enhancement, one can cite (i) the up-conversion technique, that consists in converting the sub-band gap infrared part of the spectrum into visible light by photon addition [5], and (ii) intermediate band cells in which an intermediate band enables the absorption of sub-band gap photons without reduction of the voltage [6]. Thermalization losses can be reduced (i) in hot carrier solar cells [7], that is the subject of this work and will be treated extendedly below, (ii) using down-conversion techniques, that consists in converting one high energy photon into several lower energy photons that will promote several electron-hole pairs [8], or (iii) by multiple exciton generation, where one high energy photon promotes one high energy electron-hole pair that will then generate several lower energy electron-hole pairs by impact ionization [9, 10]. Finally, the concept of

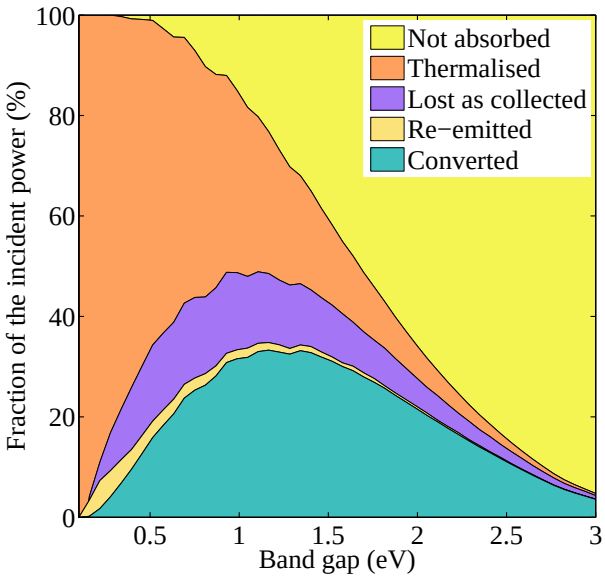

Figure 3: Efficiency and losses (non absorption, thermalization, extraction, and recombination) as a function of the absorbing material band gap, under AM1.5 incident spectrum. An optimal conversion efficiency of 31% is obtained for a 1.4 eV band gap.

multijunction combines both effects: by decomposing the solar spectrum into different spectral domains that are absorbed in different materials with well adapted band gaps, one can cover the whole spectral range (increase absorption), and the conversion is optimal in each material (reduce thermalization).

Among these concepts, only mutlijunction (or tandem) solar cells have been fully and successfully fabricated so far, with promising efficiency up to 41%. It consists in a stack of p-n junctions (sub-cells) with different band gaps, the higher band gap being on top and the lower band gap at the bottom. The UV part of the spectrum is absorbed in the front sub-cell while the visible and infrared part are transmitted and can be absorbed by the sub-cells underneath. All the sub-cells are interconnected in series so that they all produce the same current and the volage of the complete device is the sum of the voltages of the different sub- cells.

It has been demonstrated that an ideal multijunction cell made of an infinite stack of sub-cell, so that an exact match between the absorbed photon energy and the cell band gap is obtained at all photon energies, would give an efficiency of 86%

concept	principle
multijunction	decompose the solar spectrum into different spectral domains that are absorbed by distinct adapted material
up conversion	convert the infrared part of the spectrum into visible light with photon addition
down conversion	convert one UV photon into several visible photons
hot carrier solar cell	prevent carrier cooling and extract electrons with an energy higher than the bandgap
multiple exciton generation	generate several electron-hole pairs with one UV photon
intermediate band solar cell	absorb sub bandgap photons with an intermediate band to increase current

Table 1: List of 3$^{\text{rd}}$ generation photovoltaics ideas and cell concepts.

under maximal concentration (around 46000 suns), which is the thermodynamical limit of photovoltaic conversion. A detailed analysis of the potential efficiency depending on the number of sub-cells is available in [11], and show for instance achievable efficiencies above 60% with a triple junction.

The concept of intermediate band solar cell has been developed as an alternative to tandem cells, providing a potential efficiency similar to a triple junction, with only one absorbing material. An intermediate energy band is created in the band gap by the presence of a quantum dot array or a high concentration of dopants, for instance, and allow absorption from the valence band to the conduction band, but also from the valence band to the intermediate band and from the intermediate band to the conduction band (see figure 4). All electron-hole pairs generated contribute to the current, while the voltage is (hopefully) not affected by the presence of the intermediate band. The challenge is to maintain a high voltage and to prevent non radiative recombinations through the intermediate level.

Up conversion and down conversion are purely optical processes, and for that reason can be rather easily implemented on an existing cell by adding an optically active layer on the rear side for the up conversion or on the front side for down conversion. Up conversion consists in the absorption of two photons of energy $\hbar\omega < E_G$ that are normally not absorbed and subsequent emission of one photon with energy $2\hbar\omega > E_G$ that can be absorbed by the solar cell, E_G being the cell

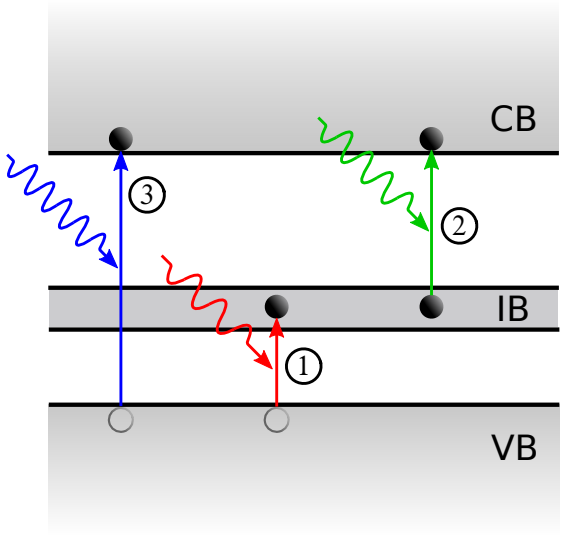

Figure 4: Schematic of an intermediate band solar cell. An intermediate energy band (IB) is created inside the band gap by the presence of a high density of impurities or coupled quantum dots. Low energy photons can be absorbed with transition from the valence band (VB) to the intermediate band ① or from the intermediate band to the conduction band (CB) ②, allowing absorption of sub-band gap photon and contributing to the current coming from the valence to conduction band transition ③.

band gap. It involves absorption by molecules or rare earth atoms with discrete energy levels, so up-converster materials generally present a narrow absorption energy range, which limits the efficiency enhancement potential. Down conversion is the reverse process with the absorption of one photon $\hbar\omega_1 > 2E_G$ and emission of two (or more) photons $\hbar\omega_2 \approx E_G$.

The hot carrier solar cell is an attractive concept that can provide very high potential efficiency, close to the thermodynamical limit, and comparable to an ideal infinite multijunction stack [7, 12], with a simplified architecture with only one absorber. The thermalization of photogenerated carriers is blocked and their kinetic energy in excess of the band gap is converted into potential energy to increase the voltage of the cell. As the kinetic energy is not lost, the band gap of the cell can be reduced compared to a standard p-n junction, and losses due to non absorption are also limited.

It has been discussed in principle, in the ideal case where carrier thermalization

is suppressed and minimal losses occur upon carrier extraction, but the question of its technological feasability has not been treated yet. Before an actual device can be fabricated, one have to wonder whether it can work in practice and under which conditions.

Outline

The purpose of this thesis is to discuss the feasability of the hot carrier solar cell concept in practical conditions. This work is organized in five chapters following this introduction.

The second chapter is a general introduction to the concept of hot carrier solar cell. The focus is put on two particular aspects of such concept: the extraction of carriers through energy selective contacts, and the thermalization of carriers. For each of these features, the impact of non ideality on the cell efficiency is quantitatively analyzed.

The question of selective contacts is treated in chapter 2. Non ideal selective contacts are introduced in a hot carrier solar cell model, and the influence of the contact selectivity is analysed and quantified.

Chapter 3 is an experimental study of carrier thermalization. Continuous wave photoluminescence is used to investigate the thermalization properties of test samples, and an empirical model for the carrier thermalization rate is proposed. This model is then introduced in a hot carrier solar cell model in chapter 4. The impact of partial carrier thermalization on the cell efficiency is quantitatively studied.

Finally, the potential efficiency of a realistic cell is determined in chapter 5, accounting for non ideal light absorption, carrier thermalization and extraction. A possible cell design is also proposed.

Bibliography

[1] M.A. Green, K. Emery, Y. Hishikawa, and W. Warta. Solar cell efficiency tables (version 37). *Prog. Photovolt: Res. Appl.*, 19:84 – 92, 2011.

[2] P. Würfel. *Physics of Solar Cells, From Principles to New Concepts.* Wiley-VCH, 2005.

[3] A. De Vos. *Thermodynamics of Solar Energy Conversion.* Wiley-VCH, 2008.

[4] M.A. Green. *Third generation photovoltaics - Advanced solar energy conversion.* Springer, 2003.

[5] T. Trupke, MA Green, and P. Würfel. Improving solar cell efficiencies by up-conversion of sub-band-gap light. *Journal of Applied Physics*, 92:4117, 2002.

[6] A. Luque and A. Martí. Increasing the efficiency of ideal solar cells by photon induced transitions at intermediate levels. *Phys. Rev. Lett.*, 78(26):5014–5017, Jun 1997.

[7] R.T. Ross and A.J. Nozik. Efficiency of hot-carrier solar energy converters. *Journ. Appl. Phys.*, 53:3813, 1982.

[8] T. Trupke, MA Green, and P. Würfel. Improving solar cell efficiencies by down-conversion of high-energy photons. *Journal of Applied Physics*, 92:1668, 2002.

[9] MC Hanna and AJ Nozik. Solar conversion efficiency of photovoltaic and photoelectrolysis cells with carrier multiplication absorbers. *Journal of Applied Physics*, 100:074510, 2006.

[10] V.I. Klimov. Detailed-balance power conversion limits of nanocrystal-quantum-dot solar cells in the presence of carrier multiplication. *Applied Physics letters*, 89(12):123118–123118, 2006.

[11] A.S. Brown. *Ultimate efficiency limits of multiple energy threshold photovoltaic devices*. PhD thesis, University of New South Wales, 2003.

[12] P. Würfel. Solar energy conversion with hot electrons from impact ionization. *Solar Energy Materials and Solar Cells*, 46:43, 1997.

Chapter 1

The hot carrier solar cell concept

1.1 Principles of the hot carrier solar cell

The concept of hot carrier solar cell was first introduced by Ross and Nozik [1]. In standard devices, the photon energy in excess of the threshold absorption energy is given to the photogenerated carrier population, and then to the lattice as heat, with only the band gap energy being converted as electrical work. If the carrier thermalization (thermal equilibration of carriers with the lattice) is suppressed, then the conversion of the total available energy into potential energy is possible and leads to higher conversion efficiency.

The energy distribution of the photogenerated carriers is, immediately after absorption, a non equilibrium distribution that depends on the energy distribution of the incident photons, and on the electron and hole effective masses and density of states. After absorption, the fate of the carrier distribution can be:

- Hot non-equilibrium: the carriers are not even in equilibrium among themselves, the carrier temperature can not be defined.
- Hot equilibrium: the carriers are in equilibrium among themselves but not with the lattice, resulting in a hot carrier population at $T_H > T_C$, where T_C is the temperature of the lattice
- Full thermalization: the common situation where carriers are at thermal equilibrium with the environment at ambient temperature.

The comparison between the thermalization rate (due to interactions with phonons, see section 1.3), the carrier-carrier scattering rate, and the carrier extraction rate (the rate at which carriers are removed from the system through contacts or by radiative recombination) will determine which one of the above cases applies. Typical time constants for these different mechanisms in III-V materials are given

Type of interaction	Characteristic time (s)
Carrier-Carrier scattering	$10^{-15} - 10^{-12}$
Carrier - Optical phonon interaction	$\geq 10^{-12}$
Optical phonon - Acoustic phonon interaction	$\sim 10^{-11}$
Auger recombination	$\sim 10^{-10}$
Radiative recombination	$\geq 10^{-9}$

Table 1.1: Typical time constants of various carrier interaction mechanisms in semiconductors, from [2].

in table 1.1, from reference [2].

The carrier-carrier scattering time constant is usually below the picosecond, and decreases with an increasing carrier density, while the time constant for the carrier-phonon interaction is of the order of the picosecond. Considering these time constants and without carrier extraction, the dynamics of the carrier after a pulsed monochromatic excitation is described in figure 1.1 from [3]. Immediately after absorption at $t = 0$, carriers are generated in a narrow energy range ②. Carrier-carrier scattering then occurs and carriers are redistributed in a hot thermal distribution ③-④, within a picosecond. This distribution is then cooled towards the lattice temperature because of interaction with phonons ⑤. Finally, carriers recombine with a sub-microsecond time constant ⑦.

If the excitation rate is higher than the thermalization rate, and lower than the carrier-carrier scattering rate, a steady state hot distribution can be established, and the carrier kinetic energy, which is usually lost as heat, can be used and contributes to the conversion efficiency.

Assuming such steady state hot carrier population is achieved, a specific care is required regarding carrier extraction. If the photogenerated electrons and holes are withdrawn towards metallic electrodes, where interactions with the lattice can not be avoided before they produce work in the external circuit, thermalization of excited carriers to the lattice temperature will occur, and with it, the carrier kinetic energy will be lost.

A specific cooling of the carriers with minimum heat losses ("adiabatic cooling") is necessary to cool down the carriers to the lattice temperature with production of chemical energy that appears as quasi-Fermi level splitting. In other words, the carriers kinetic energy has to be converted into potential energy, or voltage. This can be achieved with energy selective contacts that are described in 1.4 [4].

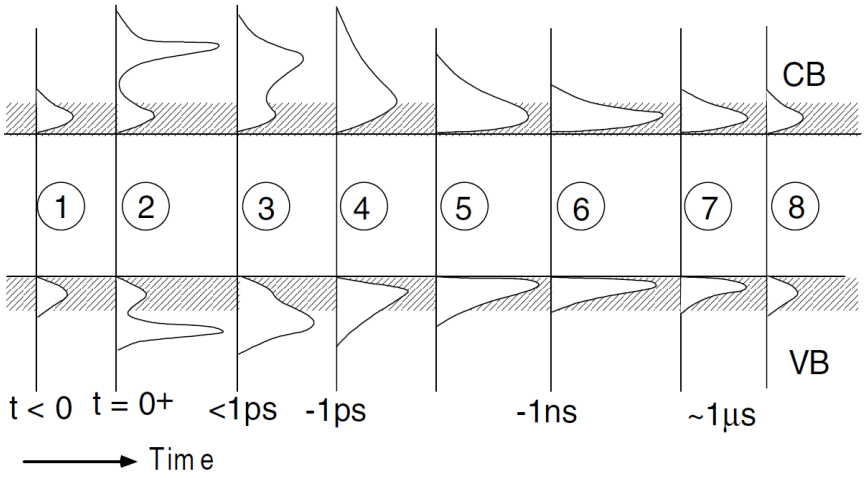

Figure 1.1: Time evolution of electron and hole populations after a laser excitation, from [3]

1.2 Detailed balance models and limit of efficiency

In order to evaluate the potential of the hot carrier solar cell concept, models have been developed to evaluate its maximal achievable efficiency. These models are based on a detailed balance approach that defines the electrical power output of a device as the difference between the power absorbed by the cell and the power lost in different types of loss processes.

The first non-empirical method to determine a solar cell efficiency limit was proposed by Trivich and Flinn [5]. In their analysis, they assumed that all photons above the band gap are absorbed, and that all electron-hole pairs photogenerated are collected with the energy of the band gap. In these conditions, the electrical power produced is the number of photons with energy higher than the band gap that are incident on the cell times the band gap energy and the efficiency is defined as:

$$\eta = E_G \frac{\int_{E_G}^{\infty} n(\hbar\omega) d\hbar\omega}{\int_0^{\infty} \hbar\omega n(\hbar\omega) d\hbar\omega} \tag{1.1}$$

where $n(\hbar\omega)$ is the photon current density and E_G is the absorber band gap energy.

This model predicts an optimal efficiency of 44% for an unconcentrated black body spectrum at 6000 K and with a 1.1 eV band gap absorber. However, it does not account for any recombination process, and for that reason is not a true

indicator of the efficiency limit of a solar cell.

In 1961, a model was proposed by Shockley and Queisser [6] where the current is not only determined by photon absorption, but is equal to the difference between absorption and radiative recombination.

$$J = q\left(\dot{N}_{abs} - \dot{N}_{em}(V)\right) \tag{1.2}$$

where J is the electric current density in A/m^2, N_{abs} is the absorbed photon current density in $m^{-2}s^{-1}$, $N_{em}(V)$ is the emitted photon current density in $m^{-2}s^{-1}$ depending on the terminal voltage V of the device, and q is the charge of an electron.

Assuming the sun emits a black body spectrum at the sun temperature T_S, the photon flux incident on the cell per unit area, per unit solid angle and per photon energy is:

$$dN_{ph} = \frac{1}{4\pi^3\hbar^3c^2}\frac{E^2}{\exp\left(\frac{E}{\mathrm{k_B}T_S}\right)-1}\cos\theta\sin\theta d\theta d\varphi dE \tag{1.3}$$

where E is the photon energy, θ is the inclination angle, and φ is the azimuthal angle.

Integrating over directions and energy, the absorbed photon current density is then given by Planck's law:

$$\dot{N}_{abs} = \frac{f}{4\pi^2\hbar^3c^2}\int_{E_G}^{\infty}\frac{E^2dE}{\exp\left(\frac{E}{\mathrm{k_B}T_S}\right)-1} \tag{1.4}$$

where f is a geometrical factor that accounts for the solid angle for photoabsorption. If incident photons comes from a cone with half angle θ_{max}, f is given by: $f = 2\pi\int\cos\theta\sin\theta d\theta = \pi\sin^2\theta_{max}$. It is 1 for maximally concentrated radiation ($\theta_{max} = \pi/2$) and 6.7×10^{-4} for non-concentrated light (the sun is viewed from a solid angle $\Omega = 6.8\times10^{-5}$). The absorptivity is assumed to be one above the band gap energy, and zero below.

The photon current density emitted by the cell with applied voltage V and at the cell temperature T_C is defined as:

$$\dot{N}_{em}(V) = \frac{np}{n_i^2}\dot{N}_0 = \exp\left(\frac{qV}{\mathrm{k_B}T_C}\right)\dot{N}_0 \tag{1.5}$$

where n and p are the electron and hole densities in the cell, and n_i is the equilibrium carrier density. $\dot{N}_0$ is the equilibrium black body emission at temperature

T_C, and is defined, for emission in a 2π solid angle, by:

$$\dot{N}_0 = \frac{1}{4\pi^2\hbar^3c^2}\int_{E_G}^{\infty}\frac{E^2dE}{\exp\left(\frac{E}{k_B T_C}\right)-1} \tag{1.6}$$

For a cell temperature $T_C = 0$ K, radiative recombinations become negligible and the open-circuit voltage is equal to the band gap. This model gives the same results as the Trivich-Finn model. However, for positive cell temperatures, radiative recombinations lead to a reduced current and open-circuit voltage and a lower efficiency. At 300 K, the efficiency limit given by the Shockley-Queisser model under unconcentrated sun light is 31% for a band gap $E_G = 1.4$ eV. The efficiency limit for fully concentrated sun light ($\Omega = \pi$) is 41% with a 1.1 eV band gap.

If non-radiative recombinations occur, the current-voltage characteristic is given by:

$$J = \frac{1}{4\pi^2\hbar^3c^2}\int_{E_G}^{\infty}\left[\frac{fE^2}{\exp\left(\frac{E}{k_B T_S}\right)-1} - \frac{\exp\left(\frac{qV}{k_B T_C}\right)}{\rho(E)}\frac{E^2}{\exp\left(\frac{E}{k_B T_C}\right)-1}\right]dE \tag{1.7}$$

where $\rho(E)$ is the fraction of the total recombination that is radiative, $\rho(E) \leq 1$ ($\rho(E) = 1$ in Shockley-Queisser approach).

The next major development in the detailed balance theory was brought by Würfel [7]. He provided a more detailed argument regarding the expression of the radiation emitted by the cell. By analysing the balance between absorption, spontaneous emission and stimulated emission, he was able to relate the emitted photon current to the internal electron-hole gas chemical potential (or quasi-Fermi level splitting), and therefore to the ouput voltage. The following expression was obtained for the emitted photon current density:

$$\dot{N}_{em}(V) = \frac{1}{4\pi^2\hbar^3c^2}\int_{E_G}^{\infty}\frac{E^2}{\exp\left(\frac{E-qV}{k_B T_C}\right)-1}dE \tag{1.8}$$

In all the above models, the carriers were supposed to be at thermal equilibrium with the lattice. In 1982, Ross and Nozik [1] imagined a device where the carriers thermally equilibrate among themselves, but are thermally insulated from the lattice, and are therefore characterized by a temperature $T_H > T_C$. Equation 1.2 becomes:

$$J = \frac{q}{4\pi^2\hbar^3c^2}\int_{E_G}^{\infty}\left[f\frac{E^2}{\exp\left(\frac{E}{k_B T_S}\right)-1} - \frac{E^2}{\exp\left(\frac{E-\Delta\mu_H}{k_B T_H}\right)-1}\right]dE \tag{1.9}$$

Here, electrons in the conduction band and holes in the valence band are assumed to be thermally equilibrated at T_H and have a chemical potential μ^e and μ^h respectively. $\Delta\mu_H = \mu^e - \mu^h$ is the chemical potential difference between electron and hole gases. A pathway is introduced for carrier extraction, where electrons and holes are extracted at specific energy levels E^e and E^h, and the energy extracted per electron-hole pair is $E_{ext} = E^e - E^h$. Such an extraction pathway provides a limited interaction between the outside world and the hot system, that continues to be thermally insulated. In those conditions, a relation between the internal chemical potential $\Delta\mu_H$ and the output voltage V can be found.

Let us consider the variation of energy of the electron plasma in the hot absorber: $dU_A^e = T_H dS_A^e + \mu^e dN_A^e$, where subscript A refers to the absorber and superscript e refers to electrons, U is the internal energy, S is the entropy, and N is the number of particles. The same equation is written for holes, with superscript h. A similar equation is now written for the variation of energy in electrode n where electrons are injected: $dU_E^e = T_C dS_E^e + \mu^n dN_E^e$, where subscript E refers to the electrode, T_C is the lattice temperature and μ^n is the Fermi level in electrode n. Here again the same equation is written for holes with superscript h and with μ^p as the Fermi level in electrode p.

The extraction of one electron-hole pair from the absorber towards the electrodes means that $dN_A^h = -dN_A^e = 1$ (injection of an electron on the p side, withdrawal on the n side). The corresponding energy variation can be written:

$$\Delta U_A = \Delta U_A^e + \Delta U_A^h = T_H(\Delta S_A^e + \Delta S_A^h) - (\mu^e - \mu^h) = T_H \Delta S_A - \Delta\mu_H \quad (1.10)$$

This energy variation is $\Delta U_A = -E_{ext}$, so the entropy variation in the absorber associated to the extraction of one electron-hole pair is

$$\Delta S_A = -\frac{1}{T_H}\left(E_{ext} - \Delta\mu_H\right) \quad (1.11)$$

From the point of view of the electrode distributions, the extraction of one electron-hole pair corresponds to $dN_E^e = -dN_E^h = 1$ and to an energy variation $\Delta U_E = E_{ext}$, so the entropy variation is:

$$\Delta S_E = \frac{1}{T_C}\left(E_{ext} - qV\right) \quad (1.12)$$

with the voltage V being defined as $V = (\mu^n - \mu^p)/q$.

An isentropic extraction of carriers means that $\Delta S_E = -\Delta S_A$, so the output voltage can be expressed:

$$qV = E_{ext}\left(1 - \frac{T_C}{T_H}\right) + \Delta\mu_H \frac{T_C}{T_H} \quad (1.13)$$

Equation 1.9 is not sufficient to determine the current voltage characteristic because of the two unknowns $\Delta\mu_H$ and T_H. An additional equation describing the energy balance in the system is required. The absorbed and emitted energy currents are simply obtained from the photon current expressions by mutliplying the integrand by the energy E of the photons. The energy current extracted through the utilization pathway is the charge current J multiplied by the extracted energy per electron-hole pair E_{ext}.

$$J.E_{ext} = \frac{q}{4\pi^2\hbar^3c^2}\int_{E_G}^{\infty}\left[E\left(f\frac{E^2}{\exp\left(\frac{E}{k_B T_S}\right)-1} - \frac{E^2}{\exp\left(\frac{E-\Delta\mu_H}{k_B T_H}\right)-1}\right)\right]dE \quad (1.14)$$

Combining equations 1.9 and 1.14, the current is determined for a given value of E_G, E_{ext} and f. The voltage is then found from equation 1.13. The current-voltage characteristics and the cell efficiency are obtained, with a predicted optimal limit of 66% under AM1.5 illumination and a band gap approaching zero.

In this model, particle conservation was assumed, which means that only radiative recombinations are considered, but also that Auger recombination and impact ionization are neglected. In 1997, Würfel [4] proposed an other approach where Auger recombination and impact ionization are assumed to be dominant over all other recombination processes and faster than carrier extraction. In these conditions, the electrons and holes are at chemical equilibrium ($\Delta\mu_H = 0$) and are described by a Fermi-Dirac distribution with a temperature $T_H > T_C$. The limit of efficiency in that case is 53% under non concentrated 6000 K black body illumination, and 85% under full concentration.

1.3 The mechanisms of carrier thermalization

In the above determination of achievable efficiencies, it was stated that the electron-hole plasma was thermally insulated from the environment, which is not the case in practical conditions. The carriers thermalize with the environment mainly because of interactions with the lattice vibration modes. This process usually occurs in few picoseconds, which is much faster than the carrier extraction time in conventional cells. In order to allow a hot carrier population regime, the carriers have to be extracted before they thermalize, which means that the thermalization rate has to be controlled and reduced, but also that the extraction time should be shorter than the thermalization time [8].

Model	Ω_S	η_{max}	$E_{G_{opt}}$	T_H
Conventional single junction	6.8×10^{-5}	31%	1.4 eV	300 K
	2π	41%	1.1 eV	300 K
Particle conservation	6.8×10^{-5}	66%	0 eV	3600 K
	2π	86%	0 eV	4200 K
Impact ionization	6.8×10^{-5}	53%	0.9 eV	348 K
	2π	85%	0 eV	2470 K

Table 1.2: Comparison of limits of efficiency (η_{max}), optimal band gap ($E_{G_{opt}}$), and carrier temperature in optimal operating conditions (T_H) for conventional single junction and different hot carrier models under unconcentrated ($\Omega_S = 6.8 \times 10^{-5}$) and fully concentrated ($\Omega_S = 2\pi$) 6000 K black body spectrum.

1.3.1 Carrier-carrier scattering

Immediately after absorption, the photogenerated electron-hole plasma distribution is not an equilibrium Fermi-Dirac distribution. In the case of a laser exciting the carriers, for instance, electrons and holes are generated in a very narrow region in the energy-momentum space. This population, in chemical and thermal disequilibrium with the environment, is subject to different scattering processes that brings it to equilibrium.

Intraband scattering

The intraband scattering comes from Coulomb elastic interaction between free carriers [9, 10]. Electron-electron, electron-hole and hole-hole scattering occur with exchange of energy and momentum to more uniformly distribute the excess kinetic energy amongst carriers. Here the carriers stay in their respective energy band (no recombination), and this interaction is called intraband scattering.

Considering this process, the free carrier population naturally evolves towards a Fermi-Dirac distribution defined by a temperature that is common to electron and holes (thermal equilibrium), that can be much higher than the environment temperature, since no interaction with the lattice has occured. In the case of different time constants for electron-hole interaction and electron-electron or hole-hole interaction, different temperatures for electrons and holes can be reached [11].

It is a very fast two-particles process that depends quadratically on the carrier

density. Its typical time scale is the femtosecond.

Interband scattering

The collisions between carriers can also result in electron-hole pair generation or recombination in non-radiative processes. Two cases are possible (see figure 1.2):

- Auger recombination: an electron and a hole recombine, and give their energy to a third free carrier (electron or holes).
- Impact ionization: a high energy free electron (or hole) gives a part of its energy to produce one exciton.

Here again the free carrier plasma total energy is conserved, but the number of particles is not. It is a three particles process, and therefore less probable than intraband scattering. A typical time constant is 100 ps (table 1.1). It also depends on the band gap, and can become very efficient in small band gap materials. The exchange between electrons and holes results in an equilibration of electron and hole chemical potentials. In the limit of very fast Auger recombination and impact ionization, electrons and holes can be considered to be in chemical equilibrium with quasi Fermi level splitting approaching zero [4, 12].

1.3.2 Electron/hole-phonon interaction

General case

The electron-hole plasma that is photogenerated is initially hot (electron/hole with energy far above/below the conduction/valence band edge) immediately after absorption. This excess kinetic energy is lost mainly by phonon emission that comes from interaction between the charge carriers with the ions of the lattice. This process brings the excited carrier population to thermal equilibrium with the lattice within a few picoseconds and can be probed by time resolved photoluminescence spectroscopy experiments (see chapter 3).

The momentum conservation condition in a scattering event implies that carriers are coupled primarily with long wavelength (small wave vector) phonons. There are four types of zone center phonons in diamond- and zinc-blende-type semiconductors: transverse acoustic (TA), longitudinal acoustic (LA), transverse optical (TO), and longitudinal optical (LO) phonons, involving different types of interaction [9, 10].

- deformation potential interaction: in the case of an acoustic phonon, the atomic displacement corresponds to a deformation of the crystal that changes the electronic energy levels. This change in electronic energies induced by

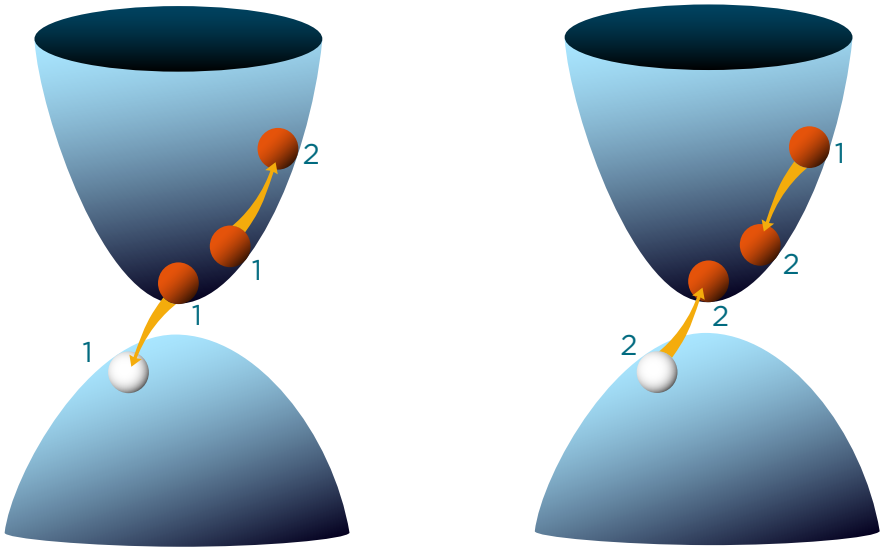

(a) Auger recombination

(b) Impact ionization

Figure 1.2: Schematic of Auger recombination (a) and impact ionization (b). In Auger recombination, the three carriers at initial time (1) end up in one carrier at final time (2) having all the energy. Impact ionization is the opposite process with one initial energetic electron generating an additional electron-hole pair

static distortion of the lattice is described by a parameter called the deformation potential. Such lattice deformation affects all energy bands, so electron and holes are coupled in the same way. It is independent of the phonon wavevector and is therefore a short range interaction.

- piezoelectric interaction: an acoustic phonon is associated with an oscillating strain that, in noncentrosymmetric crystals, can induce a macroscopic electric polarization field. This, in turn, couple to a charge carrier. This phenomenon is known as the piezoelectric effect. The electron-acoustic-phonon interaction that results from this effect is a long wavelength interaction, thus a long range interaction.
- electron-optical-phonon deformation potential interaction: an optical phonon involves relative displacement of atoms that can be seen as microscopic distortion within the primitive unit cell. In non polar semiconductor, such distortion affects the energy levels by changing bond length and bond angles. It is the analog to the deformation potential interaction for acoustic phonons.
- Fröhlich interaction: in a polar semiconductor, a longitudinal optical mode involves an opposite displacement of anions and cations in the primitive cell, that creates an electromagnetic fields interacting with the charge carriers. It is analog to the piezoelectric effect with acoustic phonons. It is a long range interaction, specific to polar semiconductors such as III-V compounds.

Interaction with small wavelength (zone edge) phonons are also possible through intervalley electron-phonon interaction. A zone edge phonon can scatter an electron from a band minimum at the zone center to a band minimum at a zone edge. For indirect semiconductors, such as silicon, this can play an important role in optical absorption. Also, the high energy electrons in a hot carrier distribution can be scattered to band minima at zone edges even in direct semiconductors. It can be avoided with a well chosen material with X and L band minima high enough to prevent such intervalley scattering.

III-V compounds

In the following analysis, the focus will be put on the case of GaAs, which is an emblematic case of a polar semiconductor, and has been widely studied.

The intensities of the different interactions depend on the phonon occupation number, and therefore on the lattice temperature. At low temperature ($<$40 K), electrons are not sufficiently energetic to excite LO phonons. Only acoustic phonons can be generated and carrier-phonon interactions are dominated by piezoelectric interaction and acoustic deformation potential [13]. For temperature

exceeding $\sim$ 40 K, the Fröhlich interaction becomes dominant and other types of interaction becomes negligible.

This means that at ambient temperature, the electron-hole plasma loses its energy mainly by emission of LO phonons. The coupled modes have a small wave vector because of the wave vector dependant Frölich matrix element. Thus, the carrier cooling process results in the generation of a large number of zone center LO phonons, which can result in a unequilibrated LO phonon population [14, 11].

The caracteristic time of this Fröhlich interaction is typically the picosecond. Experimental studies reported a time constant for electron-LO-phonon interaction of a few ps in GaAs (4 ps in [15], $\geq$ 1ps in [2]). A value close to 1 ps (depending on the carrier temperature) was theoretically determined in [16] in GaAs at 300 K. The calculated value is slightly higher in GaSb ($\sim$ 2ps).

1.3.3 Electron-hole plasma dynamic

An insight into the dynamic of an electron-hole plasma after photoexcitation and subsequent relaxation in a semiconductor is obtained by considering the case of a semiconductor illuminated by a short, high intensity pulse of light with a narrow spectral range such as from a laser [3].

The photogenerated plasma is subject to a succession of scattering event that brings the initial distribution in chemical and thermal disequilibrium to a Fermi-Dirac fully equilibrated population (see figure 1.1). In the first femtoseconds following light absorption, a thermal Fermi-Dirac distribution is established thanks to carrier-carrier intraband scattering. This distribution is however still at thermal and chemical disequilibrium with the lattice. Then, interaction with the lattice occurs in a picosecond time scale resulting in the cooling of the carriers to reach thermal equilibrium with the environment. Finally, interaction with photons through radiative recombination occurs in a nanosecond time scale, with reduction of the quasi Fermi level splitting, until the initial equilibrated distribution is reached.

The carrier cooling rate has been investigated using time resolved photoluminescence. It was observed, when the injection level was varied, that the electron energy loss rate was reduced with an increase of the carrier density in the material. Two explanations were proposed for such an effect:

- a screening of the photogenerated-electron-induced electric field by free carriers that weakens the electron-LO-phonon interaction and reduces the phonon emission rate
- the formation of a "hot" LO phonon population that is thermally equilibrated with electrons and not with the lattice. The absorption of phonon becomes as probable as the emission, and the energy loss process is blocked.

Only the second explanation was proven to be in quantitative agreement with experiments.

1.4 Energy selective contacts for carrier extraction

1.4.1 Role of selective contacts

In the paper by Ross and Nozik [1] that first introduced the concept of hot carrier solar cells, the extraction of carriers was not treated in details. An extraction pathway was considered that removes carriers at an energy U and returns them at another energy L where $U - L = E_{ext}$ is the energy extracted from the sytem per electron-hole pair. It was simply stipulated that the hot carrier system had to interact with the outside world in a very limited way to ensure its thermal insulation. Specific features of such extraction mechanisms, or its technological feasibility was not discussed.

The withdrawal of electron-hole pairs was first treated by Würfel [4]. Considering that the carrier thermalization in the electrodes could not be avoided, a cooling mechanism is necessary when extracting excited carriers towards the contacts, to bring them to the lattice temperature without entropy generation and prevent heat dissipation. He proposed a sytem of membranes allowing carrier transport in a narrow energy range $\delta E \ll kT$, that allow such isentropic cooling. In these membranes, all carriers have the same energy, and no energy loss process can occur at constant carrier concentration. They allow an isentropic cooling of electrons to the lattice temperature with production of chemical potential. The carrier kinetic energy (temperature) is converted into potential energy (chemical potential).

Extraction of electrons would then occur through a n-type membrane, and extraction of holes through a p-type membrane, the energy difference between extracted electrons and holes being the extracted energy E_{ext} mentionned in Ross and Nozik paper (see figure 2.4). In the limit of discrete energy levels and infinite carrier mobility in the membrane, this system enables optimal energy extraction with minimal heat losses. The output voltage V is then related to the quasi-Fermi level splitting in the absorber $\Delta\mu_H$ by [12]:

$$qV = \left(1 - \frac{T}{T_H}\right) E_{ext} + \Delta\mu_H \frac{T}{T_H} \tag{1.15}$$

where T is the lattice temperature and T_H is the carrier temperature.

1.4.2 Technological feasibility

The possibility to fabricate energy selective contacts have been adressed, either theoretically or experimentally. The contact selectivity is of course the key parameter that governs the design of selective contacts. As it was said above, the transmission range needs to be kept as small as possible for minimal interaction with the outside world. However, other concerns, and at first the ease of manufacture, can play a critical role.

Several different approaches were considered [17] and are described here:

- resonant tunneling through a quantum well energy level
- renonant tunneling through a quantum dot array
- renonant tunneling through defect states or impurities in a barrier oxide
- degenerate tunnel junctions

The three first solutions are very similar. It consists in a large band gap material layer insulating the hot distribution from the cold reservoir. Extraction of carriers is done by tunneling across the barrier. Carriers can tunnel either directly across the whole oxide thickness, or via a confined state in the middle of the oxide, created by a quantum well, quantum dots or defect states (see figure 1.3. Only carriers having the energy of the confined state can follow that pathway. The transmission probability decreases exponentially with the barrier thickness, which makes the resonant two steps process through the confined state much more probable, and energy selectivity is achieved.

In the case of a quantum well, the resonant level is only discrete in the direction perpendicular to the plane of the quantum well. In directions parallel to that plane, there is a continuum of available states. This means that a carrier with the right energy in the direction of quantization but with residual momentum in other directions may also tunnel across the double barrier, even though its total energy is outside the energy transmission range. Such structure is not a proper selective contact.

Total energy confinement with 3D quantization can be achieved with quantum dots embedded in a dielectric matrix. In that case, proper selectivity with very good selectivity can be obtained theoretically. However, in order to keep a small transmission range, all quantum dots must have a discrete level at the same energy. It means that the size distribution must be very uniform, which is difficult to fabricate practically.

A second solution to achieve 3D confinement is to have impurities in a large band gap material, that would form discrete levels in the barrier. Here the resonnance would be greatest for defects in the middle plan of the barrier. This solution makes the device easier to fabricate.

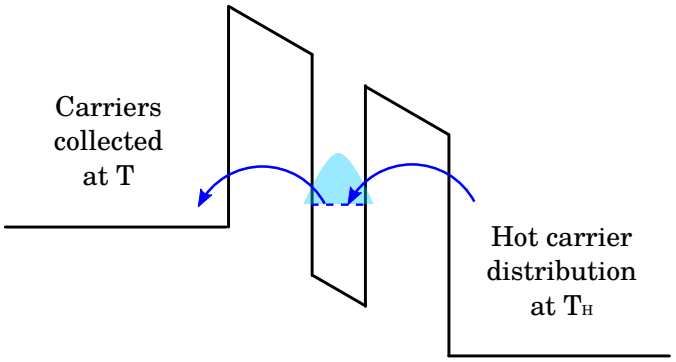

Figure 1.3: Schematic of double barrier structure for selective contacts. The hot electron population (on the right) at temperature T_H tunnel through the potential barrier, towards the cold population (on the left) at lattice temperature T. They can either cross directly the double barrier, or via the confined state in the quantum well. The probability of crossing the barrier is exponentially decreasing with increasing barrier thickness, enabling resonant transmission at the energy of the confined state.

This idea was theoretically investigated [18] (see chapter 2), with the conclusion that the barrier should be rather thick for good selectivity, and that impurities should lie in the middle of the insulator. Also, the systems providing the required selectivity were found to have rather low conductivity, which may be harmful in a hot carrier solar cell application where large current densities are expected.

The fourth solution that was proposed is the degenerate tunnel junction and is presented in figure 1.4. The excited carriers are withdrawn through a tunnel junction made of an abrupt type III degenerate pn-junction.

For such a device to work, some conditions need to be verified. The electrons must flow from the absorber towards the n contact. It means that the occupation factors, given by a Fermi-Dirac distribution in region i $f_i(E)$, must verify $f_A(E) < f_B(E) < f_C(E)$ (see figure 1.4) so diffusion can occur in the right direction. One can then write the condition:

$$\exp\left(\frac{E-E_{f_n}^A}{\mathrm{k}T_A}\right) \geq \exp\left(\frac{E-E_{f_n}^B}{\mathrm{k}T_B}\right) \geq \exp\left(\frac{E-E_{f_n}^C}{\mathrm{k}T_C}\right) \tag{1.16}$$

where $E_{f_n}^i$ is the quasi-Fermi level for electrons and T_i their temperature in material i, i=A,B or C, and E an energy in the δE interval. The same goes for holes with E_{f_p} replacing E_{f_n} as the hole quasi-Fermi level and $\leq$ instead of $\geq$.

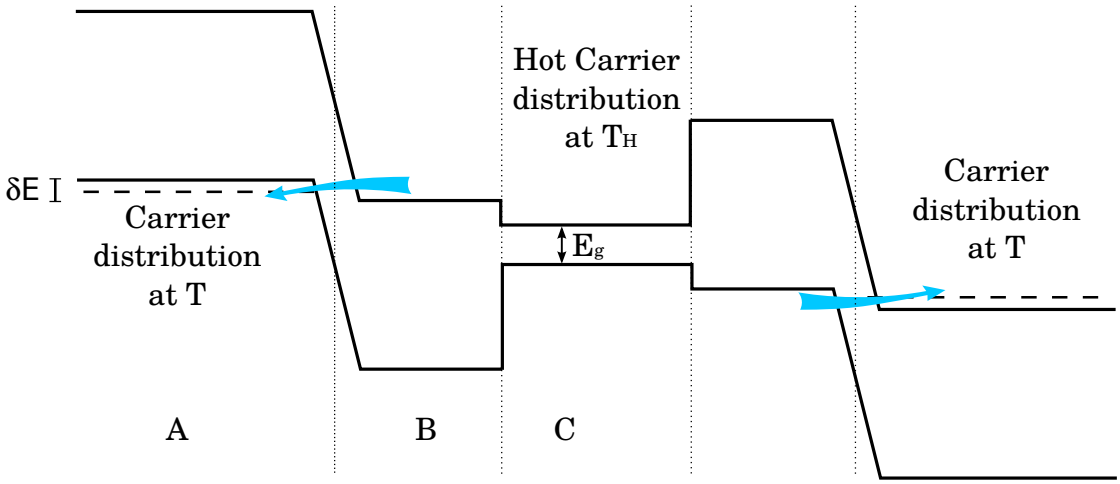

Figure 1.4: Schematic of tunnel junctions for selective contacts.

In material C (the absorber), the carrier temperature is the hot temperature T_H. If carriers in material B are thermally equilibrated with the hot distribution in C, then it implies that the quasi-Fermi level is higher in the absorber than in material B. Considering schematic 1.4, if material B is degenerated, it results in a quasi-Fermi level in the absorber that goes inside the conduction band. The same argument leads to the hole quasi Fermi-level inside the valence band. This is incompatible with light absorption (stimulated light emission would dominate over absorption). A lower carrier temperature is then necessary in material B in order to allow a quasi Fermi-level splitting in the absorber that is lower than the band gap, and to verify condition 1.16. Such temperature gradient would then be accompanied by an entropy flux that will degrade the cell conversion efficiency.

Also, from condition 1.16, one can deduce that:

$$\begin{aligned} \frac{E-\mu_e}{\mathrm{k}T_H} &\leq \frac{E-\mu_n}{\mathrm{k}T} \\ \frac{E-\mu_h}{\mathrm{k}T_H} &\geq \frac{E-\mu_p}{\mathrm{k}T} \end{aligned} \tag{1.17}$$

where μ_e and μ_h are the quasi-Fermi levels of electrons and holes in the absorber respectively, and μ_n and μ_p are the Fermi levels in the negative and positive electrodes respectively. Combining the above equations, one obtains:

$$\Delta\mu_H \geq qV\frac{T_H}{T} \tag{1.18}$$

where $\Delta\mu_H = \mu_e - \mu_h$ is the quasi-Fermi level splitting in the absorber, and $V = (\mu_n - \mu_p)/q$ is the external voltage.

The lattice temperature T being lower than the carrier temperature T_H, it follows directly that $\Delta\mu_H \geq qV$. The output voltage is therefore limited by the absorber band gap, similarly to a conventional solar cell. Those thermodynamical considerations indicate that the tunnel junction design does not provide a satisfactory solution for hot carrier solar cell selective contacts.

All solutions proposed so far for fabricating selective contacts revealed themselves unsatisfactory, and enable to solve the contradiction between high selectivity and large conductance. Results presented in chapter 2 may solve this issue by showing that selectivity may not be as critical as expected before.

Bibliography

[1] R.T. Ross and A.J. Nozik. Efficiency of hot-carrier solar energy converters. *Journ. Appl. Phys.*, 53:3813, 1982.

[2] A. Othonos. Probing ultrafast carrier and phonon dynamics in semiconductors. *Applied Physics Reviews*, 83:1789, 1998.

[3] M.A. Green. *Third generation photovoltaics - Advanced solar energy conversion.* Springer, 2003.

[4] P. Würfel. Solar energy conversion with hot electrons from impact ionization. *Solar Energy Materials and Solar Cells*, 46:43, 1997.

[5] D. Trivich and PA Flinn. Maximum efficiency of solar energy conversion by quantum process. *Solar Energy Research*, pages 143–147, 1955.

[6] W. Shockley and H.J. Queisser. Detailed balance limit of efficiency of *p-n* junction solar cells. *Journ. Appl. Phys.*, 32:510, 1961.

[7] P. Würfel. The chemical potential of radiation. *J. Phys. C: Solid State Phys.*, 15:3967–3985, 1982.

[8] M. Neges, K. Schwarzburg, and F. Willig. Monte carlo simulation of energy loss and collection of hot charge carriers, first step towards a more realistic hot-carrier solar energy converter. *Solar Energy Materials and Solar Cells*, 90(14):2107 – 2128, 2006.

[9] P.Y. Yu and M. Cardona. *Fundamentals of Semiconductors, Physics and Material Properties.* Springer-Verlag, 2001.

[10] B.K. Ridley. *Quantum processes in semiconductors.* Oxford University Press, 1999.

[11] J. Shah, P. Pinczuk, A.C. Gossard, and W. Wiegmann. Energy-loss rates for hot electron and holes in GaAs quantum wells. *Phys. Rev. Lett.*, 18:2045, 1985.

[12] P. Würfel, A.S. Brown, T.E. Humphrey, and M.A. Green. Particle conservation in the hot-carrier solar cell. *Prog. Photovolt: Res. Appl.*, 13:277, 2005.

[13] M. Pugnet, J. Collet, and A. Cornet. Cooling of hot electron-hole plasmas in the presence of screened electron-phonon interactions. *Solid State Comm.*, 38:531–536, 1981.

[14] W. Pötz and P. Kocevar. Electronic power transfer in pulsed laser excitation of polar semiconductors. *Phys. Rev. B*, 28:7040, 1983.

[15] R. Ulbrich. Energy relaxation of photoexcited hot electrons in GaAs. *Phys. Rev. B*, 8:5719, 1973.

[16] A. Luque and A. Martí. Electron-phonon energy transfer in hot-carrier solar cells. *Solar Energy Materials & Solar Cells*, 94:287–296, 2010.

[17] G. Conibeer, C.W. Jiang, M. Green, N. Harder, and A. Straub. Selective energy contacts for potential application to hot carrier PV cells. In *Photovoltaic Energy Conversion, 2003. Proceedings of 3rd World Conference on*, volume 3, page 2730. IEEE, 2004.

[18] C.W. Jiang, M.A. Green, E.C Cho, and G. Conibeer. Resonant tunneling through defects in an insulator: modeling and solar cells applications. *Journ. Appl. Phys.*, 96:5006, 2004.

Chapter 2

Heat losses in the selective contacts

2.1 Models of non-ideal contacts

The selectivity of the contact is expected to be a key parameter in the cell efficiency. However, no quantitative analysis of losses in non-ideal contacts has been done so far. In this section, a model of carrier transport through a one dimensional channel is proposed and included in the particle conservation hot carrier solar cell model. A new system of equations is obtained and solved. The influence of the contact transmission range, conductance and extraction energy on carrier temperature, heat loss, and efficiency is studied.

2.1.1 Landauer formalism

When non ideal contacts are considered, the method described in [1] for determining the charge and energy balance can not be applied anymore. The carriers are not extracted at a discrete, single energy E_{ext}, so the power extracted from the system can not be simply determined as the product of the current extracted times the extraction energy. It will be an integration of the extracted current mutliplied by the energy of the extracted carriers over the extraction energy range. Additional equations are necessary to describe the charge and energy flow through the selective contacts.

The Landauer formalism can be applied to describe the particle flux through a conductor between two particles reservoirs (see figure 2.1). It was developped in [2, 3, 4, 5] and reviewed in [6]. It relates the current between two leads connected by a ballistic conductor to the voltage across the system, considering the probability that a particle entering the conductor is transmitted through it. In this formalism,

I is the result of a balance between currents flowing in each direction, between left going I_R and right going I_L electrons.

Let us consider a ballistic conductor (see figure 2.1), whose transverse dimension is small compared to the carrier free path, so carriers are not scattered, and conductivity inside the conductor is infinity (resistance is zero). The resistance of the system comes only from the interfaces between the conductor and the reservoirs. Such interface resistance comes from the rearrangement of a large density of transverse modes in the leads into a few transverse modes in the conductor (see for instance [7] for details).

Consider a single transverse mode in the right direction whose k states are occupied according to a distribution function $f(E)$. A uniform electron gas density n with velocity v carries a current qnv. The electron density associated with a single k-state in a conductor of length L is $1/L$, and the current from the left to the right is:

$$I_L = \frac{q}{L}\sum_k f_L(E)v(k) = \frac{q}{L}\sum_k \frac{1}{\hbar}\frac{dE}{dk}f_L(E) \tag{2.1}$$

Assuming periodic boundaries and converting the sum over k into an integral according to the usual prescription:

$$\sum_k \rightarrow 2 \times \frac{L}{2\pi}\int dk \tag{2.2}$$

where the factor 2 accounts for the spin degeneracy, one obtain:

$$I_L = \frac{2q}{h}\int_\varepsilon^\infty f_L(E)dE \tag{2.3}$$

where ε is the cutoff energy of the waveguide mode. This expression can be extended to a multimode waveguide:

$$I_L = \frac{2q}{h}\int_{-\infty}^\infty M(E)f_L(E)dE \tag{2.4}$$

where $M(E)$ is the number of modes above the cutoff at energy E. A similar expression is obtained for the current from the right reservoir.

If now one considers a transmission probability τ that an electron entering the conductor from the left lead is transmitted to the right lead (one assumes here that this probability is the same for left going and right going electrons), the expression above becomes:

$$I_L = \frac{2q}{h}\int_{-\infty}^\infty \tau(E)M(E)f_L(E)dE \tag{2.5}$$

It will be considered now that the conductor can be described by an areal density N of identical and independent monomode contacts with tranmissivity $\tau(E)$. The current is then given by equation 2.5 with $M(E) = 1$ and multiplied by N. Finally, if the carrier distributions on both sides of the conductor are Fermi distributions with respective Fermi energy ε_L and ε_R, and respective temperatures T_L and T_R, the net current is:

$$I = \frac{2qN}{h} \int_{-\infty}^{\infty} \tau(E) \left[f\left(E, \varepsilon_L, T_L\right) - f\left(E, \varepsilon_R, T_R\right) \right] dE \tag{2.6}$$

The energy current is obtained similarly, by multiplying the integrand by the energy E of the transmitted electrons.

In these expressions of particle and energy flux, the transmissivity $\tau(E)$ is not specified and can take any form. In particular, it can be the transmissivity of selective contact with non zero values only in a small energy range. In section 2.2.2, a constant transmission probability equal to one in a narrow energy range $[E_{ext}/2, E_{ext}/2 + \delta E]$, and equal to zero outside, will be considered. Such transmission profile allows to study the impact of the energy width of the selective contacts on the cell efficiency, even if it is not realistic in practice. More realistic transmissivity functions are described below.

2.1.2 Transport in low dimensional structures

Double barrier tunneling

The case of resonant tunneling in a double barrier semiconductor is a textbook problem that is theoretically treated for instance in [7]. It was first observed experimentally by Chang et al [8]. It consists in a tunneling through two successive barriers where the distance between the two barriers is small compared to the electron De Broglie wavelength (that is to say a few nanometers). In that case, the region between the barrier is a quantum well with confined states, and a peculiar behaviour is observed.

Let consider a case where a small band gap material A is sandwiched between two large band gap barriers in material B, the left and right reservoirs being material A (for instance, GaAs/AlGaAs/GaAs/AlGaAs/GaAs) which is respresented in figure 2.2.

The current is calculated using the Laudauer formalism described above. Equation 2.6 applies to determine the $I-V$ characteristic of the system. Carrier distributions on both sides of the system are Fermi-Dirac distributions at temperature

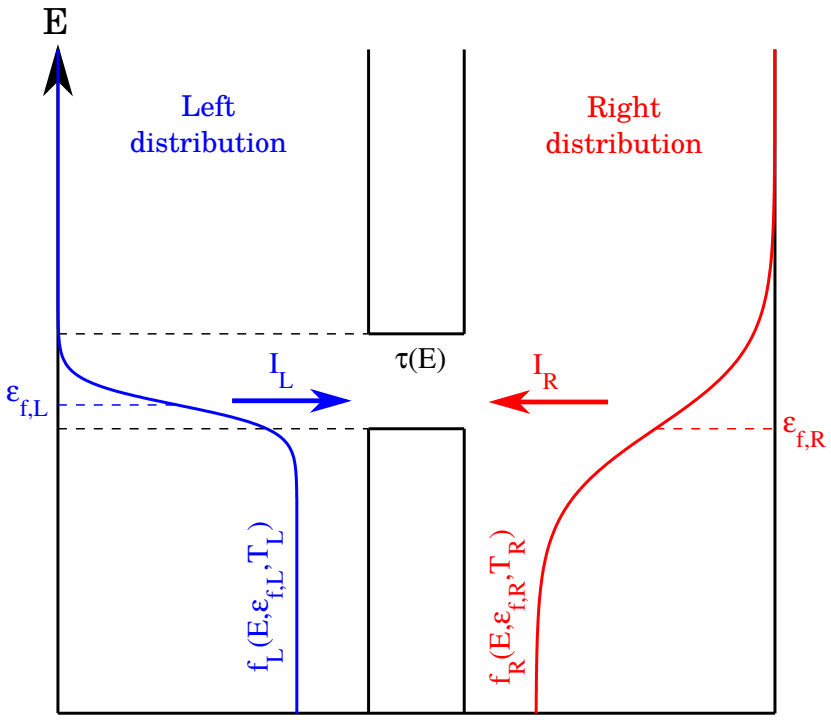

Figure 2.1: Schematic of a conductor between two carrier reservoirs, on the left at temperature T_L and Fermi energy $\varepsilon_{f,L}$, and on the right at temperature T_R and with Fermi enregy $\varepsilon_{f,R}$. Here, $T_L < T_R$ and $\epsilon_{f,L} > \varepsilon_{f,R}$. The carrier distributions are Fermi-dirac distributions. The net current is the difference between left going current I_R and right going current I_L. $\tau(E)$ is the probability that an electron having energy E is transmitted through the contact. The conductor represented here is a band-pass filter.

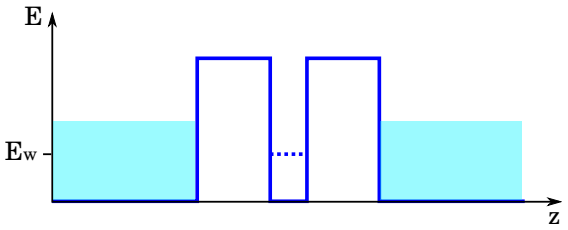

(a) $V = 0$

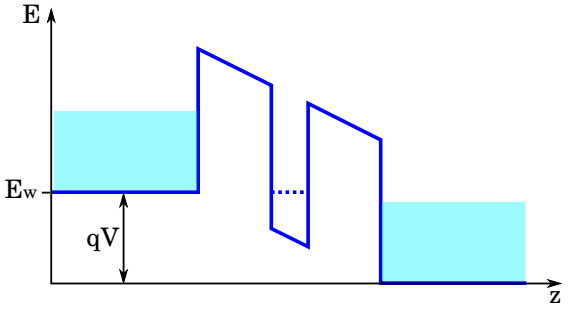

(b) $V = V_r$

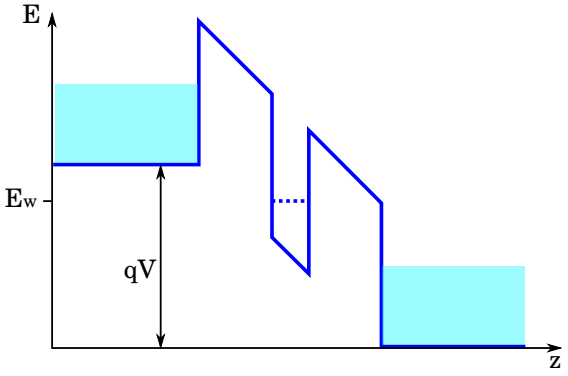

(c) $V > V_r$

Figure 2.2: Schematic of a double barrier structure. A discrete energy level at E_w allows carrier transmission. With no voltage applied to the structure (a), no current flows. When voltage is increased (b), the current increases exponentially until the energy of the confined state becomes lower than the conduction band minimum (c). In that case, there is no available state in the quantum well for carriers in the left distribution to tunnel. Maximum current is obtained at a resonance voltage V_r for which the quantum well confined state is aligned with the bottom of the conduction band on the left.

T and Fermi energies μ_1 and μ_2 and the voltage across the double barrier is defined as $V = (\mu_1 - \mu_2)/q$. The function $\tau(E)$ is simply determined by solving the Schrödinger equation in such geometry, so the current can be calculated.

At low voltage, the current increases exponentially with applied voltage. However, the position of the confined state is shifted (see figure 2.2). When this confined state is lower than the bottom of the conduction band in the left lead, resonant tunneling becomes impossible, and the current drops sharply. At higher voltage, the carriers can be transmitted by jumping above the barrier. A resonant behaviour is observed with a local maximum of current at a voltage V_r that correspond to a minimum of resistance. Immediately after the peak, the current decreases which can be seen as a negative differential resistance effect.

Such architecture could be used as a possible selective contact. However, the transmission range is rather large (a few hundreds of meV, large compared to kT), and carriers outside of the transmission range are not blocked efficiently. Another approch may provide better selectivity.

A first experimental demonstration of the resonant tunneling effect was proposed in [8]. A negative differential resistance was observed with a GaAs layer embedded between two $Al_{0.7}Ga_{0.3}As$ layers at 77 K. A more recent demonstration is proposed in [9] on a comparable structure at 77 K. It showed that the energy position of the resonance is shifted with an increase of the excitation energy, indicating a heating of carriers. This demonstrates the extraction of high energy carriers through a double barrier system.

Transport through a quantum dot or defect array

The second solution to fabricate selective contacts is resonant tunneling through discrete states in an insulator matrix (see section 1.4). It can be achieved either with quantum dots [10, 11] or defects [12] in an insulator matrix.

Let consider the case of defect states in an insulator, which has been theoretically studied [12]. In such architecture, two transmission modes are possible: (i) a direct tunnel transmission through the whole insulator thickness, (ii) or a resonant double barrier transmission using a discrete state in the matrix. In the first process, transmission probability is found simply by solving Shrödinger equation with a finite potential barrier.

In the second process, the insulator potential is modified by the presence of a defect, which can be represented by a potential well embedded in the barrier. The width of that well represents the physical range of the defect, and the position of the confined state in the well can be tuned by adjusting the well depth to match the position of the defect state. This situation can then be treated as a

double barrier problem. The transmission probability is determined as a function of carrier energy and results are given in figure 2.3.

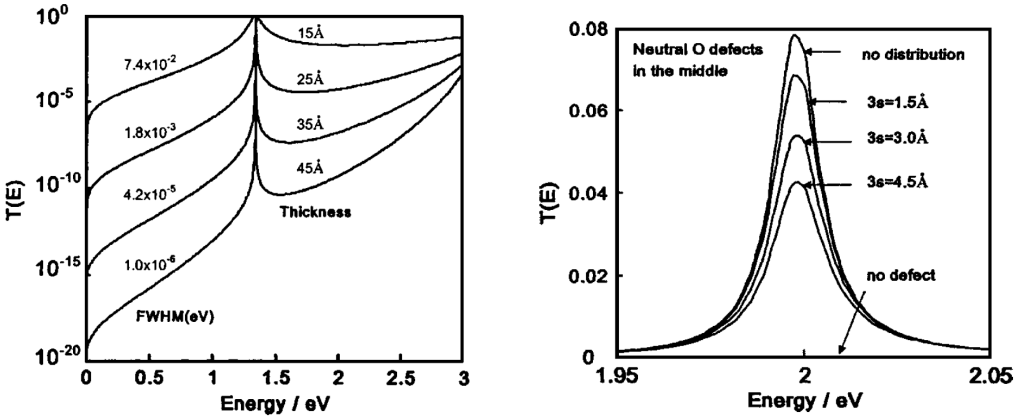

(a) (b)

Figure 2.3: Transmission coefficient of an insulator with defects embedded for resonant tunnel transmission vs carrier energy. Zero energy is the conduction-band minimum of the contact material to the insulator. (a): defects at the middle of the insulator, for different barrier thicknesses. (b): neutral oxygen vacancy defects distributed with a normal distribution centered at the middle of a 16 Å thick SiO_2 insulator with standard deviation s.

Transmissivity can be calculated for different material effective masses, barrier thickness, and defect distribution in the barrier. Calculations show that very good selectivity can be achieved theoretically, in the case of defects at the middle of the insulator matrix. Higher conductivity is obtained with thin barriers, but with lower selectivity 2.3(a). However, the peak transmissivity is lowered when the defects position deviates from the middle of the insulator, or when the defects are spatially distributed in the insulator thickness 2.3(b). A few Ångström displacement or standard deviation in the defect position can annihilate the resonance.

Selective contacts can theoretically be fabricated with the required selectivity with defect states in an insulator matrix. Nevertheless, it may turn out to be very difficult to meet the requirements concerning the control of the defects position and distribution, and the technological demonstration of selective contacts is not obvious so far.

The case of resonant tunneling through a quantum dot array can be treated similarly. It was theoretically investigated in [10]. Experimental demonstration of

the effect is proposed in [11] with silicon nanodots embedded in a SiO_2 matrix, showing negative differential resistance at ambient temperature. The resonance is however not very strong, with only a 20% reduction of the current density between the peak and the valley. The peak is broadened by the size distribution of the dots and by phonon-assisted tunneling at ambient temperature. The current density may also be too small for a hot carrier solar cell application. Another experimental result is proposed in [9] using InAs quantum dots in an AlGaAs barrier, showing that the energy position of the resonance in this structure could make it suitable for hot carrier solar cell application.

2.2 Analytical model

2.2.1 State of the art of hot carrier solar cell models

Previous models of hot carrier solar cells were reminded in chapter 1. They are based on a detailed balance model introduced by Shockley and Queisser [13], where the current is defined as the difference between the photogenerated carrier flux and the radiatively recombined carrier flux. Hot carrier solar cells though differ from this picture because the carrier temperature in the absorber T_H is unknown and the quasi Fermi level splitting $\Delta\mu_H$ is not the output voltage qV. Three variables are involved (T_H, $\Delta\mu_H$ and V), so additional equations are necessary.

An energy balance equation is considered, where the power delivered is the difference between the absorbed power and the power lost by radiative recombinations [14, 1]. It was generally assumed that no other losses occur. In particular, thermalization losses due to the carrier cooling were neglected.

Finally, ideal selective contacts were considered, which enables to express the output voltage V as a simple function of the other variables of the system.

$$qV = (1 - \frac{T_C}{T_H})E_{ext} + \Delta\mu_H \frac{T_C}{T_H} \tag{2.7}$$

where q is the charge of the electron and E_{ext} is the extraction energy as defined in figure 2.4 (see this figure also for the definition of V and $\Delta\mu_H$). In this model, since electron-hole pairs are extracted at the energy discrete E_{ext}, the power extracted is then related to the current extracted through:

$$P = E_{ext}J \tag{2.8}$$

so finally, the system can be written:

$$\begin{cases} J = J_{abs} - J_{em}(\Delta\mu_H, T_H) \\ E_{ext}J = P_{abs} - P_{em}(\Delta\mu_H, T_H) \end{cases} \tag{2.9}$$

where the absorbed and emitted energy and particle fluxes are given by a generalized Planck formula [15].

$$J_{abs/em} = \underbrace{\frac{\Omega_{abs/em}}{4\pi^3\hbar^3c^2}}_{C} \int_{E_G}^{\infty} \frac{A(E)E^2}{\exp\left(\frac{E-\mu}{\mathrm{k_B}T}\right)-1} dE \tag{2.10}$$

$$P_{abs/em} = \frac{\Omega_{abs/em}}{4\pi^3\hbar^3c^2} \int_{E_G}^{\infty} \frac{A(E)E^3}{\exp\left(\frac{E-\mu}{\mathrm{k_B}T}\right)-1} dE \tag{2.11}$$

where $\Omega_{abs/em}$ is the solid angle of incident or emitted photon respectively, E_G is the absorbing material band gap, $A(E)$ is the material absorptivity (the probability for a photon incident on the surface to be absorbed), μ is zero for absorption and $\Delta\mu_H$ for emission, T is the temperature of the incident photon for absorption and T_H for emission.

For a given voltage V, the chemical potential can be expressed as a function of the carrier temperature from equation 2.7, and the current J can be determined. $I-V$ curves are calculated this way.

Heat losses can be added in the energy balance equation by introducing the power lost by thermalization P_{th} as a function of the carrier temperature and chemical potential. The resolution method is unchanged. This will be discussed in chapter 4.

The assumption of perfect energy selectivity is obviously not realistic. The purpose of this work is to extend such model to a case of non ideal contacts, allowing carrier transmission in a narrow energy width. One can see in figure 2.4 that electrons and holes are withdrawn from the absorber towards the contacts through a membrane with a transmission energy range δE. Electrons are extracted between energies E^e_{ext} and $E^e_{ext}+\delta E$, and holes between energies E^h_{ext} and $E^h_{ext}-\delta E$. The extraction energy is defined as the minimum of the extracted electron-hole pair energy $E_{ext} = E^e_{ext} - E^h_{ext}$.

In these conditions, the relation between the voltage and the quasi Fermi level splitting in equation 2.7 does not apply. Also, the power extracted is not simply the particle flux multiplied by the extraction energy. Instead, a relation will be established between the charge or energy flux crossing a contact and the carrier chemical potential and temperature on each side of the contact using the Landauer formalism. For electron contact for instance, the current can be expressed as a function of the electron chemical potential in the absorber (μ^e) and in the electrode (μ^n) (see figure 2.4), and of the electron temperature T_H. A similar relation is obtained for holes involving μ^h and μ^p. Finally, the particle current J on the one side, the power extracted P on the other side, are expressed as functions of the

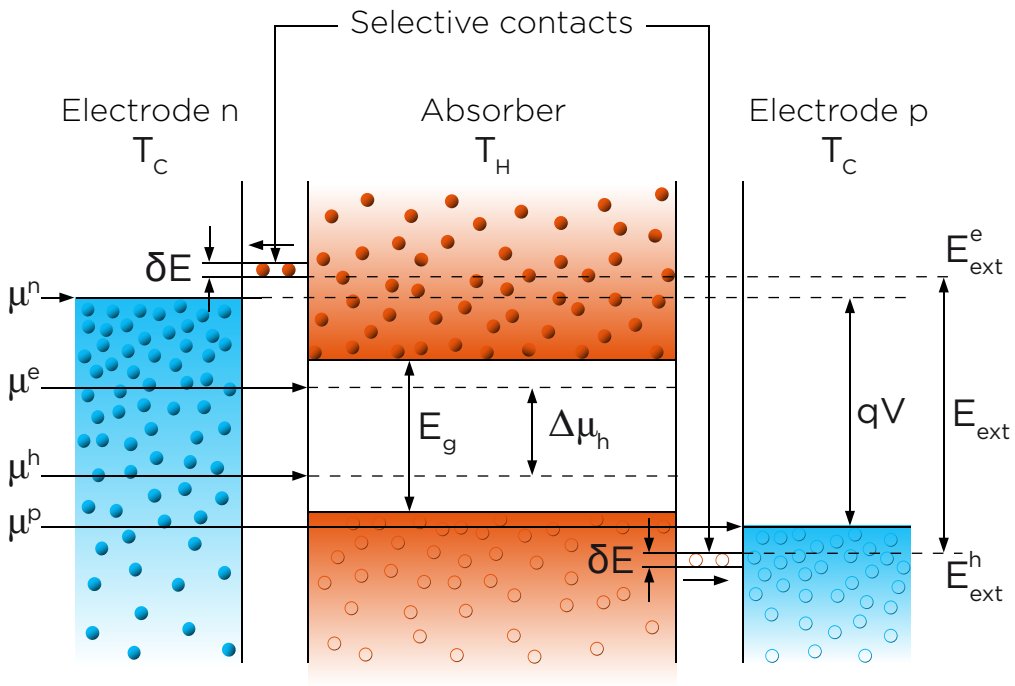

Figure 2.4: Schematic of a hot carrier solar cell. Photons are absorbed in the absorber having a band gap E_g, where carriers are in thermal and chemical disequilibrium with the lattice at temperature T_C, characterized by a temperature $T_H > T_C$ and a quasi Fermi level splitting $\Delta\mu_H = \mu^e - \mu^h \neq 0$. Carriers are extracted through selective contacts with a transmission energy range δE, electrons at energy E^e_{ext}, and holes at energy E^h_{ext}, towards electrode with an applied voltage $V = (\mu^n - \mu^p)/q$. The extraction energy E_{ext} is defined as the difference $E^e_{ext} - E^h_{ext}$. E_{ext} can be higher than the band gap.

voltage $V = (\mu^n - \mu^p)/q$, the quasi Fermi level splitting $\Delta\mu_H = \mu^e - \mu^h$, and the carrier temperature.

2.2.2 Formulation of the problem

In the general case, the following system of equations applies to describe the charge and energy conservation:

$$\begin{cases} J = J_{abs} - J_{em} - J_{nonrad} \\ P = P_{abs} - P_{em} - P_{th} \end{cases} \tag{2.12}$$

where J_{abs} is the absorbed photon current, J_{em} is the emitted photon current (from radiative recombination), P_{abs} is the solar power absorbed by carriers, P_{em} is the power lost by radiative recombination, J_{nonrad} is the particle flux that is lost due to non radiative recombinations, and P_{th} is the power lost by thermalization (including non radiative recombinations). J and P are the particle and energy current densities extracted from the cell.

The absorbed power is either re-emitted by radiative recombination (P_{em}), lost by thermalization (P_{th}) or extracted through the contacts (P). A fraction of the extracted power is then available as free energy in the form of electric power $P_{el} = I \times V = qJ \times V$, or lost upon carrier extraction because of entropy generation. This fraction of the transmitted power that is lost will be called $P_{contact}$ and is defined by: $P_{contact} = P - P_{el}$, so one can write:

$$P_{abs} = P_{em} + P_{th} + P_{contact} + P_{el} \tag{2.13}$$

Absorption and emission processes are described, assuming the solar spectrum is a black body spectrum, by a generalized Planck law, and the absorbed and emitted particle and energy fluxes are given by equations 2.10 and 2.11.

In the case of absorption, the chemical potential of the photon population is zero, and the temperature is the temperature of the sun, approximatively 6000K. In the case of emission, the chemical potential and temperature of the emitted photons are those of the electron-hole population, that is to say the quasi-Fermi level splitting and the carrier temperature [15].

In this section, the power lost by thermalization is neglected. We will see how it can be treated in chapter 4. Recombinations will be considered radiatively dominated in all simulations, so the non radiative term J_{nonrad} is always zero.

The current J and the power P that flow through the selective contacts for electrons can be expressed, after the one-dimensional Landauer equation (see sec-

tion 2.1.1, equation 2.6):

$$\begin{aligned} J_e &= \underbrace{\frac{2N}{h}}_{G/q^2} \int_{E_{min}}^{E_{max}} \tau(E) \left(f_H(E) - f_C(E)\right) dE \\ &= J_e^+ - J_e^- \end{aligned} \tag{2.14}$$

$$\begin{aligned} P_e &= \frac{2N}{h} \int_{E_{min}}^{E_{max}} E\tau(E) \left(f_H(E) - f_C(E)\right) dE \\ &= P_e^+ - P_e^- \end{aligned} \tag{2.15}$$

where

$$J_e^+ = \frac{G}{q^2} \int_{E_{min}}^{E_{max}} \frac{\tau(E)}{\exp\left(\frac{E-\mu_e}{\mathrm{k_B}T_e}\right) + 1} dE \tag{2.16}$$

$$J_e^- = \frac{G}{q^2} \int_{E_{min}}^{E_{max}} \frac{\tau(E)}{\exp\left(\frac{E-\mu_n}{\mathrm{k_B}T}\right) + 1} dE \tag{2.17}$$

$$P_e^+ = \frac{G}{q^2} \int_{E_{min}}^{E_{max}} \frac{E\tau(E)}{\exp\left(\frac{E-\mu_e}{\mathrm{k_B}T_e}\right) + 1} dE \tag{2.18}$$

$$P_e^- = \frac{G}{q^2} \int_{E_{min}}^{E_{max}} \frac{E\tau(E)}{\exp\left(\frac{E-\mu_n}{\mathrm{k_B}T}\right) + 1} dE \tag{2.19}$$

$f_C(E)$ and $f_H(E)$ are the electronic distribution functions in the cold electrode and in the hot absorber respectively. $\tau(E)$ is the contact transmissivity as defined in section 2.1.1. μ_n and μ_e are the electronic chemical potential in the n electrode and in the absorber respectively, and T_e is the electron temperature. E_{min} and E_{max} are the lower and upper bounds for integration. They depend on the transmissivity τ and will be discussed later. The prefactor in expressions 2.14 and 2.15 $\frac{2N}{h}$ comes from the Landauer formalism, with N being the areal density of transverse modes in the selective contact. It is related to the conductance G of the contact (see section 2.3.4) by:

$$G = \frac{2Nq^2}{h} = NG_0 \tag{2.20}$$

where G_0 is the quantum of conductance.

Similar expressions are obtained for holes, with μ_h and T_h as the hole chemical potential and temperature in the absorber, and μ_p as the electron chemical potential in the p electrode. In steady state conditions, $J = J_e = J_h$ and $P = P_e + P_h$. The electron and hole chemical potentials are related as follows:

$$\begin{aligned} \Delta\mu_H &= \mu_e - \mu_h \\ qV &= \mu_n - \mu_p \end{aligned} \tag{2.21}$$

Finally, the system 2.12 can be written:

$$\begin{cases} J_e^+(\mu_e, T_e) - J_e^-(\mu_n, T) = J_h^+(\mu_h, T_h) - J_h^-(\mu_p, T) \\ \qquad\qquad\qquad\qquad = J_{abs} - J_{em}(\Delta\mu_H, T_H) \\ P_e^+(\mu_e, T_e) - P_e^-(\mu_n, T) + P_h^+(\mu_h, T_h) - P_h^-(\mu_p, T) \\ \qquad\qquad\qquad\qquad = P_{abs} - P_{em}(\Delta\mu_H, T_H) \end{cases} \tag{2.22}$$

The method to determine the current as a function of the voltage consists in finding, for a given voltage, the values of $\Delta\mu_H$ and T_H to equilibrate both equations of system 2.22 (other unknowns such as μ_e and T_e can be related to those variables, as shown in 2.2.4), and then to compute J. This problem has no analytical solution in general. It can be solved using numerical methods, but some approximations can be made that allow an analytical solution to be found.

2.2.3 The Boltzman distribution approximation

In the generalized Planck law of radiation, the photon distribution function is a Bose-Einstein distribution:

$$f_{abs/em}(E) = \frac{1}{\exp\left(\frac{E-\mu}{\mathrm{k_B}T}\right) - 1} \tag{2.23}$$

where μ is the photon chemical potential and T is the photon or carrier temperature for absorption or emission respectively. If μ is small enough for the condition

$$\frac{E-\mu}{\mathrm{k}_B T} > 2 \tag{2.24}$$

to be verified over all the integration range, it is possible to consider that

$$\exp\left(\frac{E-\mu}{\mathrm{k}_B T}\right) \gg 1 \tag{2.25}$$

As the integration range is from the band gap energy to infinity, the condition 2.24 is verified if

$$\frac{E_G - \mu}{\mathrm{k}_B T} > 2. \tag{2.26}$$

In this case, the photon distribution is described by a Boltzmann distribution:

$$f_{abs/em}(E) = \exp\left(-\frac{E-\mu}{\mathrm{k_B}T}\right) \tag{2.27}$$

In the case of absorption, the photon chemical potential is zero, and the photon temperature is approximately 6000 K, so the condition is verified for band gap larger than 1 eV ($\mathrm{k_B}T \approx 0.5$ eV). For smaller band gap, it is not possible to make the Boltzmann approximation, and a numerical resolution is necessary. However, one can assume that absorption is independent of the carrier temperature and chemical potential and it can be treated as a constant in the problem, so a numerical computation is not a major issue.

In the case of emission, the photon potential is the quasi-Fermi level splitting, which is always smaller than the bandgap in solar cell operating conditions. It has been demonstrated for ideal hot carrier solar cell [1] that the best efficiency was obtained with the smallest (and even negative) chemical potential. This means that the condition is very likely to be verified in the system that is considered here. It will be verified *a posteriori* after the carrier temperature and chemical temperature have been determined.

The same analysis applies for the equations describing the transmission at the contacts, with a Fermi-Dirac distribution instead of the Bose-Einstein law, and the extraction energy E_{ext} replacing E_G as lower bound for integration. For the current flowing from the absorber to the electrodes, the condition 2.24 is automatically verified if the condition for photoemission is satisfied, since $E_{ext} \geq E_G$.

For the current flowing from the electrodes to the absorber, the chemical potential is related to the voltage ($\mu = qV$), and the condition 2.24 is verified for chemical potential smaller than the extraction energy E_{ext} by more than 0.05 eV, which is the case in the diode generator regime.

2.2.4 Other approximations

In equations 2.10 and 2.11, the material aborptivity is in general unknown, especially if the cell is not made of a single thick bulk layer. However, this absorptivity has to be close to one for a solar cell to be efficient. Here, one makes the assumption of a constant absorptivity over all the spectrum above the band gap. It will be taken in general equal to one which gives the upper limit of efficiency.

An exact knowledge of the absorption coefficient is not necessary to have a qualitative description of the behaviour of a hot carrier solar cell. Assuming a constant absorptivity allows a much simpler formulation with the absorptivity out of the integral, and an analytical expression of photoabsorption and photoemission. The influence of thermalization properties and contacts on the cell performance can be more easily investigated.

The transmissivity function $\tau(E)$ is also unknown. Solutions have been proposed to synthesize energy selective contacts for which this transmissivity has been determined, theoretically and experimentally. Here, in order to remain as general as possible and to maximize the efficiency, the transmissivity is taken constant and equal to one in the transmission range of the selective contacts, and equal to zero outside.

Finally, the problem is considered symmetrical for electrons and holes. The carrier temperature is the same for electrons and holes and the chemical potential is assumed to be symmetrically distributed between both populations. For simpler expression, the origin of energy will be taken at the middle of the band gap. The conduction band energy is then $E_G/2$, the valence band energy $-E_G/2$, and the selective contacts are also symmetrical, with a transmission range $[E_{ext}/2, E_{ext}/2 + \delta E]$ for the electron contact, and $[-E_{ext}/2, -E_{ext}/2 - \delta E]$ for the hole contact. If the quasi-Fermi level splitting is $\Delta\mu_H$, the electron and hole chemical potentials are then $\mu_e = -\mu_h = \Delta\mu_H/2$.

Such an assumption is valid if electrons and holes have the same effective mass. It is not the general case, but it allows to capture the physics of the problem. In practice, holes are likely to be quickly thermalized because of their large effective masses while electrons can remain hot. A case where holes would be considered in equilibrium with the lattice and only electrons are not thermalized appears to be a good approximation but is not treated here.

It can be noted that such a situation is not incompatible with high efficiency as the majority of the photon energy is transferred to electrons rather than holes. When absorbing a photon with energy $h\nu$, conservation of energy and momentum implies that $E_e - E_h = h\nu$ and $k_e - k_h \approx 0$ (see figure 2.5). The assumption of parabolic bands ($E_e = E_G/2 + \frac{\hbar^2 k^2}{2m_e^*}$ in the conduction band, $E_h = -E_G/2 - \frac{\hbar^2 k^2}{2m_h^*}$ in the valence band) leads to the following equation on k :

$$k^2 = (h\nu - E_G) \times \frac{2}{\hbar} \frac{m_e^* m_h^*}{m_e^* + m_h^*} \tag{2.28}$$

And the values of E_e and E_h are obtained:

$$E_e = \frac{E_G}{2} + (h\nu - E_G)\frac{m_h^*}{m_e^* + m_h^*} \tag{2.29}$$

$$E_h = -\frac{E_G}{2} - (h\nu - E_G)\frac{m_e^*}{m_e^* + m_h^*} \tag{2.30}$$

This means that a fraction $m_h^*/(m_e^* + m_h^*)$ of the excess energy $(h\nu - E_G)$ is given to the electrons, and $m_e^*/(m_e^* + m_h^*)$ is given to the holes. If the effective mass of holes is large compared to the electron effective mass, which is the case in most semiconductors, the kinetic energy of the electron-hole gas will be stored mainly among electrons. In these conditions, thermalization of holes would not cause major losses as long as electrons can be kept hot.

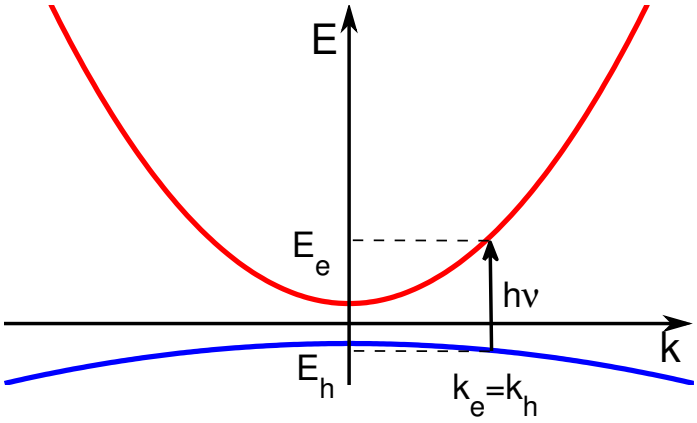

Figure 2.5: Electronic dispersion relation in a semiconducteur with parabolic bands ($E = \frac{\hbar^2 k^2}{2m^*}$, m^* being the effective mass of electrons or holes). An incident photon with energy $h\nu > E_G$ is absorbed and an electron-hole pair is generated with conservation of energy $E_e - E_h = h\nu$ and momentum $k_e - k_h \approx 0$.

A model where electrons and holes are treated separately, with different temperatures, is proposed in [16]. It shows that the full thermalization of holes has little influence on the cell efficiency.

As a consequence of the approximation of symmetrical bands, the expression of charge and power currents at the electron contact and hole contact are the same in that case and only the electronic equation is considered ($P_e = P_h = P/2$, $J_e = J_h = J$).

2.2.5 Analytical formulation

These approximations lead to the following expressions:

$$\begin{aligned} J_{em}\left(\Delta\mu_H, T_H\right) &= C\int_{E_G}^{\infty} E^2 \exp\left(-\frac{E-\Delta\mu_H}{\mathrm{k_B}T_H}\right) dE \\ &= f_1(T_H)\exp\left(\frac{\Delta\mu_H}{\mathrm{k_B}T_H}\right) \end{aligned} \tag{2.31}$$

$$\begin{aligned} P_{em}\left(\Delta\mu_H, T_H\right) &= C\int_{E_G}^{\infty} E^3 \exp\left(-\frac{E-\Delta\mu_H}{\mathrm{k_B}T_H}\right) dE \\ &= f_2(T_H)\exp\left(\frac{\Delta\mu_H}{\mathrm{k_B}T_H}\right) \end{aligned} \tag{2.32}$$

$$\begin{aligned} J^{+}\left(\Delta\mu_H, T_H\right) &= \frac{G}{q^2}\int_{E_{min}}^{E_{max}} \exp\left(-\frac{E-\Delta\mu_H}{2\mathrm{k_B}T_H}\right) dE \\ &= f_3(T_H)\exp\left(\frac{\Delta\mu_H}{2\mathrm{k_B}T_H}\right) \end{aligned} \tag{2.33}$$

$$\begin{aligned} J^{-}\left(qV, T\right) &= \frac{G}{q^2}\int_{E_{min}}^{E_{max}} \exp\left(-\frac{E-qV}{2\mathrm{k_B}T}\right) dE \\ &= f_3(T)\exp\left(\frac{qV}{2\mathrm{k_B}T}\right) \end{aligned} \tag{2.34}$$

$$\begin{aligned} P^{+}\left(\Delta\mu_H, T_H\right) &= \frac{G}{q^2}\int_{E_{min}}^{E_{max}} E\ \exp\left(-\frac{E-\Delta\mu_H}{2\mathrm{k_B}T_H}\right) dE \\ &= f_4(T_H)\exp\left(\frac{\Delta\mu_H}{2\mathrm{k_B}T_H}\right) \end{aligned} \tag{2.35}$$

$$\begin{aligned} P^{-}\left(qV, T\right) &= \frac{G}{q^2}\int_{E_{min}}^{E_{max}} E\ \exp\left(-\frac{E-qV}{2\mathrm{k_B}T}\right) dE \\ &= f_4(T)\exp\left(\frac{qV}{2\mathrm{k_B}T}\right) \end{aligned} \tag{2.36}$$

with

$$f_1(T) = C\left(2(\mathrm{k_B}T)^3 + 2E_G(\mathrm{k_B}T)^2 + E_G^2\mathrm{k_B}T\right)\exp\left(-\frac{E_G}{\mathrm{k_B}T}\right) \tag{2.37}$$

$$f_2(T) = C\left(6(\mathrm{k_B}T)^4 + 6E_G(\mathrm{k_B}T)^3 + 3E_G^2(\mathrm{k_B}T)^2 + E_G^3\mathrm{k_B}T\right)\times \exp\left(-\frac{E_G}{\mathrm{k_B}T}\right) \tag{2.38}$$

$$f_3(T) = \frac{G}{q^2}\mathrm{k_B}T\ \exp\left(-\frac{E_{ext}+\delta E}{2\mathrm{k_B}T}\right)\sinh\left(\frac{\delta E}{2\mathrm{k_B}T}\right) \tag{2.39}$$

$$f_4(T) = \frac{G}{q^2}\mathrm{k_B}T\ \exp\left(-\frac{E_{ext}+\delta E}{2\mathrm{k_B}T}\right)\times \left[\left(\frac{E_{ext}+\delta E}{2}+\mathrm{k_B}T\right)\sinh\left(\frac{\delta E}{2\mathrm{k_B}T}\right) - \frac{\delta E}{2}\cosh\left(\frac{\delta E}{2\mathrm{k_B}T}\right)\right] \tag{2.40}$$

and where $[E_{min}, E_{max}]$ is the transmission range of the selective contacts, $E_{max} - E_{min} = \delta E$ and $E_{min} = E_{ext}/2$. Injecting the simplified expressions above in the system 2.12, polynomial relations are obtained between the new variables:

$$\begin{aligned} X &= \exp\left(\frac{\Delta\mu_H}{2\mathrm{k_B}T_H}\right) \\ Y &= \exp\left(\frac{qV}{2\mathrm{k_B}T}\right) \end{aligned}$$

The charge balance equation becomes:

$$Y = A_1(T_H)X^2 + B_1(T_H)X + C_1(T_H) \tag{2.41}$$

with

$$\begin{aligned} A_1(T_H) &= \frac{f_1(T_H)}{f_3(T)} \\ B_1(T_H) &= \frac{f_3(T_H)}{f_3(T)} \\ C_1(T_H) &= -\frac{J_{abs}}{f_3(T)} \end{aligned}$$

Similarly for the energy balance equation:

$$Y = A_2(T_H)X^2 + B_2(T_H)X + C_2(T_H) \tag{2.42}$$

with

$$\begin{aligned} A_2(T_H) &= \frac{f_2(T_H)}{f_4(T)} \\ B_2(T_H) &= \frac{f_4(T_H)}{f_4(T)} \\ C_2(T_H) &= -\frac{P_{abs}}{f_4(T)} \end{aligned}$$

Here C_2 is independent of T_H. In a more generalized case where thermalization in the absorber is not neglected, a T_H dependent expression is obtained: $C_2(T_H) = (P_{abs} - P_{th}(T_H))/f_4(T)$. The resolution method can be applied in the same way.

By taking the difference of equations 2.41 and 2.42 a polynomial expression is obtained on X only

$$\alpha(T_H)X^2 + \beta(T_H)X + \gamma = 0 \tag{2.43}$$

$$\begin{aligned} \alpha &= A_2(T_H) - A_1(T_H) \\ \beta &= B_2(T_H) - B_1(T_H) \\ \gamma &= C_2(T_H) - C1(T_H) \end{aligned}$$

For a given T_H it is now possible to determine the positive root of that polynomial. Three situations are possible:

- no positive root: there is no stable state at this temperature
- one positive root: there is one unique stable state at this temperature
- two positive roots: two distinct states are found with different chemical potentials and voltages. The carrier temperature is not a monotonous function of the voltage (see figure 2.10), so this situation can occur and is not unphysical. In that case, two distinct branches of the $T_H(V)$ are found that correspond to the different roots, and merge into one unique curve.

Finally, $\Delta\mu_H$ is determined as a function of T_H, and the corresponding voltage V is calculated using equation 2.41 for instance.

2.2.6 Efficiency and losses

The chemical potential $\Delta\mu_H$ and the cell voltage V are determined at a given carrier temperature, which enables to determine the current density extracted from the cell, either by determining the radiative recombination J_{em} using equation 2.31

in the charge balance equation in system 2.12, or by computing the charge current at the contact in equation 2.14.

The current-voltage (IV) curves are then obtained, the electric power delivered by the cell is $P_{el} = J \times V$ and the efficiency is deduced:

$$\eta = \frac{J_e \times V}{P_{inc}} \times 100 = \frac{J_h \times V}{P_{inc}} \times 100 \tag{2.44}$$

The power lost from non absorption is then simply obtained :$P_{unabs} = P_{inc} - I \times V$, and the power lost due to radiative recombination is given directly by equation 2.32. A fraction of the energy of the extracted carriers is lost as they cross the contact. The net energy flux that cross a contact (for instance the electron contact) is given by the following equation:

$$P_e = P_e^+(\mu_e, T_e) - P_e^-(\mu_n, T) \tag{2.45}$$

but only a part of it contributes to the electric power because of entropy flux that accompanies the irreversible transport of carriers. The power lost in contact was defined as the difference between the power crossing the contact and the electric power:

$$P_{contacts} = \left(P_e^+(\mu_e, T_e) - P_e^-(\mu_n, T) + P_h^+(\mu_h, T_h) - P_h^-(\mu_p, T)\right) - I \times V \tag{2.46}$$

The sum of the converted power, the radiatively recombined power, and the power lost in contacts is equal to the absorbed power.

2.3 Results of simulations

The selective contacts are characterized by their transmission range δE, the transmission energy E_{ext}, and the contact degeneracy N. It is known that an ideal hot carrier solar cell would have a discrete transmission range, an infinite conductivity, and an extraction energy equal to the average energy of absorbed photons. In practice however, the contact conductivity and selectivity are not ideal, and one has to study the impact of these non idealities on the cell efficiency. The criticality of the contact parameters (selectivity, degeneracy and extraction energy) are studied. Optimal values of conductivity and extraction energy are determined.

2.3.1 Validation of the model

Before investigating the influence of the contact selectivity and conductivity on the cell efficiency, it is necessary to check that the model developed here is in agreement with the previous Ross-Nozik model for ideal hot carrier solar cells with perfectly selective contacts. By setting the contact energy range to a value that is small compared to the kinetic energy of carriers ($\delta E \ll \mathrm{k}T_H$), for instance 1 meV, and with a contact degeneracy that is large enough to ensure carrier extraction without resistance losses, the two models should give the same results, at least for large band gaps ($E_g > 0.5$ eV). In the case of smaller band gaps, the Boltzman approximation made above is not valid because the quasi Fermi level splitting is below the band gap by less than $\mathrm{k_B}T_H$. This model thus gives inaccurate results which might diverge from the Ross-Nozik model.

The efficiency and the different losses for the two models are presented in figure 2.6 as a function of the band gap, in full concentration condition. A very good agreement is observed over the whole band gap range, which shows the validity of the model in the limit of an ideal hot carrier solar cell. A validation in the limit of a fully thermalized solar cell will be proposed in section 4.3.1.

2.3.2 Criticality of the transmission range

If perfectly selective contacts were shown to give optimal conversion efficiency, provided that their conductance can be high enough, a quantitative analysis of the losses in contacts due to their non ideality is missing so far. A first attempt was proposed in [17] but only in the case of a 0 eV band gap absorber. The case of a more realistic 1 eV band gap is treated here. Two cases will be considered: first, a fixed extraction energy equal to the average energy of absorbed photons, second, with an optimization on the extraction energy in each configuration to have the maximal achievable efficiency. The first situation is interesting to see the evolution with only one varying parameter (the contact transmission range). However, in order to determine the ultimate achievable efficiency, it is more relevant to investigate the hot carrier solar cell behaviour in its optimal operating conditions. The contact conductance is taken optimal to enable maximal efficiency.

The cell efficiency, heat losses in the contact and radiative losses are plotted as functions of the contact transmission range in figure 2.7, either with a fixed extraction energy equal to the absorption energy (dashed line), or with an optimal extraction energy depending on the transmission range (solid line). The value of the optimal extraction energy as a function of the transmission range can be seen in figure 2.13. For $\delta E < 10$ meV , the efficiency is that of an ideal hot

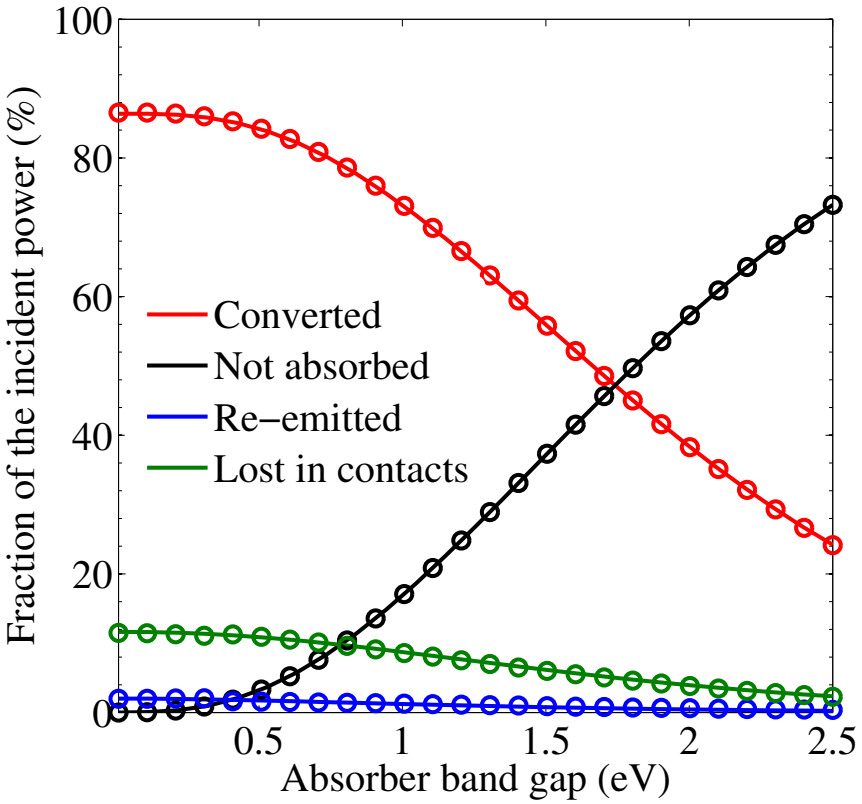

Figure 2.6: Fraction of the incident power that is converted (red), not absorbed (black), lost by radiative recombination (blue) and lost in the selective contacts (green), obtained using the Ross-Nozik model (empty circles), or with the hot carrier solar cell with non ideal selective contacts ($\delta E \ll \mathrm{k}T_H$) in the case of highly selective contacts (solid lines), under full concentration of the incident sun light. Very good agreement is obtained between the two models.

carrier solar cell. Both situations give the same efficiency, because the absorption energy is the optimal extraction energy with highly selective contacts. In that case, $\delta E \ll \mathrm{k_B}T$ so the contacts can be considered as a discrete level compared to the energy distribution of carriers.

With increasing transmission range, the cell efficiency (red) drops in the region $\delta E \sim \mathrm{k_B}T$, and the heat losses increase, as expected. In this region, optimized and fixed E_{ext} situations diverge. As the transmission range increases, the heat flow at

the contacts increases, and the carrier temperature is reduced. As a consequence, the density of high energy electrons is reduced. With an extraction energy that is unchanged, the current extracted is reduced and the radiative losses increase to balance the reduction of charge extraction, as can be seen in blue. When the extraction energy is optimized, the current is conserved and the radiative losses are unchanged. The heat losses at the contact (purple) are lower in the case of fixed extraction energy as a consequence of the lower current.

When δE becomes larger than 500 meV, the efficiency reaches a plateau, indicating that further increasing of the transmission range does not change the behaviour of the cell. In this configuration, the contacts are not selective, but form a high pass filter, allowing transmission only above (for electrons) or below (for holes) a threshold. $\delta E \gg k_B T$ so the upper bound of the contact is not seen by the carrier distribution and the contacts act as semi-selective contacts.

It is noticeable that the efficiency that is reached in the limit of such semi-selective contacts is higher than the Shockley-Queisser limit, which is about 40% in the present conditions. An efficiency of about 55% is obtained with extraction energy equal to the absorption energy, and as high as 60% with optimized extraction energy. It means that potential barriers, allowing carrier transmission at energies higher than a threshold, can thermally insulate the hot carrier population in a satisfactory way. A high pass filter is expected to be much easier to fabricate, especially considering the required conductance, than a band pass filter. One of the major technological lock in the making of a hot carrier solar cell, which is the extraction of carriers through selective contacts, could be adressed using one large band gap semiconductor forming an electron high pass filter and a blocking layer for holes, and symmetrically another one forming a blocking layer for electrons and a hole low pass filter (see figure 2.8). Such architecture provides a potential efficiency as high as 60% if thermalization losses in the absorber are neglected.

2.3.3 Optimal extraction energy

The impact of the extraction energy on a hot carrier cell efficiency has not been precisely determined so far. Würfel [1, 18] compared two models of hot carrier solar cells: a particle conservation model and a Auger recombination / impact ionization model, in which these processes are respectively considered negligible or dominant. In the first model, the effect of the extraction energy on the carrier temperature and chemical potential is discussed. It is shown that an extraction energy lower than the average energy of absorbed photons gives unphysical results. However, the impact on the cell efficiency is not considered. In the second model, the device efficiency is not affected by a change of the extraction energy if heat losses in the

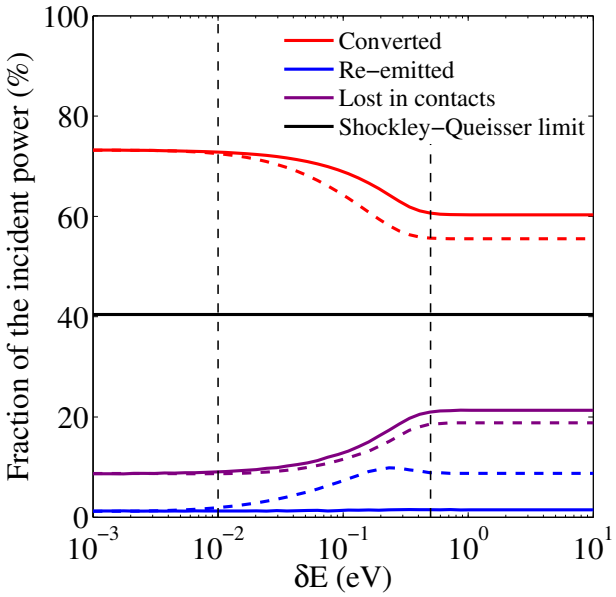

Figure 2.7: Efficiency (red), Heat flux in contact (purple) and radiative losses (blue) of a hot carrier solar cell as a function of the width of the contact transmission window, for a 1 eV band gap absorber under full concentration of incident light. First case (solid line): E_{ext} is optimized for each value of δE. Second case (dashed line): E_{ext} is fixed and equal to the absorption energy. The conductance is taken optimal in both cases. The Shockley-Queisser limit is 40% in that case (black line). Three regions are visible, separated by dashed black lines: high selectivity ($\delta E < 10$ meV), low selectivity ($\delta E > 500$ meV), and an intermediate selectivity between these two limit cases.

absorber are neglected. The same power is extracted with high current and low voltage (small extraction energy) or high voltage and low current (large extraction energy).

The model that is used here is derived from the particle conservation model, so the impact of the extraction energy has to be determined. In addition, thermal losses will be added in the energy balance. The relation between efficiency and extraction energy is affected by the thermalization rate as the available energy in the hot electron reservoir is reduced. Also, additional thermalization through contacts upon carrier extraction occurs with non ideal selective contacts that also affects the optimal extraction energy.

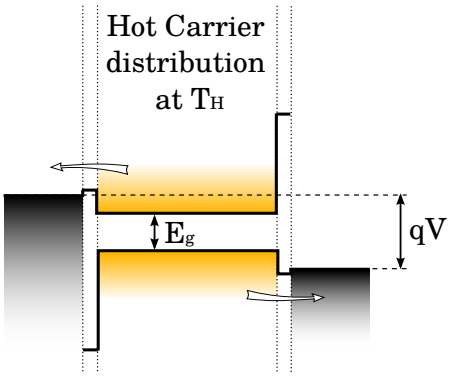

Figure 2.8: Simplified schematic of a hot carrier solar cell. A small band gap absorber with unequilibrated carriers is sandwiched between large band gaps layers working as a semi-selective contact for one type of carrier, and blocking layer for the other. The most energetic carriers are withdrawn towards their respective electrodes by jumping above the barriers.

The absorbed photons have an average energy $< E_{abs} >$ that is equal to the total absorbed power divided by the total absorbed photon flux integrated over energies.

$$E_{abs} = \frac{\int_{E_G}^{\infty} a(E) E^3 \left(\exp\left(\frac{E}{kT_S}\right) - 1 \right)^{-1} dE}{\int_{E_G}^{\infty} a(E) E^2 \left(\exp\left(\frac{E}{kT_S}\right) - 1 \right)^{-1} dE} \tag{2.47}$$

where $a(E)$ is the material absorptivity. The absorption energy is plotted in figure 2.9 as a function of the absorber band gap in the case of an absorptivity that is one above the band gap and zero below.

Even with large band gaps, the average energy of the absorbed photons is 0.5 eV larger than the band gaps. Using Boltzmann approximation, the absorption energy can be written:

$$E_{abs} = \frac{P_{abs}}{J_{abs}} = E_g + \mathrm{k_B} T_S \frac{1 + \frac{4\mathrm{k_B}T_S}{E_g} + \frac{6(\mathrm{k_B}T_S)^2}{E_g^2}}{1 + \frac{2\mathrm{k_B}T_S}{E_g} + \frac{2(\mathrm{k_B}T_S)^2}{E_g^2}} \tag{2.48}$$

When $E_g \gg \mathrm{k_B} T_S$, so for band gaps larger than 1.5 or 2 eV, the absorption energy can be approximated by: $E_{abs} = E_g + \mathrm{k_B} T_S$, which gives this 0.5 eV difference.

The absorption energy is also the average energy of the photogenerated carriers. For minimum losses, and in the case of neglected thermalization and ideal contacts,

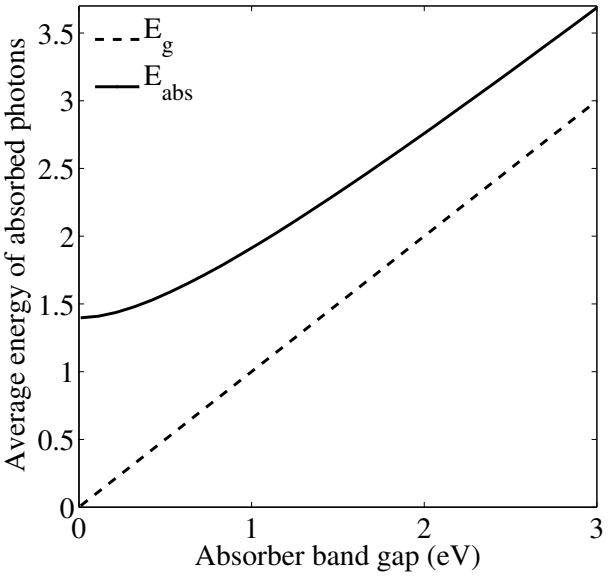

Figure 2.9: Average energy of absorbed photons (solid line) as a function of the absorber band gap (dashed line).

the extraction energy should be equal to this average energy, which would give the optimal conversion efficiency. For a symmetrical system, as described in 2.2.2, it means that $E_e = E_{abs}/2$ and $E_h = E_{abs}/2$. Here, only electrons with energy E_e and holes with energy E_h are extracted. However, carriers with energy higher and lower are not lost, as a high energy electron can promote a lower energy electron up to the contact level through carrier-carrier scattering which ensures the refill of the contact level as it is emptied because of extraction. This scattering is only a redistribution of the available energy and is not a loss. If the carrier-carrier scattering is fast enough, and neglecting Auger effect, all the absorbed energy can then be extracted. In steady state conditions, carriers are photogenerated and extracted at the same energy E_{abs} and at the same rate, with only a small amount of energy lost by radiative recombination and because of minimal entropy losses upon carrier extraction towards a cold reservoir.

For non ideal selective contacts, additional losses will occur in the contact, which may result in a lower carrier temperature in the absorber, and the optimal extraction energy is expected to be shifted towards lower energies.

Figure 2.10 presents the carrier chemical potential, carrier temperature, current

density and conversion efficiency as a function of the external voltage that are obtained in the case of a 1 eV band gap absorber with highly selective contacts ($\delta E = 1$ meV) under full concentration of the incident light for different extraction energies. Two regimes are distinguished: (i) the extraction energy is lower than the average energy of absorbed photons (E_{abs}), represented by the dashed-line curves, (ii) the extraction energy is above it, represented by the solid-line curves.

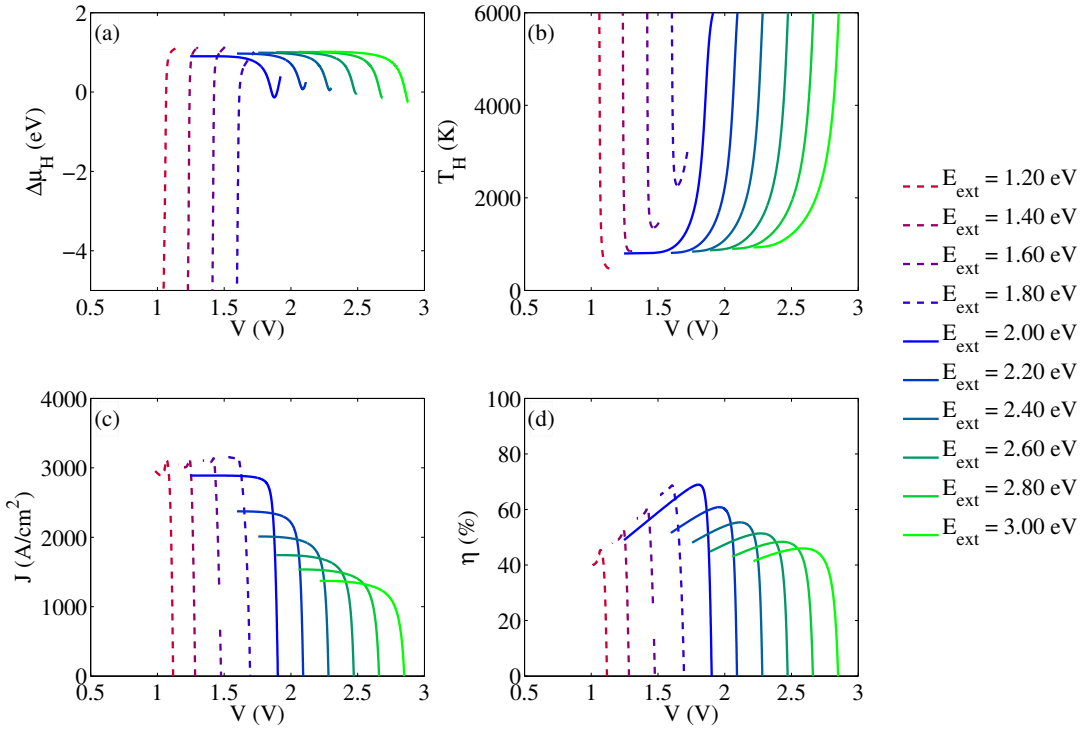

Figure 2.10: Carrier chemical potential (a), carrier temperature (b), current density (c) and delivered power (d) as a function of the external voltage for different extraction energies in the case of a 1 eV band gap absorber and highly selective contacts ($\delta E = 1$ meV) under full concentration.

In the second regime ($E_{ext} > E_{abs}$, the expected behaviour is observed, with a carrier temperature reaching 6000 K in open circuit conditions, and decreasing with the increasing amount of current that is extracted. The extraction of current in that case acts as a cooling of the carrier plasma, the carrier being generated at

energy E_{abs} and extracted at energy $E_{ext} > E_{abs}$. In open circuit conditions, the carrier plasma is at thermal and chemical equilibrium with the incident photon distribution, with radiative recombination balancing absorption. One can see that with the increase of the extraction energy, a raise of the open circuit voltage is obtained, counterbalanced by a reduction of the current density due to the reduced carrier density in the absorber at the energy at which they are collected. The resulting conversion efficiency is decreased with increasing extraction energy.

In the first regime ($E_{ext} < E_{abs}$, unrealistic results are obtained, with carrier temperature exceeding the sun temperature, and increasing rapidly with increased current. Such behaviour follows directly from the neglecting of thermal losses in the absorber. Without any way to dissipate the artifical heating coming from the withdrawal of the low energy carriers, the electron-hole plasma is heated unlimitedly as the current density increases. This should disappear with the introduction of thermalization in the model, which will be done in chapter 4. Here, carriers are collected with an energy $E_{ext} < E_{abs}$, and therefore below the carrier average energy. The withdrawal of a carrier corresponds to a heating of the remaining carrier plasma, as the low energy carriers are removed from it. At the same time, the chemical potential difference between electrons and holes diverges also towards very negative values, to maintain the conservation of carrier density. In steady state conditions, one electron hole pair is extracted with energy E_{ext}, and one is promoted with energy E_{abs}. The energy difference $E_{abs} - E_{ext}$ is then given to the hot electron-hole plasma which is heated to very high temperature. The efficiency is reduced at the smallest extraction energy, because the open circuit voltage is limited by it on the one side, and the current density is also limited by the photon current incident on the cell.

It can be noted that the $J(V)$ curves present some fluctuation at low voltage. This comes from a convergence issue: the carrier temperature and chemical potential diverging towards very large values, the ratio $\Delta\mu_H/\mathrm{k_B}T_H$ is not well defined, and so is the current. Also, a gap is visible in the $E_{ext} = 1.6$ eV curve. The two parts of the curves are given by different roots of the polynomial that is solved (see section 2.2.5) and the junction between the two parts is not perfect. This gap could be filled simply by refining the mesh on T_H.

The same data are represented in figure 2.11 in the same condition but in the case of non selective contacts ($\delta E = 1$ eV). In that case, the carrier temperature is lower, due to increased heat leakage through contacts. The same two regimes are observed with very high temperature and very negative chemical potential for extraction energies below a threshold, and more realistic results at higher extraction energies. The difference here is the value of that threshold, which is below the absorption energy.

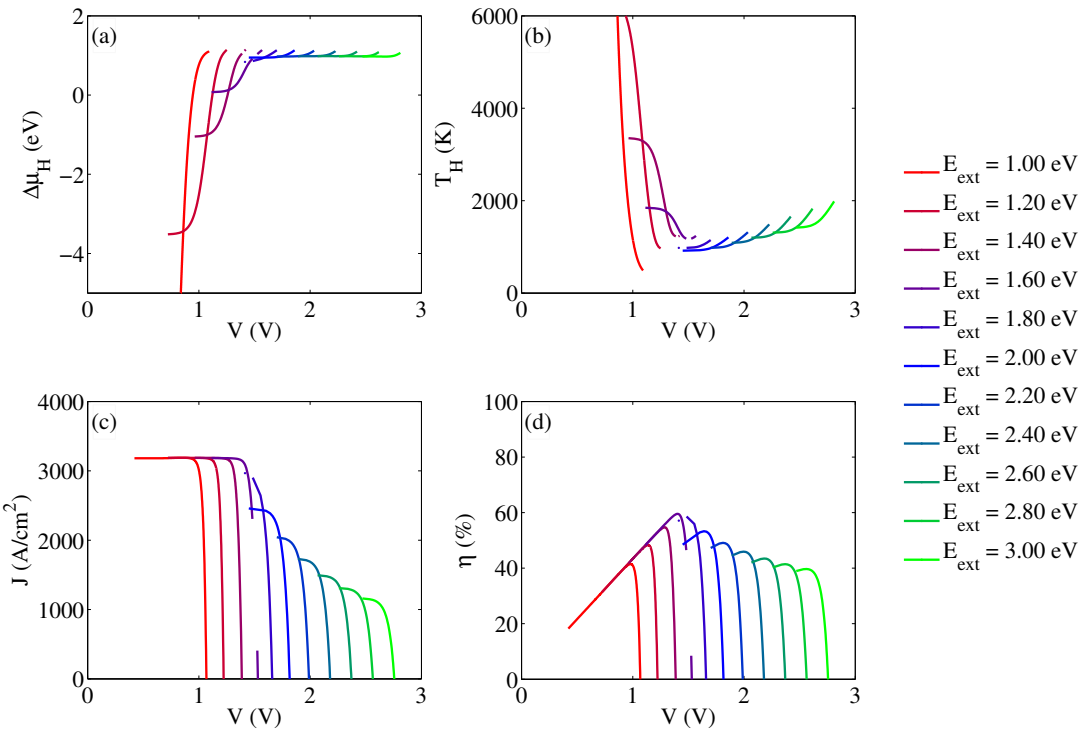

Figure 2.11: Carrier chemical potential (a), carrier temperature (b), current density (c) and delivered power (d) as a funciton of the external voltage for different extaction energies in the case of a 1eV band gap absorber and poorly selective contacts ($\delta E = 1$ eV) under full concentration.

The dependance of the efficiency on the extraction energy and the transmission range can be analyzed with figure 2.12 showing iso-efficiency curves in the δE-E_{ext} space, for a 1 eV band gap absorber under full concentration. The contact conductance (see section 2.3.4) is taken optimal. Three distinct regions are visible.

In the limit of very high selectivity ($\delta E < 10$ meV $\ll k_B T_H$ eV), contacts can be considered ideal and the optimal extraction energy is constant and equal to the absorption energy (provided the conductance can be as high as necessary). In a transition range between 10 meV and 500 meV, the efficiency depends both on the extraction energy and the transmission range. When δE is reduced, the maximum of efficiency is higher and occurs at a higher extraction energy. In the limit of

very low selectivity ($\delta E > 500$ meV), the efficiency becomes independant of the transmission range. This will be discussed in section 2.3.2. Here, the optimal extraction energy is a constant.

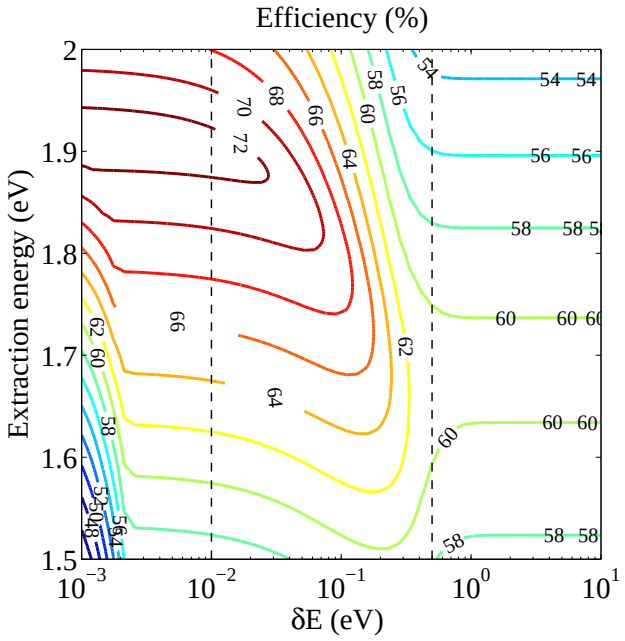

Figure 2.12: Iso-efficiency curves as a function of the extraction energy and the contact transmission range, for a 1 eV band gap absorber under full concentration. For small values of δE, the efficiency becomes strongly dependant on extraction energy, especially towards small values of E_{ext}. For large δE, the efficiency becomes independant on the transmission range and less dependant on the extraction energy. The different regions are separated by dashed black lines.

The dependance of the optimal extraction energy on the contact selectivity is shown in figure 2.13. It confirms that the optimal extraction energy equals the absorption energy (dashed line) in the limit of perfectly selective contacts. The three regimes are clearly visible, with a constant optimal extraction energy for $\delta E < 10$ meV, a δE-dependant optimal extraction energy between 10 and 500 meV, and a cell efficiency that becomes independent of the contact selectivity above 500 meV. With non selective contacts ($\delta E \gg 500$ meV), the optimal extraction energy is 1.68 eV, much larger than the absorber band gap (1 eV).

The efficiency, as well as radiative and contact losses are presented in fig-

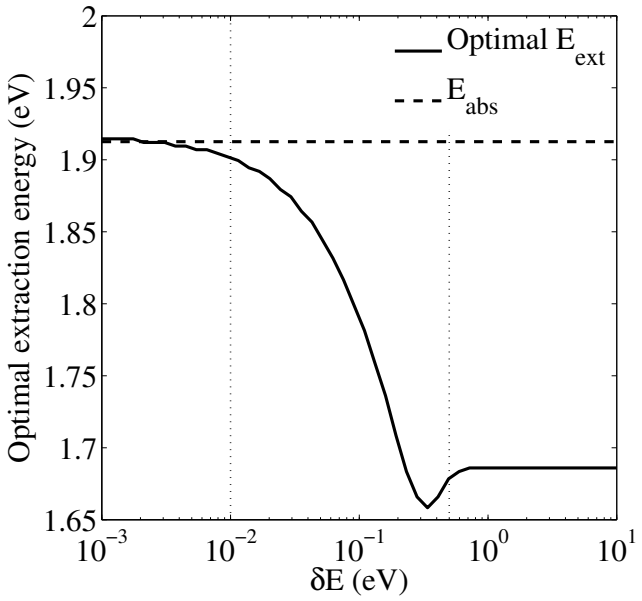

Figure 2.13: Optimal extraction energy vs contact transmission range for a 1 eV band gap absorber under full concentration. The three regions of high selectivity ($\delta E < 10$ meV), low selectivity ($\delta E > 500$ meV), and intermediate selectivity are separated by dotted lines.

ures 2.14, 2.15 and 2.16 as functions of the extraction energy, and for different values of the contact transmission range width, from 1 meV to 1 eV. It confirms that the optimal extraction energy for ideal hot carrier solar cell is the average energy of absorbed photons, and that it is shifted down when opening the transmission window. Here, the loss due to non absorption is constant and not presented, and neither is the thermal loss in the absorber that is neglected. One can see in figure 2.16 that for $E_{ext} < E_{abs}$, losses come from an increased heat flow in the contacts, due to high entropy flux upon the transport of carrier from an absorber at a very high temperature $T_H \gg T$ towards contact at ambient temperature. For $E_{ext} > E_{abs}$, losses are due to an increase of radiative recombinations (figure 2.15) because of a reduced current density. Particle conservation being ensured, carriers can either be extracted or recombined radiatively. If fewer carriers are collected (reduced current), more have to recombine.

With $\delta E = 1$ meV or $\delta E = 10$ meV, the cell behaves more or less like an ideal hot carrier solar cell, with an optimal conversion efficiency for $E_{ext} \simeq E_{abs}$. With,

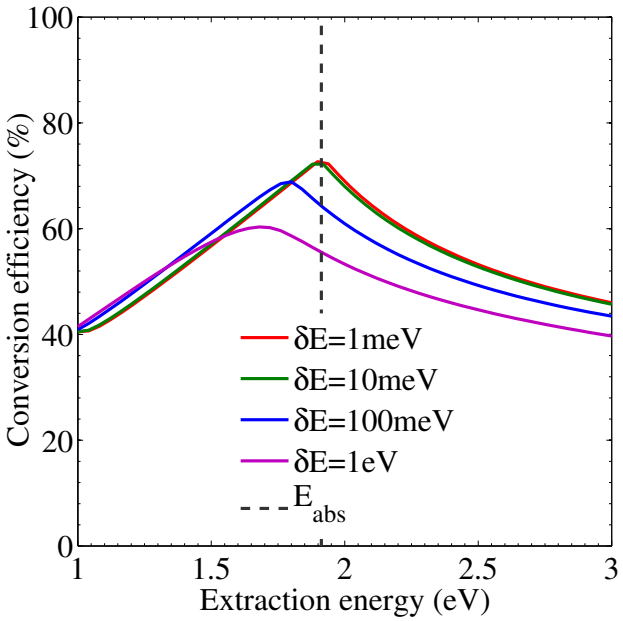

Figure 2.14: Conversion efficiency as a function of the extraction energy for a 1 eV band gap absorber with neglected thermalization under full concentration, and for different contact transmission widths from 1 meV to 1 eV. The dashed line stands for the absorption energy E_{abs}.

wider contact transmission range, the optimal extraction energy is shifted down. In that case, the heat flux through the contacts is larger, so the carrier temperature in the absorber is reduced, as can be seen on figure 2.11 compared to 2.10 (graph (b), carrier temperature vs voltage). The carrier average energy is then lower and they should be extracted at a lower energy.

One can notice also that the peak is sharper in the case of highly selective contacts. This means that a small variation of the extraction energy can strongly affect the cell performance if highly selective contacts are required, but it becomes less sensitive if poorly selective contacts are used. It also means that a hot carrier solar cell will be more sensitive to small variations of the incident spectrum with highly selective contacts than with non selective contacts.

Finally, the maximal efficiency that is obtained with highly selective contacts ($\delta E = 1$ meV$\ll$ kT_H) is 72.5% at $E_{ext} = 1.9$ eV, which is very close to the ideal hot carrier solar cell case ($\sim 72\%$), and is 60% at $E_{ext} = 1.68$ eV with non selective

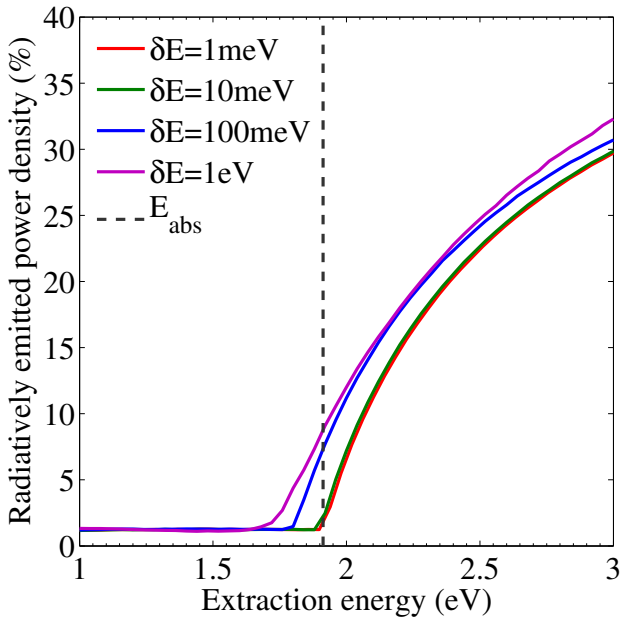

Figure 2.15: Radiative losses as a function of the extraction energy for a 1 eV band gap absorber with neglected thermalization under full concentration, and for different contact transmission widths.

contacts ($\delta E = 1$ eV$\gg$ kT_H). This value is much higher than the standard single junction limit ($\sim 40\%$).

2.3.4 Impact of contact conductance

The prefactor $2N/h$ in expression 2.14 is related to the conductance of the contact. N is the areal density of identical channels for carrier conduction through the selective contact, and $2/h$ is the quantum of conductance divided by the square of the charge of the electron (see [7]). The conductance of the contact can then be defined, in analogy to the conductance of a ballistic conductor defined in the Landauer formalism, as:

$$G = \frac{2Nq^2}{h} \tag{2.49}$$

in $\Omega^{-1}.cm^{-2}$.

One could expect that a large conductance is beneficial for carrier extraction without voltage drop. However, if the conductance is very high, it will result in

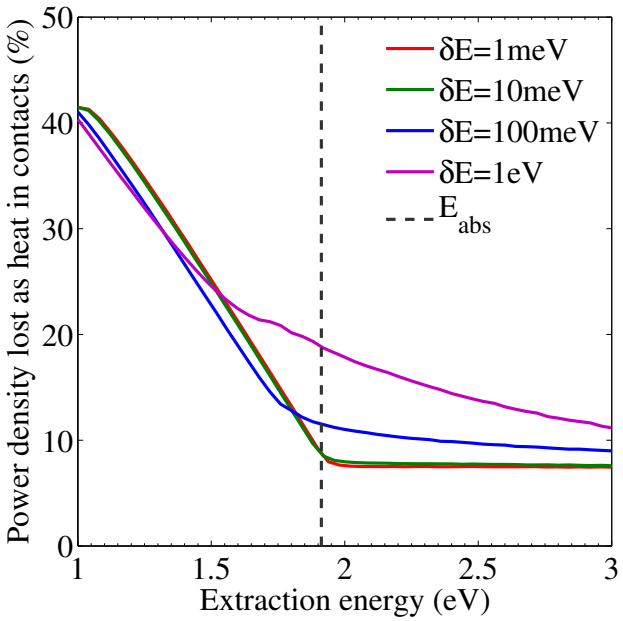

Figure 2.16: Heat losses in the contacts as a function of the extraction energy for a 1 eV band gap absorber with neglected thermalization under full concentration, and for different contact transmission widths.

an efficient heat exchange between hot and cold distributions. The net charge current extracted at a selective contact is the difference between currents from the absorber to the electrode and from the electrode to the absorber. When a high energy electron is extracted from the absorber and a low energy electron is injected in the absorber, the net current is zero but the amount of heat exchanged is the energy difference between these two electrons and is > 0. When the conductance is increased, the current extracted can be increased to some extent, beyond which only the heat flow increases with the rapid exchange of hot and cold electorns between the two populations, and the charge current saturates. One can therefore expect an optimal value of conductance that enables extraction of the photogenerated carriers without major heat losses in the contacts.

The efficiency is plotted in a $G{-}\delta E$ space in figure 2.17. Iso-efficiency curves are represented showing two different very distinct regions. For a contact transmission range below ~ 50 meV, the efficiency depends on both contact conductance and transmission range. The best efficiencies are obtained with the highest selectivity.

For each δE value, an optimal conductance is found. The efficiency raises sharply when increasing G, then a flat region is observed in a G range that depends on the contact transmission range, and the efficiency decreases at higher G. For δE above ~ 50 meV, the cell efficiency becomes independent of the transmission range. An optimal value for conductance is found but the efficiency variation is slower.

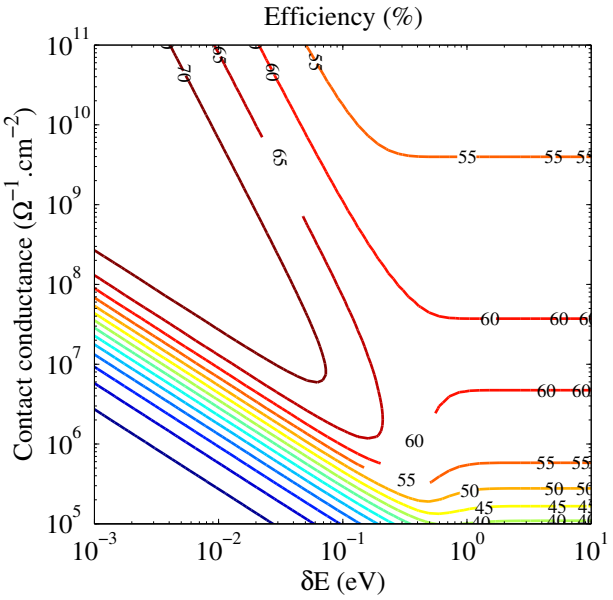

Figure 2.17: Iso-efficiency curves as a function of the contact conductance and transmission range for a 1 eV band gap absorber under full concentration and with optimized extraction energy.

The optimal conductance is plotted as a function of the contact selectivity in figure 2.18. In the high selectivity range ($(\delta E < 50$ meV), the optimal conductance decreases regularly with the increasing transmission range. This part of the curves can be accurately fitted with $1/\delta E^2$ law. In the limit of very narrow selective contacts, the current in equation 2.14 becomes, using a first order Taylor series in $\frac{\delta E}{\mathrm{k_B}T}$:

$$J = C_2 \frac{\delta E}{2} \left[\mathrm{e}^{\left(\frac{\Delta\mu_H - E_{ext}}{\mathrm{k_B}T_H}\right)} - \mathrm{e}^{\left(\frac{qV - E_{ext}}{\mathrm{k_B}T}\right)} \right] \tag{2.50}$$

In the case of an ideal hot carrier solar cell, the equation:

$$\frac{\Delta\mu_H - E_{ext}}{\mathrm{k_B}T_H} = \frac{qV - E_{ext}}{\mathrm{k_B}T} \tag{2.51}$$

is stated. It is expected that the term inside brackets in equation 2.50 should also tend towards 0 when $\delta E \ll k_B T$. It is plotted as a function of δE for highly selective contacts in figure 2.19. When δE tends towards 0, the plotted quantity becomes proportional to δE. It means that in the limit of perfectly selective contacts, the current can be written:

$$J \propto G\frac{\delta E^2}{2} \tag{2.52}$$

If the current is not zero, G is necessarily proportional to δE^2, which explains why the optimal conductance follows the trend in figure 2.18.

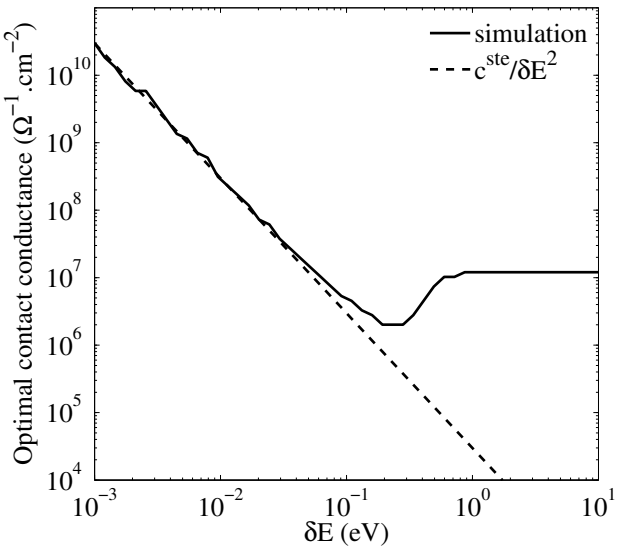

Figure 2.18: Optimal contact conductance as a function of the transmission range for a 1 eV band gap absorber under full concentration and with optimized extraction energy. The dashed line represents a conductance proportionnal to $1/\delta E^2$.

In the low selectivity range ($\delta E > 50$ meV), the optimal conductance is constant and close to 10^{11} Ω^{-1}.cm^{-2}. The optimal value would be reduced at lower concentration ratio, since lower current density would then be involved.

The efficiency as a function of the contact conductance is plotted in figure 2.20 for different values of contact transmission range: 1, 10, 100 meV and 1 eV. Heat losses in the contacts and radiative losses are also represented in figure 2.21

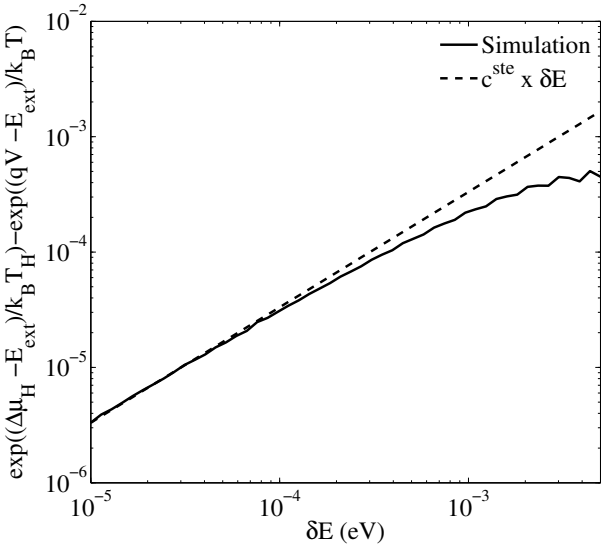

Figure 2.19: Term between the brackets in equation 2.50 as a function of the contact transmission range (solid line). In the limit of highly selective contacts (towards the left), it becomes proportionnal to the contact transmission range (dashed line).

and 2.22 respectively and with the same δE values. For highly selective contacts ($\delta E = 1$ meV), a flat maximum of efficiency is observed for conductance ranging from 10^9 to 10^{13} Ω^{-1}cm^{-2}. At lower conductance values, the efficiency drops drastically and the radiative losses increase in the same proportions. It means that the extracted current is too low and carriers that can not be extracted have to recombine. For higher values of conductance, no gain on charge current is made, but the power lost as thermalization in the contacts increases (purple curves) and the efficiency decreases.

For larger transmission range ($\delta E = 0.01$ to 1 eV), the same trend is observed but the range of conductance that gives optimal efficiency is reduced, and the optimal condutance is shifted down. This down shift comes from the integration over the energy range $[E_{ext}/2, E_{ext}/2+\delta E]$ in expression 2.14 and 2.15. For a given value of N, an increase of the energy range for integration leads to an increase of the transmitted charge and energy current. It then requires a smaller value of N, and finally of the contact conductance, to reach the optimal current density.

For very high values of the conductance, the heat loss in the contacts saturates and the cell efficiency reaches a limit, that is common for all values of the

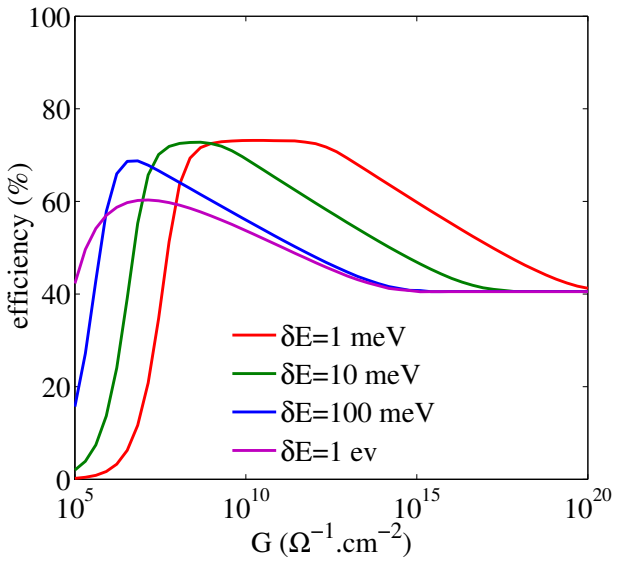

Figure 2.20: Efficiency of a hot carrier solar cell as a function of the contact conductance G for different contact transmission ranges: $\delta E = 1$ meV (red), $\delta E = 10$ meV (green), $\delta E = 100$ meV (blue), $\delta E = 1$ eV (purple). The extraction energy was optimized at each values of G ad δE. Simulations are performed in the case of a 1 eV band gap absorber under full concentration of sun light.

transmission range. This limit corresponds very precisely to the Shockley-Queisser limit in the present case (1 eV band gap and full concentration) and is 40.4%. This illustrates the importance of carrier extraction in a hot carrier solar cells: even if thermalization of carriers in the absorber is suppressed, no efficiency gain can be obtained if thermalization in contacts is not carefully tackled.

The order of magnitude obtained for the required conductance may raise the issue of the technological feasability of such contacts. If one considers a metallic layer, whose conductivity can reach 10^4 $\Omega^{-1}.\mathrm{cm}^{-1}$, the conductance is defined as the conductivity divided by the layer thickness. Values higher than 10^{10} $\Omega^{-1}.\mathrm{cm}^{-2}$ for the conductance with a layer thickness below 10 nm are possible. If one considers a degenerate semiconductor, its conductivity would be about three orders of magnitude lower, so only 10^7 to 10^8 $\Omega^{-1}.\mathrm{cm}^{-2}$ could be achieved. However, this concerns bulk conductivity where the carrier transport is controlled by scattering of charge carriers. In the case of a very thin conductor (below the mean free path of carriers), the transport is ballistic and only the access resistance at the interfaces

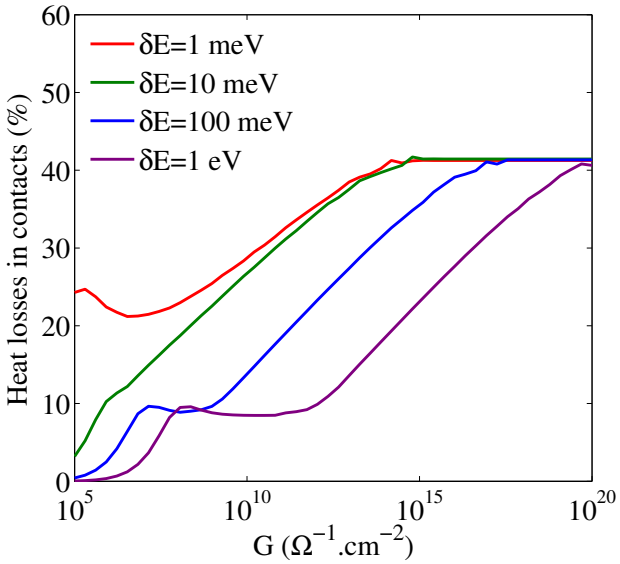

Figure 2.21: Heat losses in the contacts of a hot carrier solar cell as a function of the contact conductance G for different contact transmission ranges: $\delta E = 1$ meV (red), $\delta E = 10$ meV (green), $\delta E = 100$ meV (blue), $\delta E = 1$ eV (purple). The extraction energy was optimized at each values of G and δE. Simulations are performed in the case of a 1 eV band gap absorber under full concentration of sun light.

is involved. In that case, the contact conductivity is the quantum of conductance mutliplied by the density of transverse modes. The quantum of conductance is defined by:

$$G_0 = \frac{2q^2}{h} = 7.75 \times 10^{-5}\ \Omega^{-1} \sim 10^{-4}\ \Omega^{-1} \tag{2.53}$$

For a targeted value of $G = 10^{10}\ \Omega^{-1}.\text{cm}^{-2}$ for $\delta E = 1$ meV, the required density of modes would then be $10^{14}\ \text{cm}^{-2}$. In a bulk material, the carrier density of state is, as a function of the energy E:

$$g_{3D}(E) = \frac{1}{2\pi^2}\left(\frac{2m^*}{\hbar^2}\right)^{3/2} E^{1/2} \tag{2.54}$$

where m^* is the effective mass. In the case of GaAs for instance, the electron effective mass for electrons in the Γ valley is $m^* = 0.063m_0$, and the density of

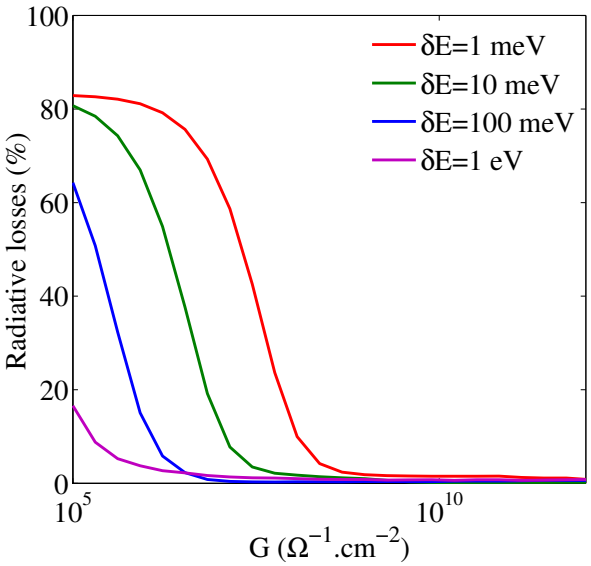

Figure 2.22: Radiative losses of a hot carrier solar cell as a function of the contact conductance G for different contact transmission ranges: $\delta E = 1$ meV (red), $\delta E = 10$ meV (green), $\delta E = 100$ meV (blue), $\delta E = 1$ eV (purple). The extraction energy was optimized at each values of G ad δE. Simulations are performed in the case of a 1 eV band gap absorber under full concentration of sun light.

states is $g_{3D}(E) = 10^{20}$ cm^{-3}.eV^{-1} at 1 eV above the band edge. If one considers a 10 nm thick material, 10^{14} modes are then available per eV and per square centimeter. When the transmission range is only 1 meV, it means that the density of modes for carrier transmission is only 10^{11} per square centimeter, much below the targeted 10^{14} cm^{-2}. This would give a conductance $G = 10^7$ Ω^{-1}.cm^{-2}, which, for very selective contacts, would only allow efficiency up to 20%. With a broader transmission range of 0.1 eV, 10^{13} cm^{-2} modes are achievable and a conductance of 10^9 Ω^{-1}.cm^{-2} would be possible, which is two order of magnitudes higher and above the optimal conductance (close to 10^7 Ω^{-1}.cm^{-2} here). In the case of tunneling through quantum dots or impurities, the situation would be even less favorable because of a lower density of transverse modes, limited by the density of dots or defects.

On figure 2.17, one can notice that the efficiency benefit when one goes from contacts having a transmission range of 100 meV to very selective contacts with 10 meV width or below is not obvious (see also figure 2.7), with a cell efficiency

increasing from 67% to 70%. On the other side, one has to pay a cost in term of contact conductance that seems prohibitive, since the optimal conductance goes from 10^7 to almost 10^9 $\Omega^{-1}.\mathrm{cm}^{-2}$. From the above analysis, such conductance may be unattainable. Having highly selective contacts appears to be not so useful in term of efficiency, and clearly a drawback regarding the required conductance.

Here, simulations are performed in full concentration condition. With lower concentration ratio, the required conductance would be reduced. Considering a proportional relation between the photocurrent and the incident flux, a concentration ratio of 1000 suns would imply an optimal conductance reduced by a factor 50, which should be more easily achievable.

The conductance of the contact is found to be a critical parameter in the cell efficiency. A small conductance leads to a reduction of the current density extracted from the absorber which strongly limits the efficiency. However, if the conductance is too large, heat leakage occurs at the contacts that reduces the carrier temperature and in the end also restricts the efficiency. The difficulty to achieve very high conductance could make very selective contacts, and their realization with low dimensional structures, incompatible with high efficiency.

2.4 Conclusion

The role of contact selectivity on the cell efficiency has been quantitatively investigated. Contrary to what was commonly admitted, a very high selectivity of the contacts is actually not crucial. Efficiency of 60% was obtained with semi-selective contacts allowing carrier transmission above an energy threshold, under full concentration. It is lower than the 73% efficiency obtained with ideal contacts in the same conditions, but is still a 50% relative efficiency improvement compared to the Shockley-Queisser limit. Such a high pass filter can be obtained with a large band gap layer, and may be much easier to work out than selective contacts using discrete levels (defects, quantum dot arrays) or tunnel junction, that proved themselves technologically challenging and incompatible with large current densities.

The question of contact conductivity is the second major limitation regarding selective contacts. The different ideas proposed to achieve carrier selectivity for contacts all involve tunneling, which would not favor large current densities expected for a device working under high concentration. It is pointed out that the contact conductivity decreases with the transmission range. Highly selective contacts would then strongly limit the possible extracted current, and would not be compatible with high conversion efficiencies. This is another argument in favor

of semi-selective contacts.

A new device architecture is proposed were large band gap materials replace the selective membrane and act as semi-selective contact for one type of carrier and as a blocking layer for the other. The height of the potential barrier would then determine the extraction energy, whose optimal value should be carefully determined depending on the concentration ratio (and on the thermalization rate, when it is considered).

Bibliography

[1] P. Würfel, A.S. Brown, T.E. Humphrey, and M.A. Green. Particle conservation in the hot-carrier solar cell. *Prog. Photovolt: Res. Appl.*, 13:277, 2005.

[2] R. Landauer. Electrical resistance of disordered one-dimensional lattices. *Philosophical Magazine*, 21(172):863–867, 1970.

[3] R. Landauer. Conductance from transmission: common sense points. *Physica Scripta*, 1992:110, 1992.

[4] M. Büttiker, Y. Imry, R. Landauer, and S. Pinhas. Generalized many-channel conductance formula with application to small rings. *Phys. Rev. B*, 31:6207, 1985.

[5] M. Büttiker. Four-terminal phase-coherent conductance. *Phys. Rev. Lett.*, 57:1761, 1986.

[6] Y. Imry and R. Landauer. Conductance viewed as transmission. *Reviews of Modern Physics*, 71:306, 1999.

[7] S. Datta. *Electronic transport in mesoscopic systems*. Cambridge University Press, 1995.

[8] LL. Chang, L. Esaki, and R. Tsu. Resonant tunneling in semiconductor double barrier. *Appl. Phys. Lett.*, 24:593, 1974.

[9] S. Yagi and Y. Okada. Fabrication of resonant tunneling structures for selective energy contact of hot carrier solar cell based on III–V semiconductors. In *Photovoltaic Specialists Conference (PVSC), 2010 35th IEEE*, pages 001213–001216. IEEE.

[10] G. Chen, G. Klimeck, and S. Datta. Resonant tunneling through quantum-dot arrays. *Phys. Rev. B*, 50:8035, 1994.

[11] G. Conibeer, C.W. Jiang, D. König, S. Shestha, T. Walsh, and M.A. Green. Selective energy contacts for hot carrier solar cells. *Thin solid films*, 516:6968, 2008.

[12] C.W. Jiang, M.A. Green, E.C Cho, and G. Conibeer. Resonant tunneling through defects in an insulator: modeling and solar cells applications. *Journ. Appl. Phys.*, 96:5006, 2004.

[13] W. Shockley and H.J. Queisser. Detailed balance limit of efficiency of *p-n* junction solar cells. *Journ. Appl. Phys.*, 32:510, 1961.

[14] R.T. Ross and A.J. Nozik. Efficiency of hot-carrier solar energy converters. *Journ. Appl. Phys.*, 53:3813, 1982.

[15] P. Würfel. The chemical potential of radiation. *J. Phys. C: Solid State Phys.*, 15:3967–3985, 1982.

[16] Y. Takeda, T. Ito, T. Motohiro, D. König, S. Shrestha, and G. Conibeer. Hot carrier solar cells operating under practical conditions. *Journ. Appl. Phys.*, 105:074905, 2009.

[17] M.F. O'Dwyer, T.E. Humphrey, R.A. Lewis, and C. Zhang. Electronic and thermal transport in hot carrier solar cells with low-dimensional contacts. *Microelectronics Journal*, 39:656–659, 2008.

[18] P. Würfel. Solar energy conversion with hot electrons from impact ionization. *Solar Energy Materials and Solar Cells*, 46:43, 1997.

Chapter 3

Experimental study of carrier thermalization

3.1 Hot carrier spectroscopy

Photoluminescence was early identified as an interesting tool to investigate carrier distributions in a semiconductor. In particular, it was used to study non equilibrium electron populations ("hot electrons") already in 1969 [1]. In this section, different methods for probing carrier thermalization from photoluminescence experiments are presented.

3.1.1 Continuous wave photoluminescence (CWPL)

The first experimental demonstration of a hot electron effect by photoexcitation was performed on GaAs using a continuous wave argon ion laser [1]. It was shown that the interband photoluminescence intensity decreases exponentially with photon energy in the high energy tail of the signal, indicating a Maxwellian distribution of carriers characterized by a temperature T_{e-h}. The intensity of the emitted signal from band to band carrier recombination and in the small photon energy interval $d(\hbar\omega)$ is given by the following expression [2]:

$$dI_{PL}(\hbar\omega) = A(\hbar\omega)\,(\hbar\omega)^2 \left(\exp\left(\frac{\hbar\omega - \Delta\mu_{e-h}}{\mathrm{k}T_{e-h}}\right) - 1\right)^{-1} d(\hbar\omega) \qquad (3.1)$$

where $A(\hbar\omega)$ is the material absorptivity, $\Delta\mu_{e-h}$ is the quasi Fermi level splitting, and T_{e-h} is the carrier temperature, assumed to be common to electrons and holes. The shape of the signal on the low energy side of the peak is related

to the absorption edge and depends on the absorptivity. On the high energy side, the absorptivity can be considered large and slowly varying compared to the exponential decrease of the signal, so the shape of the luminescence signal depends on the quasi-Fermi level splitting and on the carrier temperature. For energies high enough ($\hbar\omega - \Delta\mu \gg \mathrm{k}T$), the Bose-Einstein distribution can be approximated by a Maxwell-Boltzmann distribution and equation 3.1 can be written:

$$\begin{aligned} dI_{PL}(\hbar\omega) &= A(\hbar\omega)\,(\hbar\omega)^2 \exp\left(\frac{\Delta\mu_{e-h}}{\mathrm{k}T_{e-h}}\right) \exp\left(-\frac{\hbar\omega}{\mathrm{k}T_{e-h}}\right) d(\hbar\omega) \\ &\propto (\hbar\omega)^2 \exp\left(-\frac{\hbar\omega}{\mathrm{k}T_{e-h}}\right) d(\hbar\omega) \end{aligned} \tag{3.2}$$

The carrier temperature can therefore be determined from the high energy part of the luminescence intensity. It can be noted here that, the measured signal being an integration of the intensity in small wavelength intervals, the expression above needs to be modified with the introduction of the wavelength interval:

$$d\lambda = \frac{hc}{(\hbar\omega)^2} d(\hbar\omega) \tag{3.3}$$

and becomes for the integrated intensity over a discrete wavelength interval $\Delta\lambda$:

$$I_{PL}(\hbar\omega) \propto (\hbar\omega)^4 \exp\left(-\frac{\hbar\omega}{\mathrm{k}T}\right) \tag{3.4}$$

When the carriers are at thermal equilibrium with the lattice, the temperature that is obtained that way is the lattice temperature. However, it was found in that study that the shape of the spectra changes with the incident laser power, indicating that the carrier temperature T_{e-h} increases with an increase in the excitation power.

Information on the carrier energy loss processes to the lattice is obtained by analysing the dependance of the carrier temperature on the excitation power. In steady state conditions, the power input equals the power transferred to the lattice P_{th} (index th stands for thermalization). The experimental data for $1/T_{e-h}$ was shown to have a slope corresponding to the optical phonon energy [3, 4], indicating that scattering by optical phonons is the dominant energy loss mechanism for temperature exceeding 40 K in GaAs.

The existence of a steady-state Maxwell-Boltzmann distribution and the domination of LO phonon scattering process being established, these types of experiments were extended to other materials and higher excitation regimes [4]. Also,

processes of energy loss to acoustic phonons were investigated by studying the electron to acceptor luminescence [5].

Despite significant achievements with CWPL, difficulties emerged in the determination of absolute values of electron-phonon scattering rates. First, the power input in the electron-hole system, that is necessary to determine the energy loss rate, can be reasonably estimated but is always subject to some uncertainty. Second, both electrons and holes need to be considered, with holes coupled to the lattice by polar as well as deformation potential interaction, which adds some complexity to the problem. Finally, the density of carriers, that is expected to affect the carrier cooling rate, varies with the excitation power, introducing another variable in the problem.

Another approach in hot carrier spectroscopy using continuous wave photoluminescence is the investigation of the LO-phonon-emission cascade [6, 7]. When electrons are photogenerated high above the conduction band minimum, they relax by successive emission of LO phonons, resulting in an electron distribution composed of a cascade of peaks separated by the LO phonon energy. The signature of this distribution is a series of peaks in the high energy tail of the photoluminescence signal. These peaks are approximately 10^{-5} weaker than the band-gap-related photoluminescence. The analysis of the width and height of the series of high energy peaks as a function of the excitation energy allows to determine the electron-phonon scattering rate. This technique applies at rather low carrier density (10^{15} cm^{-3}). The polarization of the emitted signal was also investigated in [6]. When excited with a polarized light, the photogenerated carriers have an anisotropic momentum ditribution, which then results in a polarized photoluminescence. The scattering of carriers acts as a randomization of the carrier momentum that becomes more and more isotropic. The amount of polarized light in the PL spectrum can then be related to the carrier scattering rate.

3.1.2 Ultrafast spectroscopy

The different interaction mechanisms that govern the energy and momentum relaxation of carriers occur at very small time scales, and thus are difficult to observe experimentally. Typical time constants for the main mechanisms are proposed in table 3.1 (see [8]). In order to observe these ultrafast phenomena in the carrier dynamics, different techniques were developed, that were made possible thanks to the development of ultrafast pulsed laser.

The main advantage of these time resolved techniques is to provide a direct determination of the energy loss rate without the quantitative knowledge of the absorbed power by the electron-hole plasma. The different available techniques

Type of interaction	Characteristic time (s)
Carrier-Carrier scattering	$10^{-15} - 10^{-12}$
Intervalley scattering	$\geq 10^{-14}$
Intravalley scattering	$\sim 10^{-13}$
Carrier - Optical phonon interaction	$\geq 10^{-12}$
Optical phonon - Acoustic phonon interaction	$\sim 10^{-11}$
Auger recombination	$\sim 10^{-10}$
Radiative recombination	$\geq 10^{-9}$

Table 3.1: Typical time constants of various mechanisms in semiconductors [8].

are described below and reviewed in [8].

Pump-and-probe

In the pump-and-probe technique, an ultrashort laser pulse is separated into two pulses, a pump and a probe. The pump pulse excites the sample under investigation, causing a change in its properties. A weaker probe pulse then monitors these changes at a time delay Δt. By varying Δt, the time evolution of the investigated property is measured.

This technique may be used to study the reflection or transmission. In that case, the measured transmission or reflection can be related to the dynamic of the occupation at the energy level of the laser, which gives insights into the carrier relaxation dynamics. It can also be used to monitor time-resolved Raman scattering: the phonon population is investigated at different time delays after excitation by the probe pulse. Finally, time resolved photoluminescence can be performed using pump-and-probe technique. In that case, an up-conversion gate (see below) is used to scan the luminescence signal at a variable time delay.

Streak camera

A streak camera is a device that converts time information into spatial information. The light emitted from a sample that is photoexcited by an ultra short laser pulse is focused on a photocathode that releases an electron flux that is proportional to the incident light intensity. The electron flux is then accelerated and deflected by an applied voltage that sweeps the electrons across a phosphore screen. Electrons released at a different time will strike the screen at a different

position. The spatial intensity profile is then related to the temporal intensity profile of the photoluminescence. Streak cameras have a time resolution of a few picoseconds. Their use is limited to visible and near infrared luminescence.

Up-conversion gate

After an ultrashort excitation pulse, the photoluminescence signal is collected, collimated and combined with a probe pulse, called the gating pulse, in a nonlinear crystal. The angle of the crystal is set to phase match the frequency of the gating pulse with a selected frequency of luminescence. A signal whose frequency is the sum of the laser and luminescence frequencies is then measured by a photomultiplier. By varying the time delay of the gating pulse, the temporal profile of luminescence can be obtained. This technique provides a better time resolution than streak camera, and offers the possibiliby to scan further in the infrared.

Thermalization rate at high carrier density

The methods described above were used to study the carrier dynamics in semiconductors in the first picoseconds after photoexcitation. We will here focus on luminescence studies. The results obtained in the field of hot carrier spectroscopy are reviewed in [3].

A first attempt to make time-resolved photoluminescence spectroscopy with sub-nanosecond time resolution on GaAs [9] showed the domination of carrier-carrier scattering that ensures the establishment of a Maxwellian distribution, even at low carrier densities. However, carrier-phonon interactions occurs at a picosecond time scale and could not be directly observed. It first became possible with pump-and-probe techniques [10, 11, 12] for time-resolved absorption measurements.

However, there is a difficulty in interpreting absorption measurements, where transitions from heavy-holes, light-holes and splitt-off valence band contribute to the observed transmission changes. In contrast, the luminescence spectrum is dominated by recombinations with heavy holes and its interpretation is more straightforward. A first example of time-resolved photoluminescence is proposed in [13], still with GaAs at 4 K. It was shown that carrier-carrier scattering occurs with a very small time constant (below the 20 ps time resolution), followed by a carrier cooling from 90 K to 50 K within the first 150 ps. At 50 K, the carrier energy becomes lower than the threshold for LO phonon emission, and the thermalization rate is strongly reduced. The method was then applied to other materials such as InGaAs [14]. A time resolution below 500 fs was achieved [15], and intervalley

scattering rates could be measured in GaAs and InP at ambient temperature [16]. Time resolution of approximatively 100 fs was then achieved in [17].

In these experiments, the carrier temperature after photoexcitation is determined from the photoluminescence with a sub-picosecond time resolution. The time constant for carrier energy loss process is then determined directly from the $T_{e-h}(t)$ data. The first femtosecond of the carrier dynamics could be explored in [16], in the range of 0.5-1.5 ps after excitation, showing that the establishment of a Boltzmann-like distribution was almost instantaneous, with a carrier temperature higher than 600 K, even at low excitation intensity. It is shown that in the first picosecond, the PL signal rises, with a maximum of PL intensity 10 ps after excitation, because of intervalley scattering that brings back carriers from the L valley to the Γ valley (electrons in the L valley do not contribute to luminescence). This effect is much less pronounced in InP, because of a reduced intervalley scattering.

It was found from absorption experiments that, at low carrier density, the experimental energy loss rate was close to the theoretical value, but that it was unexpectedly slow at high excitation intensity [18]. Time-resolved photoluminescence experiments using up-conversion technique [19] confirmed this result. It was shown that the carrier energy loss rate in bulk GaAs was reduced above a critical carrier density of about 2×10^{18} cm^{-3}.

The first explanations proposed for the reduced cooling rate invoked a screening of the Fröhlich interaction [18, 20, 21]: the electromagnetic interaction between electrons and polar phonons is screened by the large density of carriers, which weakens the electron-LO-phonon coupling and results in a slowed phonon emission rate. It was theoretically investigated in [22], showing that the energy loss rate could be reduced by one order of magnitude when the screening of long range electron-phonon interactions at high carrier density was taken into account.

A second explanation invoked a hot phonon effect and was pointed out in [23]: the strong coupling between electrons and phonons leads to an out of equilibrium LO phonon population; the carrier cooling process is then limited by the LO phonon decay rate. The accumulation of nonequilibrium LO phonon faster than their decay is called the phonon bottleneck effect. In this process, the ability of a system to give rise to a hot phonon population is determined by the ratio between the net phonon emission rate (emission rate minus absorption rate), and the LO phonon decay rate. When the carrier density increases, the probability of a phonon to be reabsorbed by carriers increases, and the net phonon emission rate is reduced. In GaAs, the LO phonon decay time constant was measured to be approximatively 7 ps at 80 K [24]. If the carrier density is high enough so the reabsorption time is one tenth of that lifetime for instance, the cooling time is

increased by a factor of 10.

At high carrier density, coupled plasmon-phonon modes are involved, and a distinction between screening effects and hot phonon effects becomes almost impossible. The total electron-phonon population has to be considered as one unique system, with its own cooling rate [25]. However, theoretical studies incorporating both effects [26, 27] showed that the screening of the electron-phonon interaction plays a minor role in the slowing of carrier cooling. Experimental results of carrier temperature as a function of time was successfully fitted with a model in which the LO phonon population was determined accounting for electron-LO phonon scattering and LO-acoustic phonon anharmonic decay. They showed that the slowing of carrier cooling was due to an amplified LO phonon population that leads to the reabsorption of phonons by electrons. The effect of screening was even considered to accelerate the cooling of carriers in the way that the reduction of electron-phonon interaction would weaken the amplification of LO phonon and therefore limit the reabsorption by electrons.

Thermalization rate in low dimensional structures

A lot of interest was put into the study of carrier cooling rates in GaAs quantum well structures. The most commonly studied structures were GaAs/AlGaAs multi quantum wells and superlattices. A first experimental result by Shank *et al* [28] using pump-probe absorption measurement did not show a noticeable reduction in the carrier cooling rate compared to bulk at a carrier density $n = 2.5 \times 10^{17}$ cm^{-3}. However, another study by Xu and Tang [29] using picosecond photoluminescence showed that the carrier energy loss rate is much more carrier-density dependant in quantum wells than in bulk material. As a consequence, the carrier cooling rate is strongly reduced in quantum wells and becomes significantly lower than in bulk when the carrier density is higher than 10^{18} cm^{-3}. They also found that higher carrier temperatures were reached in QW than in bulk under high excitation. Another study [30] stated that the cooling rate measured in a modulation doped GaAs/AlGaAs multi quantum well was reduced by a factor 60 compared to the predicted rate using a three-dimensional nondegenerate-electron model.

Different hypotheses were proposed to explain this reduced thermalization in 2D systems: a modification of the energy loss rate could arise from a change either in the phonon emission rate or in the phonon decay rate. The effect of the reduced dimensionality on the optical phonon lifetime or a screening of the electron-phonon coupling by a high plasma density were rejected by Shah *et al* [31], in favor of a nonequilibrium LO phonon population in excess of what is expected in the 2D system. Leo *et al* [32, 33] then studied the influence of the well width

on the energy loss rate reduction. They showed that at high carrier density (up to 10^{18} cm^{-3}), the cooling rate was slower in thick wells (20 nm) than in the thin ones (3 nm). This difference however disappear when one considers the sheet carrier density rather than the volume carrier density as parameter. This indicates that the main effect in the energy loss rate reduction with 2D systems is the selection of wave vectors parallel to the plane of the well in the electron-phonon interaction. The phonon emission rate becomes therefore only dependent on the *sheet* carrier density, and independent of the well thickness. This is confirmed by theoretical studies highlighting the influence of interface modes in the electron-phonon scattering rate [34, 35]. The impact of a modification of the LO phonon lifetime by the material structuration would then play only a minor role. This was in agreement with a theoretical study of hot phonon effects in GaAs/AlGaAs systems [36].

The above conclusion however was only valid in the range of carrier density that was considered ($10^{15} < n < 10^{18}$ cm^{-3}). The problem was reexamined in the $2 \times 10^{18} - 1.5 \times 10^{19}$ cm^{-3} range by Pelouch *et al* [37], showing that the carrier energy loss rate was indeed reduced in 2D systems compared to bulk for carrier density higher than 2×10^{18} cm^{-3}. They found that the effect was stronger in thinner wells, and that the reduction becomes more pronounced with an increased photogenerated carrier density. Such energy loss rate reduction was related to an enhanced hot phonon effect because of a longer LO phonon lifetime due to the two dimensional confinement, in contradiction with previous conclusions. Those results were then confirmed in [19].

The energy loss rate reduction in 2D systems was similarly observed in other materials: InGaAs/InP [38], InGaN/GaN [39] for instance.

The long phonon lifetime in quantum structures is usually attributed to the opening of phonon band gaps in the dispersion relation. The major LO phonon decay process (one LO phonon decaying into tow acoustic phonons [40]) can be forbidden if there is no available state with half of the energy of the zone center LO phonon [41, 42] (see chapter 4).

3.1.3 Steady state and transient state

Time resolved techniques have been widely used to investigate the carrier thermalization rates in semiconductors, to the detriment of the continuous wave technique. The latter suffers from the lack of precision in estimating the power density injected in the system, that is necessary to have quantitative information about the carrier energy loss rate. By following directly the time evolution of carrier distribution, time resolved techniques enabled to bypass this difficulty.

However, in the case of solar cell application, the dynamics of the carrier in transient state is not a decisive information, since the cell operates in steady state condition. It is more useful to understand how the cell operate under a continuous excitation, and more specifically what is the achievable carrier temperature under a certain excitation intensity, and what part of the incident power density is lost to phonons. For that purpose, continuous wave photoluminescence is a more relevant tool.

Also, the dynamical thermalization rate φ_{dyn} that is observed with time-resolved technique is not necessary the same as the steady state thermalization rate φ_{st}. A relation between steady state and dynamical thermalization rates was proposed in [43]:

$$\varphi_{dyn} = \frac{C_{eh}}{C_{LO} + C_{eh}} \varphi_{st} \tag{3.5}$$

where C_{eh} and C_{LO} are the heat capacities of the carrier plasma and of the excited LO-phonon modes respectively.

The energy loss rate obtained by probing the transient carrier distribution in time resolved techniques is reduced by a factor that depends on the plasma contribution in the heat capacity of the coupled electron-hole plasma-LO phonon system compared to the steady state energy loss rate. This plasma heat capacity is not known in general, depends on the carrier and lattice temperatures, and can be difficult to determine. The energy loss rate that is determined using time resolved technique is therefore an underestimation of the actual steady state energy loss rate, and can not be used to determine the carrier distribution in steady state conditions. It is said in [43] that the heat capacity of the plasma is less than 15% of that of the LO phonon modes in the concentration and temperature ranges under consideration. The dynamical thermalization rate that is measured in time-resolved experiments is then reduced approximatively by a factor 10 compared to the steady state thermalization rate.

For those reasons, continuous wave photoluminescence will be used to investigate the thermalization properties of candidate materials for hot carrier solar cell application.

3.2 Description of samples

Materials and structures suitable for a hot carrier solar cell application have been identified. Several samples were synthesized and their thermalization properties were investigated.

3.2.1 Material selection

The hot carrier absorber application implies specific features that restricted the range of available materials. First of all, one can see in figure 2.6 that the hot carrier efficiency is highest with small band gap materials. When compared to figure 4.1, it is noticeable that the efficiency improvement with a hot carrier solar cell compared to a fully thermalized cell becomes important when one goes for band gaps below 1 eV. The absorber of a hot carrier solar cell is meant to have a rather small band gap. A band gap between 0.5 eV and 1 eV should be preferred. Below 0.5 eV, parasitic effects such as Auger recombinations and non radiative recombinations may compete with radiative transition and the thermalization will be less manageable.

Secondly, a large carrier density will be beneficial for thermalization reduction. For that, it is interesting to absorb light in the smallest possible volume of material. A direct band gap is therefore required.

Also, nanostructuration of the material may play a determinant role in the control of thermalization. III-V semiconductors give the possibility to grow films with a high cristallographic quality and a very good control of thickness. They also provide good absorption. For these reasons, they are the best candidates for our application.

In figure 3.1 that represents the position of the common binary III-V semiconductors in the band gap - lattice constant space, only one binary compounds meets the above requirements: GaSb. Different ternary or quaternary compounds can also be formed with a lattice constant very close to that of GaSb and with band gaps ranging from 0.4 eV (InAs) to 2.4 eV (AlSb), which enables to synthesize a large variety of heterostructures of type I, II or III. Finally, the small effective mass and phonon energy in GaSb can be beneficial to obtain a small carrier thermalization rate.

The focus was put on two different materials with a band gap of 1.9 μm (0.66 eV):

- a ternary $Ga_{0.8}In_{0.2}Sb$ in compressive strain on a GaSb substrate
- a quaternary $Ga_{0.86}In_{0.14}As_{0.12}Sb_{0.88}$ lattice-matched with GaSb

Different structures have been tested for each of these compounds, which are listed in table 3.2.

The samples were grown by Molecular Beam Epitaxy (MBE) on n-type doped (in the 5-8$\times 10^{17}$ cm^{-3} range) epi-ready GaSb [100] substrates. The MBE machine used is a Varian Gen II molecular epitaxy reactor equipped with tellurium (Te) and beryllium (Be) dopant cells, and valved cracker cells for both arsenic and antimony. Growth rates were set at 0.5 monolayer per second (ML/s) for both

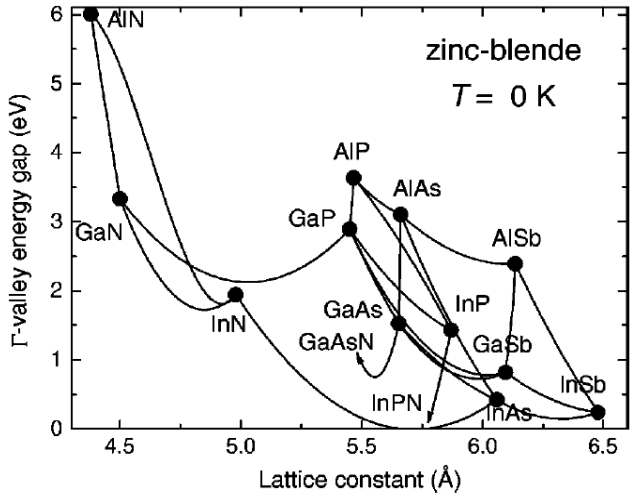

Figure 3.1: Lattice constant and band gaps of III-V semiconductors at 0 K

indium (In) and gallium (Ga) and 1 ML/s for both arsenic (As) and antimony (Sb). Prior to the growth, the substrate was outgassed for several hours at 150℃ inside the introduction chamber, then loaded in the growth chamber and heated for 20 minutes at 550℃ under Sb flux for oxide removal. The n-type doped GaSb (Te-doped) buffer layer was then deposited at 510℃, followed by the growth of the MQW structure at 400℃ and of the p-type doped GaSb (Be-doped) bottom contact layer. In situ RHEED (Reflection High Energy Electron Diffraction) has been used for monitoring the sample surface evolution during the growth. More specific details on optimum growth conditions, i.e. growth rates, temperature, V/III ratio, strain adjustment and MBE shutter sequence to realize high-quality GaSb-based samples will be reported elsewhere on comparable GaSb systems [44].

3.2.2 Strained samples

A first series of samples were multi quantum wells made of a ternary compound in compressive strain on a GaSb substrate. This series is composed of samples V641, V642, V809 and V812.

V641 an V642

Sample V641 consists in a strained MQW structure on a n-doped GaSb substrate covered by an n-doped (2×10^{18} cm^{-3}) GaSb buffer layer. The active region is composed of 5 periods of a 8 nm-thick InGaSb well and 27 nm-thick GaSb barrier. The targeted fraction of indium in the well is 20% for an expected luminescence at 1.93 μm at ambient temperature. This results in a lattice mismatch $\Delta a/a = 1.25\%$ on the GaSb substrate. The structure is then capped by a p-doped (2×10^{18} cm^{-3}) GaSb contact layer.

Sample V642 is similar to V641, with a $Al_{0.35}Ga_{0.65}As_{0.03}Sb_{0.97}$ barrier replacing the GaSb barrier. It is a quaternary compound lattice-matched on GaSb and with a higher band gap. It leads to deeper wells and therefore to an increase of the electron and hole ground state energies. The luminescence is expected at 1.87 μm. The structures of samples V641 and V642 are proposed in figures 3.2 and 3.3.

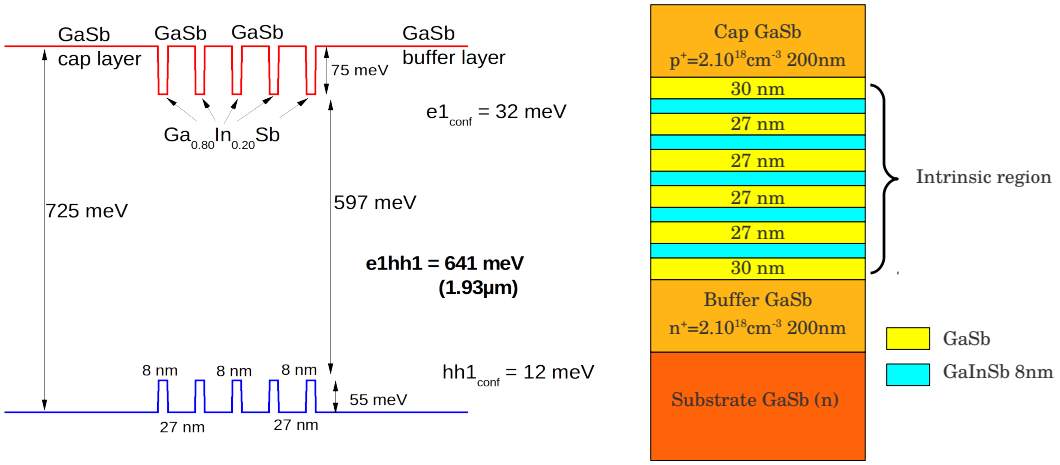

(a) Band offsets in V641 sample

(b) Schematic of the V641 sample stack

Figure 3.2: Band offset (a) and structure (b) of sample V641

High resolution X-ray diffraction (HRXRD) experiments were performed on these samples to check the composition and thickness of the deposited layers. The measured and simulated spectra are presented in figure 3.4. The comparison between measurement and simulation indicates a 35.5 nm period, close to the expected 35 nm period, and a 17% indium content, slightly shifted from the targeted 20% content.

These samples were test structures, showing that a very good control of the well

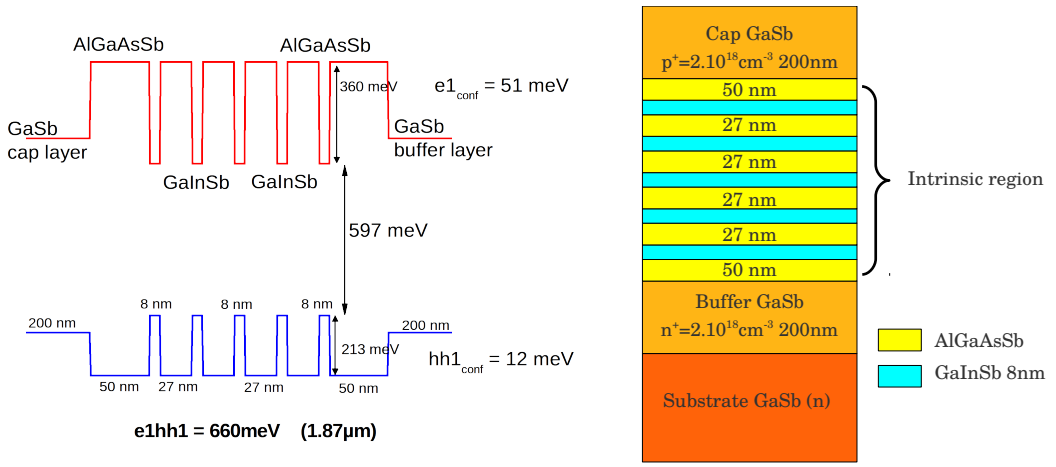

(a) Band offsets in the V642 sample (b) Schematic of the V642 sample stack

Figure 3.3: Band offset (a) and structure (b) of sample V642

thickness and material crystallinity could be achieved. Luminescence was obtained on sample V641 at ambient temperature. The feasibility of the photoluminescence measurement on such material being established, the focus will be put on other more promising samples.

V809 and V812

V809 and V812 samples were inspired from V641, with thicker wells. Cladding layers were added for sample V812 to ensure the carrier confinement in the well region. The band offset is presented in figure 3.5.

As can be seen in figure 3.5, the multi-quantum wells (MQW) structures consisted of a 200 nm thick Te-doped ($n = 1 \times 10^{16}$ cm^{-3}) GaSb buffer layer, an undoped region made of 5 MQW containing five 10 nm-thick $GaIn_{0.2}Sb_{0.8}$ compressively strained wells and six 20 nm-thick GaSb barriers, and 100 nm thick of GaSb cap layer (V809). The V812-structure is the same as the previous one but with 20 nm thick AlSb barriers surrounding the MQW region. The conduction and valence band-offset ΔE_c and ΔE_v were calculated by interpolating binary heterointerface values followed by calculation of shifts due to strain. The numerical values used to calculate the band diagram and the electrons and holes energy levels and wavefunctions were extracted from reference [45].

XRD experiments were performed on samples V809 and V812 and are presented

in figure 3.6. The two XRD curves are very similar, confirming the excellent reproducibility of the growth method. In the V812 curve, an additional peak corresponding to AlSb is visible, indicating the presence of the cladding layers in the structure.

Cladding layers in sample V812 play the role of blocking layers for electrons and holes. It prevents them from being scattered outside of the active region, which has a double interest: it limits the heat flow outside of the excited electron-hole plasma, and maintains a high carrier density, which can facilitate the establishment of a hot carrier population.

3.2.3 Lattice-matched samples

The second series of samples consists in multiquantum wells made of lattice matched quaternary compounds. It is composed of samples V725, V1078 and V1231.

V725 and V1078

Samples V725 and V1078 are multi-quantum well structures on a GaSb substrate, with lattice matched well and barrier materials. It is designed in order to exhibit luminescence at 1.9 μm at ambient temperature (similarly to previous samples). Cladding layers, also lattice matched with GaSb, are inserted in the structure on both side of the well region.

The V725 well region is composed of 5 times 10 nm thick wells and 30 nm thick barriers. Sample V1078 differs in the barrier thickness which is only 20 nm. The well material is $Ga_{0.86}In_{0.14}As_{0.12}Sb_{0.88}$ with a 0.58 eV band gap at ambient temperature (see section 3.4.1 for band gap determination of alloys). The barrier compound is $Al_{0.25}Ga_{0.75}As_{0.03}Sb_{0.97}$ with a 1.03 eV band gap. Large band gap cladding layers made of $Al_{0.9}Ga_{0.1}As_{0.07}Sb_{0.93}$ ensure carrier confinement in the active region. A schematic of the band offset and material stack is proposed in figure 3.7.

The active regions of samples V725 and V1078 are almost identical, and only results on sample V725 will be presented here. A 20 nm thick $InAs_{0.98}Sb_{0.2}$ is inserted in sample V1078 between the substrate and the active region. This layer can later be used as a blocking layer for a chemical etch of the substrate. The sample can be reported on a glass substrate with a metallic coating, so the GaSb substrate can be removed. The active region alone, composed of the quantum wells and the cladding layers, can then be obtained.

V1231

Sample V1231 has an absorbing layer with the same composition as V725 or V1078, but consists in only one 50 nm thick layer instead of a 5×10 nm quantum well structure. It is sandwiched by two layers of the AlGaAsSb barrier compound of 60 nm each. Without confinement, the band gap is reduced compared to QW samples, with emission at 2.1 μm at 300 K instead of 1.9 μm for other samples.

The absorbing thickness (well + barrier) for photoluminescence experiments is the same as sample V1078, and the total volume of the well material is similar to samples V725 and V1078. The idea here is to investigate the effect of carrier confinement and material structuration on the thermalization properties of the material, by comparing quantum structures and bulk-like material in the same conditions of illumination.

Name		Composition	Thickness	λ_{em}
V641	Well	$Ga_{0.83}In_{0.17}Sb$	5×8 nm	1.90 μm
	Barrier	GaSb	6×27 nm	
V642	Well	$Ga_{0.83}In_{0.17}Sb$	5×8 nm	1.87 μm
	Barrier	$Al_{0.35}Ga_{0.65}As_{0.03}Sb_{0.97}$	6×27 nm	
V809	Well	$Ga_{0.8}In_{0.2}Sb$	5×10 nm	1.90 μm
	Barrier	GaSb	6×20 nm	
V812	Well	$Ga_{0.8}In_{0.2}Sb$	5×10 nm	1.90 μm
	Barrier	GaSb	6×20 nm	
V725	Well	$In_{0.14}Ga_{0.86}As_{0.12}Sb_{0.88}$	5×10 nm	1.90 μm
	Barrier	$Al_{0.25}Ga_{0.75}As_{0.03}Sb_{0.97}$	6×30 nm	
V1078	Well	$In_{0.14}Ga_{0.86}As_{0.12}Sb_{0.88}$	5×10 nm	1.90 μm
	Barrier	$Al_{0.25}Ga_{0.75}As_{0.03}Sb_{0.97}$	6×20 nm	
V1231	Well	$In_{0.14}Ga_{0.86}As_{0.12}Sb_{0.88}$	50 nm	2.10 μm
	Barrier	$Al_{0.25}Ga_{0.75}As_{0.03}Sb_{0.97}$	2×60 nm	

Table 3.2: List of the investigated samples with their respective composition and structure and the wavelength of luminescence λ_{em} at 300 K.

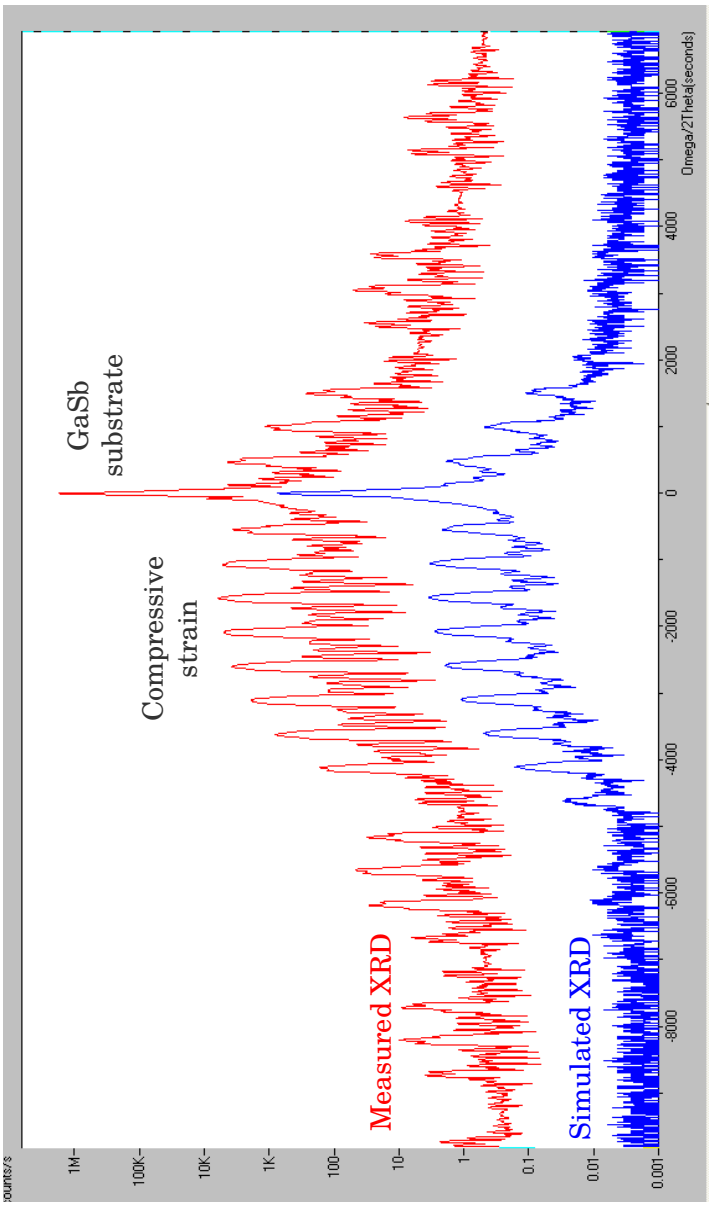

Figure 3.4: Simulated (blue) and measured (red) XRD signal of sample V641. The main peak comes from GaSb. The envelope of the signal can be related to the compressive strain. The fit of the secondary peaks with simulation indicates a 17% indium content in the well, slightly shifted from the targeted 20%. A 35.5 nm period (well plus barrier) is observed in good agreement with the expected 35 nm (27+8) period.

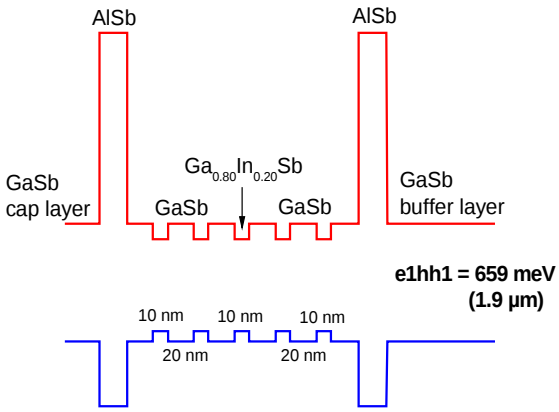

Figure 3.5: Schematic of the band offsets of sample V812

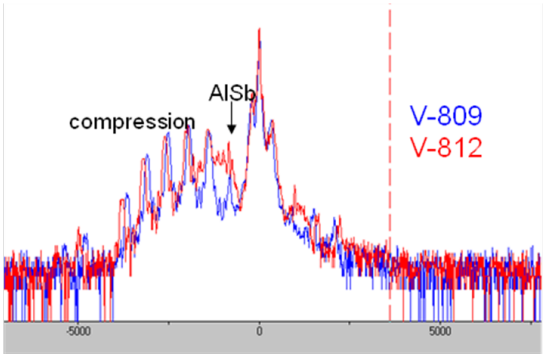

Figure 3.6: High resolution X-ray diffraction (HRXRD) measurements on strained samples V809 and V812

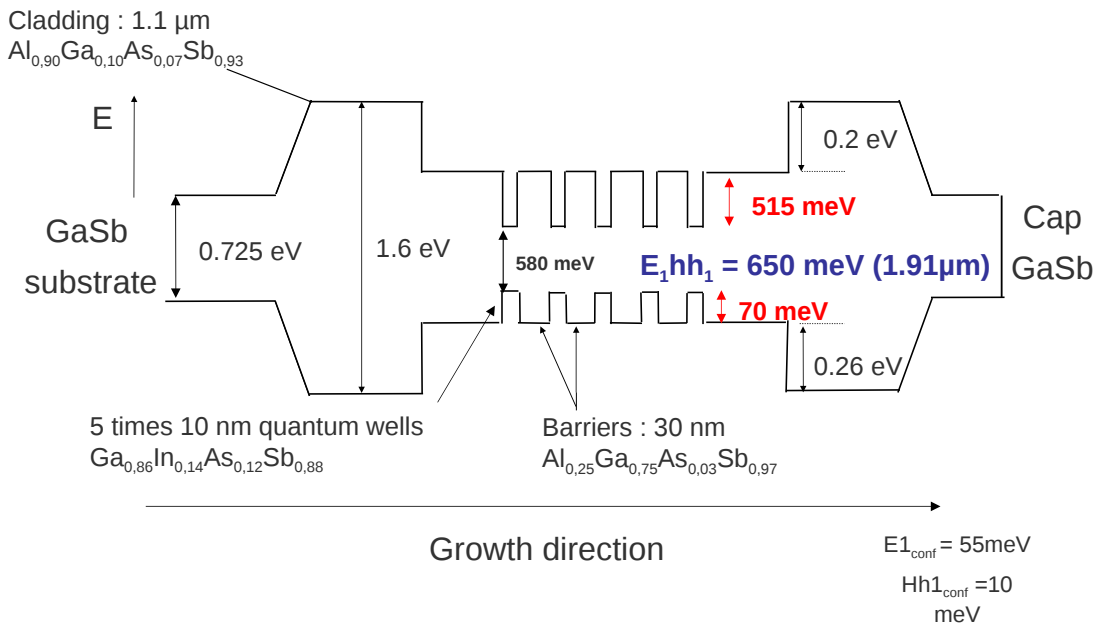

Figure 3.7: Schematic of the band offsets in sample V725.

3.3 Experimental setup

The samples were characterized by continuous wave photoluminescence. Carriers are photogenerated in the sample by a laser excitation, and the spectrum emitted from the radiative recombinations is collected and measured.

This measurement is performed at different excitation power. When increasing the laser power, the photogenerated electron-hole plasma can no longer equilibrate with the lattice. The temperature of the carriers raises with the excitation power and the relation between the temperature rise and the incident power provides information on the thermalization properties.

This study is carried out at different lattice temperature. The phonon involved in carrier thermalization being thermally activated, it is expected that the thermalization rate will depend on the lattice temperature. For that reason, the PL measurements were carried out in a cryostat for temperature controlled experiments.

Two different setups were used: one setup at Chimie ParisTech (setup A), another at IRDEP (setup B). They differ from each other in the excitation and collection configuration and in the equipment.

3.3.1 Setup A

(See figure 3.8)

Excitation

The excitation source was a tunable Ti-sapphire laser pumped by an argon-ion laser. It was used in the 750-900 nm range. Beyond 900 nm, the power delivered by the laser decreases, which is unfavourable for high injection power-dependant PL experiments. Under 750 nm, however, the claddings in some of the sample would absorb a part of the incident light, and the absorption in the absorbing layer would have been lower (and harder to estimate). The power delivered by the laser was about 600 mW, depending on the chosen wavelength.

The laser beam was sent on the sample with a 45° angle with the sample surface.

Neutral density filters were used to tune the incident power from 100% to below 0.01%, depending on the intensity of the collected signal.

Collection and measure

The signal was collected with two lenses with a focal length of 10 cm (NA$\approx$ 0.4) imaging the excited spot on the slit of a monochromator. The monochromated

signal was then sent on a PbS photodetector cooled at 80 K with liquid nitrogen.

The optical axe of the collection system made a 45° angle with the surface of the sample.

Temperature control

The sample was placed in the chamber of a liquid helium cryostat, reaching temperature down to 10 K. Thermal contact between the sample and the cold finger of the cryostat was ensured using a silver paste. Some experiments were performed at 10, 20 or 30 K, but most were performed at temperature between 50 and 100 K, which is a more relevant temperature range for thermalization study. The cryostat was not very stable at higher temperature.

3.3.2 Setup B

(See figure 3.9)

Excitation

The excitation source was a near infrared laser diode emitting at 781 nm. It delivered a power of about 90 mW

The laser beam was coupled in a multimode optical fiber, then collimated to enter a microscope objective. Two configurations were possible: a high power configuration where the beam was transmitted by a beam splitter with 92% transmission, or a low power configuration where the beam was reflected by the beam splitter (8% reflexion). Accounting for losses in the fiber, objective and other optics, the power incident on the sample was finally 17 mW in the high power configuration, 0.7 mW in the low power configuration.

The same neutral density filters were used to tune the incident power.

Collection

The signal was collected by the objective having a 11 mm working distance and a 0.6 numerical aperture (NA). It is then reflected/transmitted by the beam splitter (depending on the configuration, see figure 3.9(a) and 3.9(b)).

The signal was then coupled in an optical fiber and sent in a spectrometer. It is an Ocean Optics NIR256 spectrometer, composed of a 256 pixels InGaAs detector with a detection ranging from 900 to 2500 nm and cooled with a double Peltier plate at -10°C.

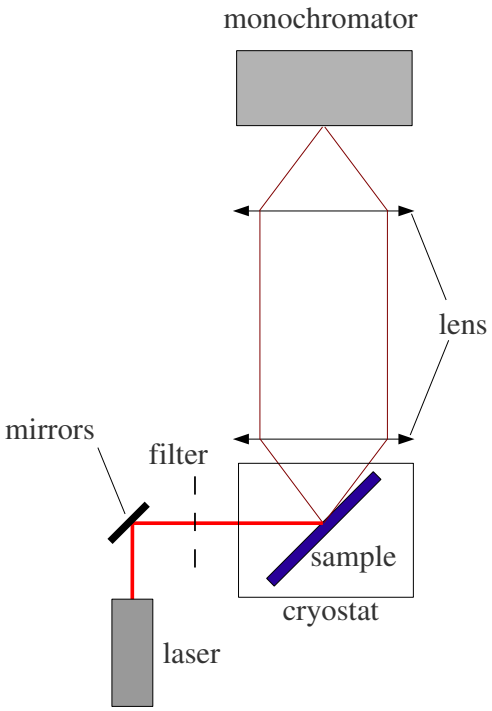

Figure 3.8: Schematic of the experimental setup A. The sample is placed in the cryostat chamber, its surface making a 45° angle with the laser beam, and with the optical axis of the collecting optics. The collecting optics consist in two lenses with a focal length of 10 cm imaging the excited spot at the entrance of a monochromator. The monochromated signal is then sent onto a PbS photodetector that is cooled with liquid nitrogen.

Temperature control

The samples were put in a cryostat chamber, here again glued with silver paste for thermal contact. The cryostat used was a nitrogen cryostat, with a minimum reachable temperature of 80 K.

3.3.3 Comparison

The features of the two setups are summed up and compared in table 3.3. Setup A has very good features in terms of detector sensitivity compared to setup B, due to the liquid nitrogen cooled detector. Also, the excitation power is much

higher. However, the focusing of the excitation laser in setup B allows reaching higher power density than in setup A in spite of a lower laser power.

Above all, the very good control of the spot size with the microscope objective in setup B enables a precise determination of this power density, which is not possible in the other setup, where only a rough estimation is possible. This power density is a key parameter for a quantitative determination of thermalization properties. For that reason, and despite a poor sensitivity, setup B is expected to provide more accurate results.

Features		Setup A	setup B
Excitation	Incident power	600 mW	17 mW
	Laser wavelength	750-900 nm	781 nm
	Spot size	$\sim 10^{-3}$ cm^2	5.10^{-6} cm^2
	Power density	6.10^2 W/cm^2	3.10^3 W/cm^2
Collection	Detector sensitivity	very good	poor
	Detector resolution	~ 1 nm	>6 nm
	Acquisition time	~ 1 minute	20 ms
Temperature	Accessible range	10-100 K (unstable)	80-300 K

Table 3.3: Comparison of the two photoluminescence setups.

The results obtained with the two different setups with a test sample are shown in figure 3.10 for comparison. The sample was a 75 times 8.5 nm thick InGaAs wells and 10 nm thick InP barriers on an InP buffer and with a 81 nm thick InP capping layer. Its band gap is 1.6 μm (0.77 eV) at ambient temperature.

A good agreement is found between the results obtained with the different setups and detectors in the high energy region of the spectrum. The shape of the signal, in particular the slope of the high energy tail of the signal, are very similar at comparable laser intensities. This means that the estimation of the excitation intensity is fairly good, so the carrier temperature obtained with the different setups can be compared. In the low energy region, setup B gives a lower signal, because of a lower detector sensitivity when approaching the limit of the detection range.

3.3.4 Excitation power density

It was pointed out that the precise determination of the excitation power density was a weak spot of the continuous wave photoluminescence technique. The

thermalization rate is determined from the relation between the power absorbed by the material and the steady state carrier temperature. For that reason, the absorbed power density is a key parameter to have a quantitative determination of the thermalization properties of a sample.

The laser power incident on the sample surface was measured for each photoluminescence measurement, with a powermeter in the focal plane of the setup. The laser spot size was determined using a camera imaging the sample (figure 3.11(a)). The area of the spot was measured by taking the surface of the sample that receives an excitation higher than half of the maximal intensity. This image was scaled using an image of a reference grating (figure 3.11(b)). The spot sizes and power densities in both configurations (A and B) are given in table 3.3.

Knowing the incident power, the absorbed power is then calculated from the absorption coefficient of the material, using a multilayer model described in appendix B. The propagation of a monochromatic plane wave in a stack of flat parallel layers is computed, knowing the absorption coefficient and refractive index in each layer (see for instance reference [46]). The data for absorption coefficient and refractive index were found in [47] and in [48]. It allows to determine the fraction of the incident power that is reflected, transmitted and absorbed as a function of the incident angle and wavelength. An example of the result obtained with a 750 nm laser incident on sample V725 is presented in figure B.1, showing the transmitted (a), reflected (b) and absorbed (c) fraction of an incident plane wave as a function of the incident angle, for different polarization: s, p, and unpolarized.

The angle dependant absorbed power is then integrated over the incident angle to determine the absorbed power when a laser is focused on the sample with a given numerical aperture (or solid angle). A 40% absorption is obtained in that case, roughly independent of the numerical aperture. The same method was used with the other samples.

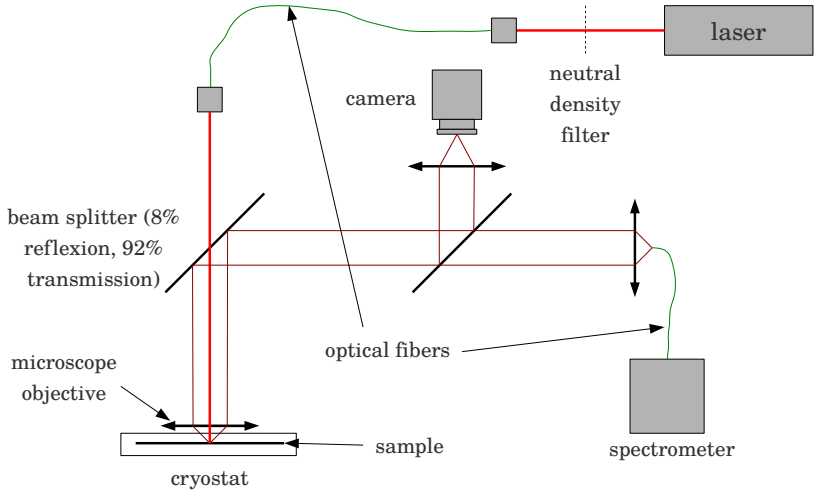

(a) High power density

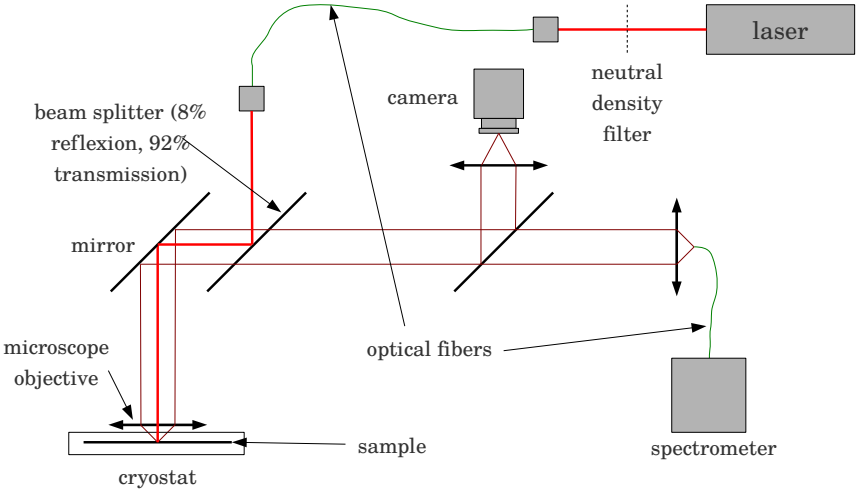

(b) Low power density

Figure 3.9: Schematic of the experimental setup B, in high power density conditions (a) and low power density conditions (b). The excitation laser is coupled in a multimode optical fiber, and collimated towards a microscope objective, after being transmitted (a) or reflected (b) by a beam splitter. It is then focused on the sample that lays in the cryostat chamber. The photoluminescence signal is then collected by the same objective and reflected (a) or transmitted (b) by the beam splitter. The signal is finally coupled to another optical fiber and sent to a spectrometer. A camera can be placed in the optical path to image the sample.

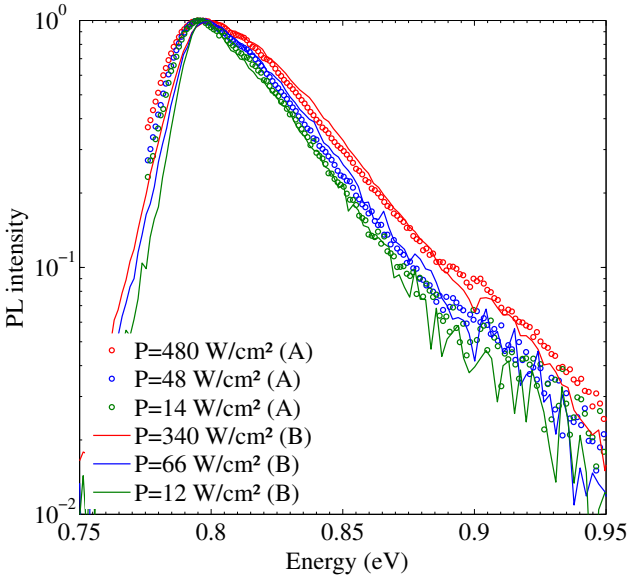

Figure 3.10: PL spectra obtained with a reference InGaAs QW sample on setup A (empty circles) and B (solid lines) at different excitation intensities. The spectra are normalized at the peak intensity. A good agreement is found in the high energy region between the two setups at comparable intensity. A lower signal is observed at low energies with setup B, because of a lower detector sensitivity in this region.

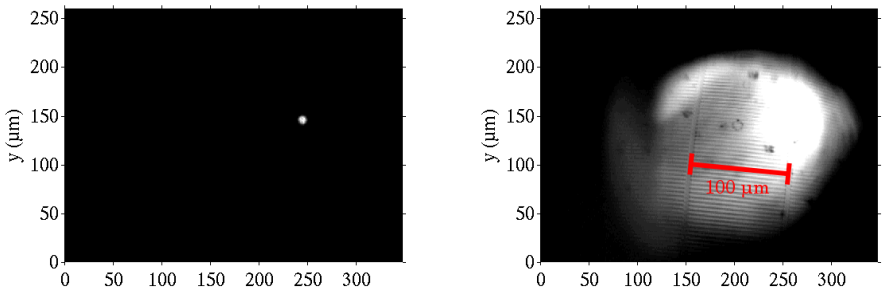

(a) (b)

Figure 3.11: Image of the laser spot (a) compared to a reference grating (b) with a set of vertical lines having a period of 100 μm (red). The spot is found to have a diameter of 10 μm.

3.4 Experimental results: temperature determination and thermalization rate measurement

The results of photoluminescence experiments and the information that are extracted from them are presented in this section. The methodology for extracting temperature and thermalization rates is presented. The impact of sample structure and composition are investigated and discussed.

3.4.1 Photoluminescence spectra analysis

Figure 3.12 is the photoluminescence spectra obtained on sample V725 at 80 K with setup A, for excitation intensity ranging from 0.7 to 700 W/cm^2. Two peaks are visible that, according to their energy position, correspond to the fundamental recombination in the wells for the lower energy peak, and from the GaSb bulk substrate for the higher energy peaks. The different possible radiative transitions are described in figure 3.13. Intersubband transitions ((5) and (6)) are in general non radiative and are not detected here. Relative intensity of transitions (1), (2), (3) and (4) are given by the Fermi-Dirac occupation factor that decreases exponentially with energy.

	Temperature	0 K	80 K	300 K
Band gaps (eV)	well	0.66	0.65	0.58
	barrier	1.12	1.10	1.03
	cladding	2.18	2.17	2.10
	e1hh1 (eV)	0.72	0.70	0.64

Table 3.4: Band gaps of the well, barrier and cladding in the V725 sample at 0 K, 80 K, and 300 K. The fundamental transition e1hh1 in the well is also reported here.

The expected band gaps of the different materials (well, barrier, cladding) are determined at low temperature using the method and data proposed in appendix A. The fundamental transition in the well e1hh1 and the valence and conduction band offsets are proposed in table 3.4 at 0 K, 80 K and ambient temperature. The expected emission energy can be compared to the position of the photoluminescence signal. Radiative recombination in the well are expected at 0.7 eV. Recombination from higher energy level in the well occur at 0.86 eV. The signal from the barrier

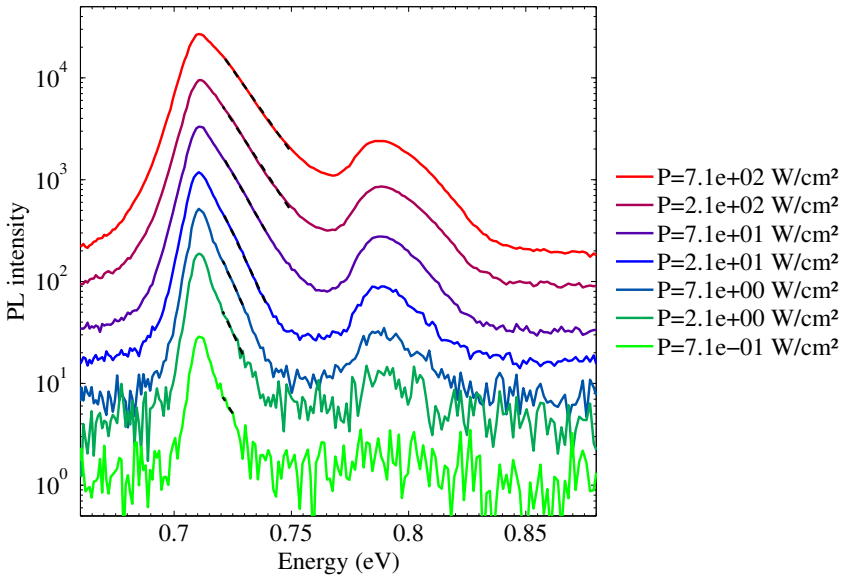

Figure 3.12: Photoluminescence spectra of sample V725 at 80 K at various excitaion intensities from 0.7 to 700 W/cm^2. Two peaks are visible, attributed to radiative transitions in the wells and in the GaSb substrate or capping layer.

should be measured at 1.1 eV and signal from the GaSb substrate or capping layer can also be detected at 0.8 eV.

In figure 3.12, the main peak is measured at 0.7 eV which is in good agreement with the predicted value for e1hh1 transition. A second smaller peak is visible at around 0.8 eV that would come from GaSb. It can come from the thin GaSb capping layer at the surface, that is necessary to passivate the Al-rich cladding layer. It can also come from the GaSb substrate. However, the laser is absorbed in the well region so only a small part of the incident laser reaches the substrate, and the luminescence from the substrate is partially reabsorbed in the well region, so the emission from the substrate should be small. No signal from the barrier or higher levels in the well has been detected.

It is noticeable here that the photoluminescence peak is broadening with an increase of the incident power. This is commonly related to an increasing carrier temperature. A local heating of the material due to the laser excitation could also explain such broadening. However, the peak of luminescence is not shifted with varying excitation power. A heating of the material would lead to a reduction of

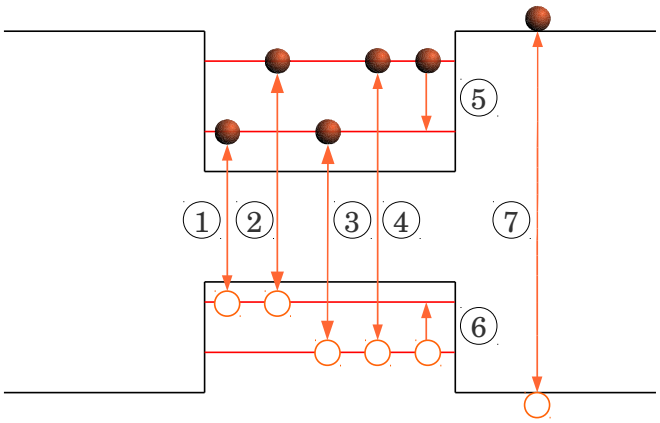

Figure 3.13: Possible radiative transitions in a quantum well structure: (1) fundamental transition from the ground electronic state e1 to the ground heavy hole state hh1 in the well; (2), (3) and (4): higher energy transitions involving excited electronic and/or hole states; (5) and (6) inter subband transitions without recombination; (7) band to band recombination in the barrier.

the band gap, and the peak would be expected to shift towards lower energies.

Considering equation A.1, the variation of the band gap with the temperature is:

$$\frac{dE_g}{dT} = -\alpha T \frac{T+2\beta}{(T+\beta)^2} \tag{3.6}$$

α being of the order of 10^{-4} eV/K and β of the order of 100 K, a typical value is obtained at 80 K: $\frac{dE_g}{dT} \approx 10^{-4}$ eV/K. The temperature increase that is observed here associated with the peak broadening reaches a few hundreds of Kelvin (see below for temperature determination), which would imply a shift of the band gap of the order of 10 meV, which is not observed on figure 3.12. The material heating can then be eliminated as the cause of the peak broadening, and an out of equilibrium carrier population can be considered.

It was said (3.1.1) that the high energy part of the PL signal could be used to determine the temperature. It is simply given by the slope of the curve in log scale: slope $= 1/\mathrm{k}T_H$. This method for carrier temperature extraction is valid under some conditions:

- the absorptivity in the energy range where the slope is determined varies slowly compared to the exponential decay of the carrier occupation factor
- the condition $(E-\Delta\mu)/\mathrm{k}T_h \gg 1$ is verified in that energy range, where $\Delta\mu$

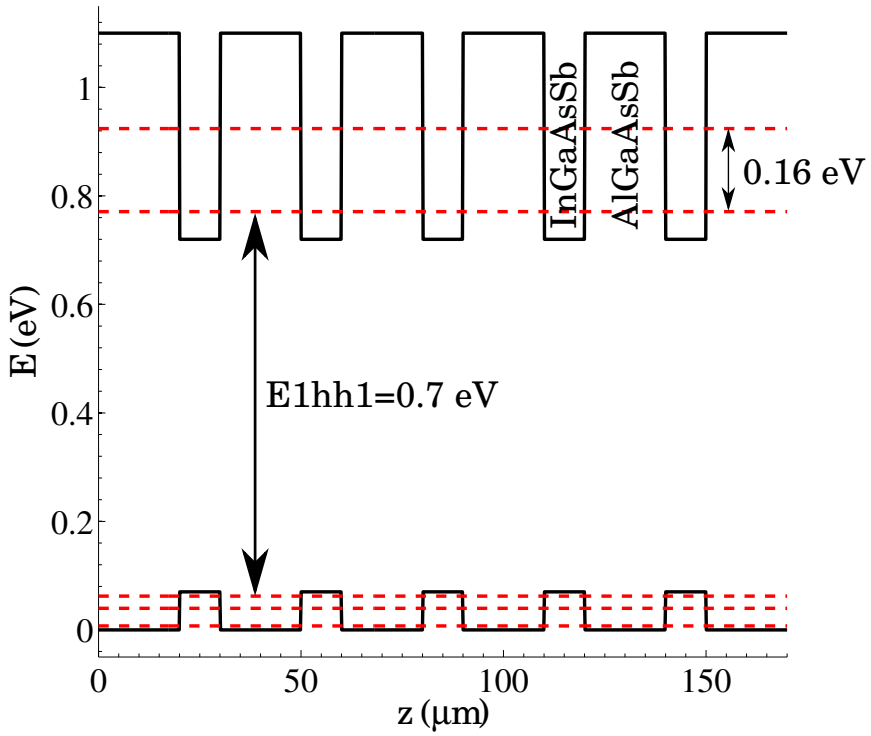

Figure 3.14: Structure of the V725 sample in the quantum well region and position of the electron and hole confined states at 80 K. Two electron and three hole subbands (in red dashed line) are visible. The fundamental transition e1hh1 has an energy of 0.709 eV. The first excited electronic state is 0.16 eV higher than the ground state.

is the quasi-Fermi level splitting.

The first condition is verified in quantum well material, because of a flat density of states, as long as only one energy level is involved, which is the case here with a first excited electronic state that is high enough and should not be populated at reasonable electronic temperature (0.16 eV corresponds to a temperature of 1800 K). One can consider that only the ground electronic state is populated.

The second condition may not be verified in high injection conditions. However, the change in the absorptivity due to quasi Fermi levels coming close to the band edges should only be noticeable in the vicinity of the band gap, and becomes negligible at energies greater than the band gap by about 100 meV.

The method is then to consider an energy range that is high enough to eliminate those effects, and to determine the slope in that region. The error made in the slope determination is estimated from the uncertainty on the luminescence signal. The amplitude of noise is measured, which results in an uncertainty on the position of the points that are used to determine the slope. An uncertainty ΔS is obtained on the slope, which is translated into an uncertainty on the temperature: $\Delta T_H = \mathrm{k}T_H^2 \Delta S$.

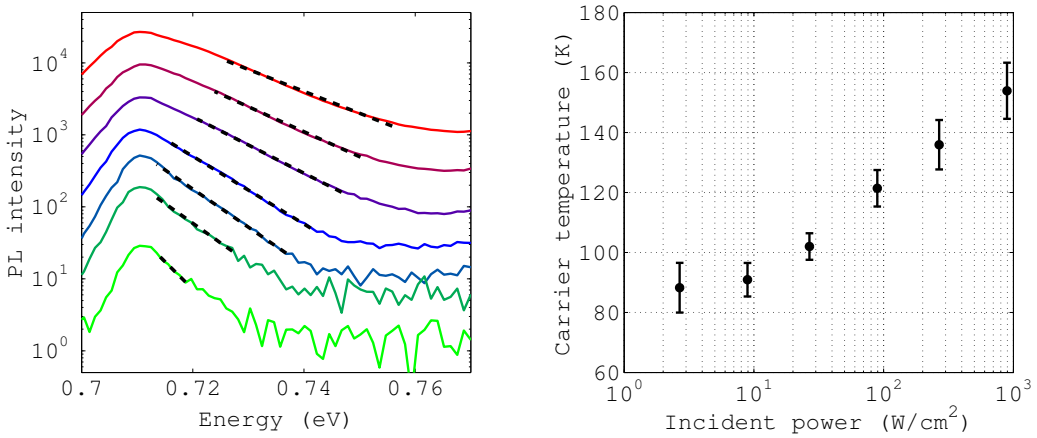

(a) (b)

Figure 3.15: Exponential fit (a) and the deduced carrier temperature vs incident power density (b) from incident power dependent CWPL experiments on sample V725 at 80K.

The results obtained from figure 3.12 are presented in figure 3.15. The carrier temperature is plotted as a function of the excitation power density. At low power density ($P < 10$ W/cm^2, equivalent to 100 suns), the carrier temperature is that of the lattice, indicating a thermalized electron-hole population. When the power density exceeds 10 W/cm^2, the temperature increases progressively to reach close to 160 K at 1000 W/cm^2, or 10000 suns.

3.4.2 Qualitative study of carrier thermalization

Different parameters and their influence on the thermalization properties are investigated next:

– the role of the cladding layers

– the importance of lattice matching
– the effect of quantum confinement of carriers.

Thermalization rates are obtained and compared. Also, experiments are conducted at different lattice temperature, and the effect of lattice temperature on the thermalization of carriers is studied.

Role of claddings for carrier confinement

Samples V809 and V812 have the same structure (see 3.2), the V812 having in addition two AlSb cladding layers sandwiching the absorbing layers. These high band gap cladding layers act as electron and hole barriers, preventing them from being scattered outside of the quantum wells region towards the surface. Two effects can be expected: a reduction of the heat flow outside of the wells, as carriers are insulated from the cold distribution in the substrate, and higher carrier density which should favours the establishment of a hot carrier regime.

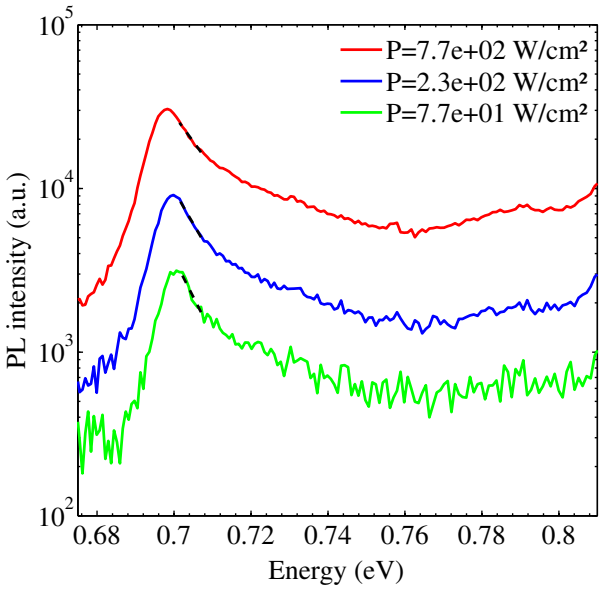

Figure 3.16: Photoluminescence spectra of sample V809 at variable incident power. No change in the spectra shape is visible.

The PL spectra of these two samples measured in the same conditions of lattice temperature (80 K) and excitation intensity are presented in figures 3.16 and 3.17. Several differences are noticeable.

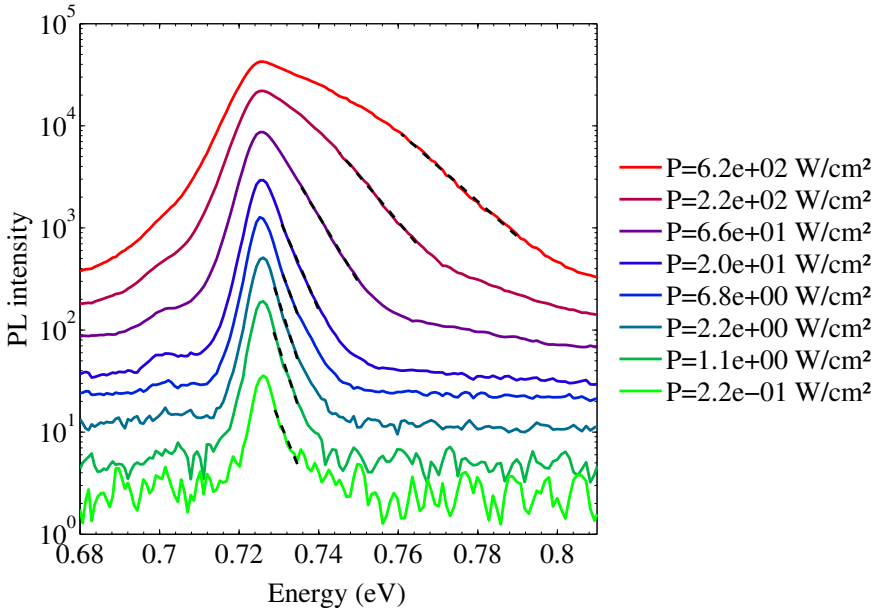

Figure 3.17: Photoluminescence spectra of sample V812 at variable incident power. The high energy tails of the spectra are fitted by an exponential law (black dashed line). A decrease of the slope is observed with increased incident power, indicating a heating of carriers.

First, the photoluminescence intensity of sample V809 is much weaker than for sample V812 at the same excitation power. This must come from a higher non radiative recombination rate without the AlSb layer. In V812 sample, the photogenerated carriers are confined in the quantum well region, where they recombine, mainly radiatively. On the contrary, the carriers generated in V809 are scattered towards the surface where they can recombine through surface state, providing additional recombination pathways. If this process is faster than the radiative recombination in the well region, it can explain the strong reduction of the photoluminescence intensity.

Secondly, the optical band gap is shifted with a photoluminescence peak at 0.7 eV compared to the case of sample V812. The well ($Ga_{0.8}In_{0.2}Sb$) band gap at low temperature can be determined as mentioned above, and should be $E_{g,Ga_{0.8}In_{0.2}Sb}(T = 50K) = 0.625$ eV. This is the bandgap of the bulk material, which is increased in the case of quantum wells because of confinement. Knowing the material electron and hole effective masses and the well and barrier thick-

nesses, the position of the lowest electronic state in the conduction band and of the highest hole state in the valence band can be determined, and the expected optical band gap is $E_{e_1hh_1}(T = 50K) = 0.67$ eV. This value is much smaller than the band gap observed on PL spectra of sample V812.

However, this does not account for strain effect on the band gap. The InGaSb layers on a GaSb substrate have a compressive strain that increases the band gap. The band gap shift can be estimated, using a deformation potential constant D that can be found in [49]. The band gap shift is then: $\Delta E_g = D \times \Delta a/a$, where a is the lattice parameter and Δa is the lattice mismatch. The lattice parameter and deformation potential constant of the ternary alloy InGaSb is determined by a linear interpolation of the values for GaSb and InSb. The band gap shift is then obtained $\Delta E_g = 0.098$ eV at 50 K. The position of the energy levels in the well can then be recalculated, and we find $E_{e_1hh_1}(T = 50K) = 0.74$ eV. This value is higher than the observed band gap, but much closer than the previous value of 0.67 eV. The discrepancy can come from an overestimation of the deformation in the layer, because of a lower indium content than expected in the layer, or partial relaxation of the strain by dislocations for instance. One can still conclude that the PL signal from sample V812 at 0.72 eV does correspond to recombination in the well region. Sample V809 having the same structure (as can be seen on XRD measurement, both samples have very similar well composition and strain, see figure 3.6), it should exhibit luminescence at the same energy. The shift of the PL peak thus indicates that the luminescence comes from another mechanism.

A weak peak is visible on the V812 spectra below the bandgap that is at the same energy as the signal from sample V809. This seems to indicate that the band gap luminescence is in fact absent in the V809 spectra, and that the signal comes from other recombination process (through defect levels for instance). It is impossible to conclude with certainty about the nature of this peak. It would require further investigation about the position of defects in the absorber and at interfaces. Anyway, the absence of the main photoluminescence peak in the V809 spectra makes the determination of a carrier temperature and the investigation of the thermalization properties impossible.

Cladding layers thus seem necessary, for practical and methodological reasons (weak and unusable signal), and for physical reasons to favour a hot carrier regime: the confinement of carriers enables higher carrier concentration, and cladding layers prevent the heat from flowing outside of the well region. The samples without cladding layers will be abandonned in the following analysis.

Lattice matched vs strained

The comparison of a lattice-matched sample (V725) and a strained sample (V812) can provide information on the impact of strain on the thermalization properties.

It is expected that strain should accelerate the thermalization of carriers, since it creates defects levels in the band gap that provide additional non radiative recombination pathways. It is also a technological constraint as it does not allow to grow thicker layers with good crystalline quality, whereas it was possible to grow a 50 nm thick absorbing layer with the lattice-matched material (see section 3.4.2).

However, using only lattice-matched materials adds another constraint in the composition of the absorbing alloy. For that reason, using strained samples may be beneficial if the thermalization properties are not degraded.

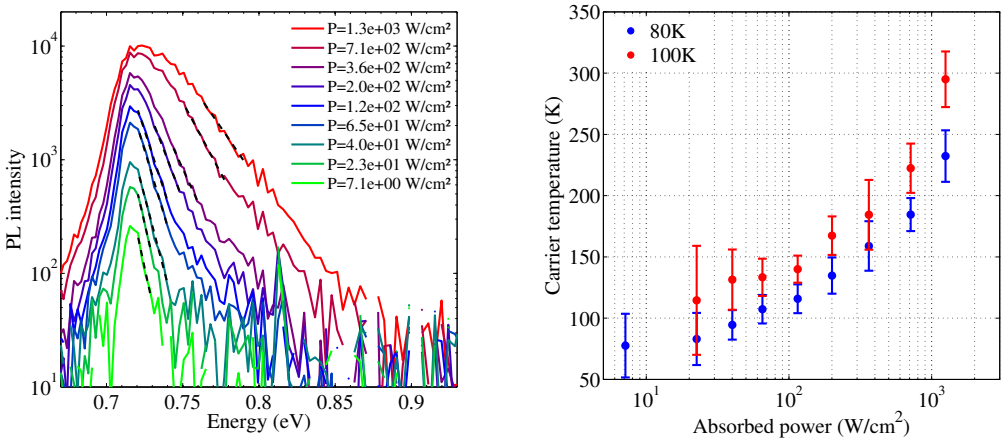

(a) (b)

Figure 3.18: PL spectra of sample V812 at different incident power densities at 80 K (a) and carrier temperature (b) as a function of the absorbed power density deduced from the PL data. At low power density, the carrier temperature is that of the lattice. It increases with increased absorbed power to reach almost 200 K above the lattice temperature.

Figures 3.18(a) and 3.19(a) show the PL spectra obtained with sample V812 and V725 respectively at 80 K. In both cases, a broadening of the PL peak is observed with the increase of incident power, while the position of the peak is unchanged. The peak broadening is strongly asymmetrical and is mainly visible

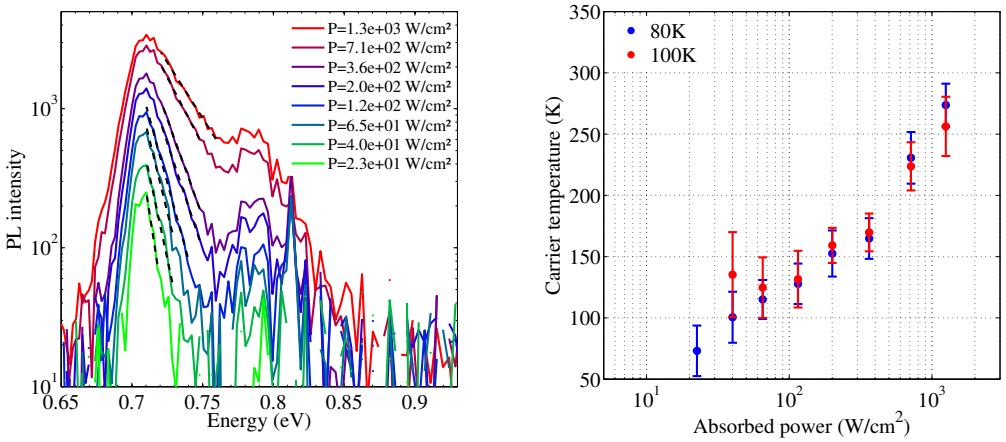

(a) (b)

Figure 3.19: PL spectra of sample V725 at different incident power densities at 80 K (a) and carrier temperature (b) as a function of the absorbed power density deduced from the PL data. At low power density, the carrier temperature is that of the lattice. It increases with increased absorbed power to reach almost 200 K above the lattice temperature.

on the high energy side of the spectrum.

The carrier temperatures that are extracted from the PL signal for samples V725 and V812 are reported in figure 3.19(b) and 3.18(b) as a function of the incident power, and for two different lattice temperatures: 80 K and 100 K. It is first noticeable that, at low excitation intensity, the carrier temperature that is found is close to the lattice temperature in all cases. This validates the method for the temperature determination. With the raise of the excitation power, the carrier temperature is increased up to around 300 K for both samples, at excitation intensities close to 1 kW/cm^2, which corresponds to approximatively 10000 suns.

Both samples give comparable results, and a quantitative determination of the thermalization time is necessary to conclude (see section 3.4.3). It seems that no spectacular difference is visible in the thermalization properties, so technological criteria are likely to be predominant in the choice between strained and strain-free samples. In that case, the possiblity to grow thicker layers with lattice matched materials should be crucial.

Influence of quantum confinement

It is expected (as shown in chapter 4, it is also stated in various papers [19, 33, 37]) that the carrier energy loss rate can be reduced in quantum well structures compared to bulk. The first samples we studied were therefore quantum structures to favour the establishment of a hot carrier regime. However, an experimental comparison with the bulk-like material is necessary.

A 50 nm InGaAsSb layer was grown, embedded in two 60 nm AlGaAsSb, with the same composition as in sample V725, and sandwiched with the same cladding layers. A structure with the same well thickness, but without quantization, is then obtained (sample V1231). Its band gap is reduced compared to that of V725, and equal to 2.1 μm at ambient temperature. The comparison between V725 and V1231 can help to understand the role of quantization in the thermalization properties.

The composition of sample V812 or V809 did not allow to grow a thick layer as it is not lattice-matched with the bulk GaSb.

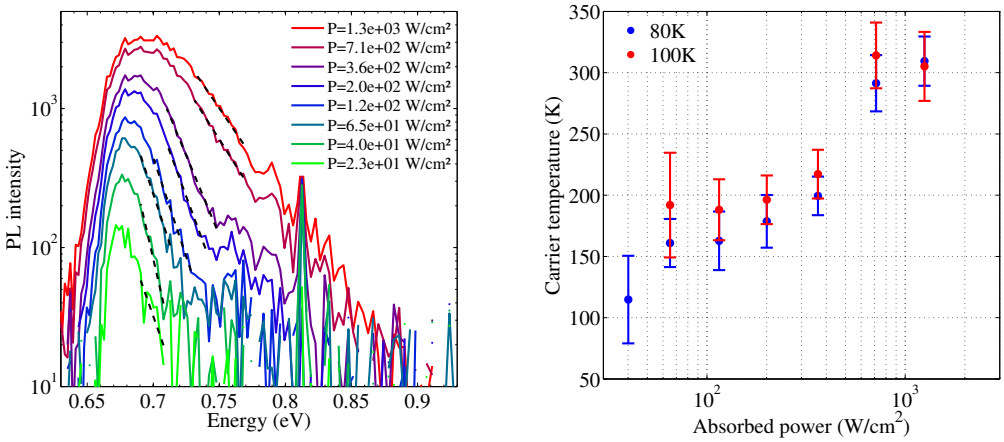

(a) (b)

Figure 3.20: PL spectra of sample V1231 at different incident power densities at 80 K (a) and carrier temperature (b) as a function of the absorbed power density deduced from the PL data.

The photoluminescence spectra obtained with V1231 on setup B are presented in figure 3.20(a), and the spectra obtained with sample V725 at 80 K in the same conditions are presented in figure 3.19(a). The carrier temperatures that are

extracted from those data are presented in figures 3.19(b) and 3.20(b). In both cases, a carrier heating occurs, which is slightly more pronounced in the case of V725. The carrier temperature reaches about 280 K for V725, and less than 200 K for V1231. It seems that the thermalization is faster in the bulk material, but still comparable. No drastic difference is observable between V725 and V1231.

However, the determination of the carrier temperature may be affected by the absorptivity in the bulk material. In the PL curve fitting, it is assumed that the absorptivity is constant in the energy range that is considered. It is very likely to be verified in quantum well samples where the electronic density of state is flat. In bulk sample, this density of state can be modeled by a $\sqrt{E - E_G}$ law. With an increasing absorptivity with increasing energy, the slope can be underestimated, and the carrier temperature overestimated. An experimental determination of the material absorptivity would then be necessary to avoid this problem. A slowly varying absorptivity will still be assumed. Such assumption is supported by the absorption coefficient of the GaSb in the energy range considered here, represented in figure 3.21 at 300, 77, and 4 K [48]. The well composition is not far from GaSb, and a rather similar shape is expected.

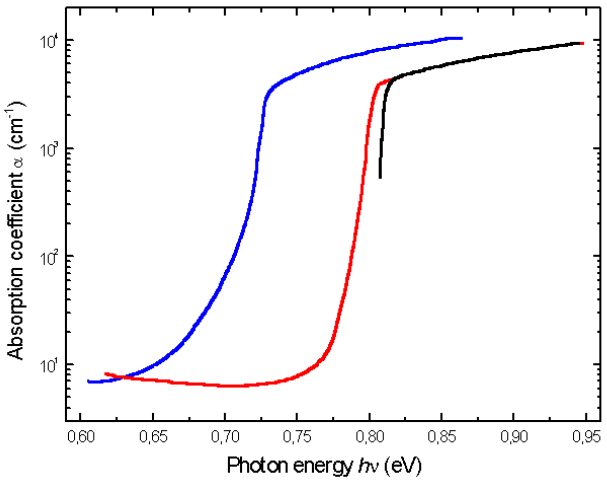

Figure 3.21: Absorption coefficient of a p-type bulk gallium antimonide at 300 (blue), 77 (red) and 4 K (black). A slowly varying absorption coefficient is observed above the absorption edge. From [48]

3.4.3 Carrier thermalization time and thermalization rate

The thermalization properties of a sample can be determined from the carrier temperature - incident power relationship. Since there is no electrical power extracted, the absorbed power can only be lost as heat towards the lattice or by radiative recombinations (non radiative recombinations involving phonon emission, they contribute to the heat transfer to the lattice). In other words, carriers loose their energy by interaction with phonons or photons. The power lost by thermalization can then be expressed as the difference between the absorbed power and the radiatively emitted power.

The determination of absorbed power was detailed in 3.3.4. An absolute measurement of the emitted power was not possible, but assuming a dominant radiative recombination, the power lost by recombination can be estimated from the photoluminescence data. Photons are absorbed with energy $E_{abs} = E_{laser}$, and reemitted with an average energy E_{em} that can be determined from the PL spectra:

$$E_{em} = \frac{\int_0^\infty E \times I_{PL}(E)dE}{\int_0^\infty I_{PL}(E)dE} \tag{3.7}$$

where $I_{PL}(E)$ is the photoluminescence intensity as a function of the photon energy E. If recombinations are radiatively dominated, the number of absorbed photons equals the number of emitted photon, and the radiatively emitted power is given by:

$$P_{em} = \frac{E_{em}}{E_{abs}} P_{abs} \tag{3.8}$$

In the case of non radiatively dominated recombination, the radiatively emitted power can be expressed similarly:

$$P_{em} = \eta \frac{E_{em}}{E_{abs}} P_{abs} \tag{3.9}$$

with η being the radiative yield, that is to say the fraction of total recombination that are radiative.

Finally, the power transferred from carriers to the lattice per unit volume is:

$$P_{Th} = \frac{P_{abs} - P_{em}}{t} = \frac{1}{t}\left(1 - \eta \frac{E_{em}}{E_{abs}}\right) P_{abs} \tag{3.10}$$

where t is the absorbing material thickness.

This power transfer comes from interaction with phonons. In polar semicondutors, at temperature above a threshold around 40 K, this interaction is dominated

by a strong coupling with the zone center LO phonon modes, so it will be considered that only these modes contribute to the carrier energy loss. The carrier energy loss rate to LO phonons can be written, in the case of small non equilibrium [3]:

$$P_{Th} = \frac{n\hbar\omega_{LO}}{\tau}\exp\left(-\frac{\hbar\omega_{LO}}{\mathrm{k}T_H}\right) \tag{3.11}$$

P_{Th} can be obtained from equation 3.10, T_H is determined from photoluminescence data, n is the carrier density, τ is an average phonon emission time, which is in general a function of the carrier temperature, the lattice temperature and the carrier density.

This model for the carrier energy loss rate is confirmed by plotting $1/T_H$ as a function of the incident power in log scale. A linear relation is observed with a slope that is related to the LO phonon energy and is $-\mathrm{k_B}/\hbar\omega_{LO}$ (see figure 3.22). The phonon energy that is considered here is that of bulk GaSb, which gives a good agreement with the experimental data. At low power density, the data deviate from the linear relation. This can be due to a different regime where LO phonon emission is not the only energy loss mechanism. It can also come from a less accurate determination of the carrier temperature at low power density.

Such a model, however, only applies as long as the limiting process is phonon emission. When a phonon bottleneck occurs, the electron-LO phonon interaction can be considered instantaneous, and the limiting process is now the decay of the out of equilibrium LO phonons into acoustic phonons. Thus, in our case, another model needs to be used that is given in [43]. In that case, one considers an out of equilibrium zone center LO phonon population that equilibrates with electrons, and decays by interaction with the other phonon modes at the lattice temperature. The rate at which electrons loose their energy is then limited by the rate at which the excited phonon modes decay into other phonon modes. The power lost by carriers is then given by the LO phonon decay rate $1/\tau$, mutliplied by the LO phonon energy and by the number of phonons involved, which is the number of phonon modes coupled to electrons, times their occupation number in excess of the equilibrium occupation number.

$$P_{Th} = \frac{\hbar\omega_{LO}}{\tau}\frac{n_q}{2}\left(N_q(T_H) - N_q(T)\right) \tag{3.12}$$

where n_q is the number of phonon modes that are in thermal disequilibrium, $N_q(T_H)$ and $N_q(T)$ are the LO phonon occupation numbers at the hot temperature and at the lattice temperature respectively. The rate depends here on the density of out of equilibrium phonons, and not on the carrier density, because the cooling is limited by the decay of LO phonons.

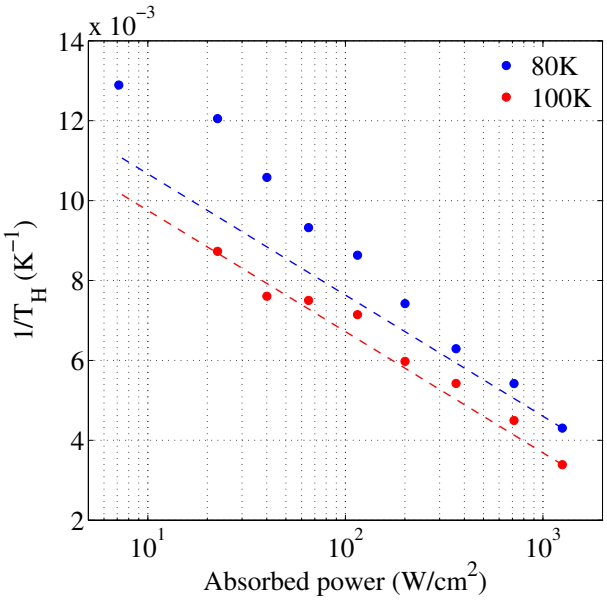

Figure 3.22: Inverse of the carrier temperature as a function of the absorbed power density in log scale in the case of sample V812. A linear relation is observed, with a slope $-\mathrm{k_B}/\hbar\omega_{LO}$, with $\hbar\omega_{LO}$ being the LO phonon energy of bulk GaSb (represented by dashed straight line) at two different lattice temperature: 80 K (blue) and 100 K (blue). The vertical shift between data at different temperatures comes from a change in the phonon lifetime.

The above expression applies in the most general case for one phonon mode $\vec{q}$ with energy $\hbar\omega_{LO}(\vec{q})$. The LO phonon distribution function will be approximated here by a flat distribution with a constant energy $\hbar\omega_{LO}$. Only a small region of the Brillouin zone is involved in the out of equilibrium phonon population [36]: the norm of the wave vector of coupled phonon modes is inferior to a tenth of the Brillouin zone radius. The approximation of constant LO phonon energy is thus reasonable. $N_q(T)$ is given by a Bose-Einstein distribution function at energy $E_q = \hbar\omega_{LO}$ and at temperature T:

$$N_q(T) = \left(\exp\left(\frac{\hbar\omega_{LO}}{\mathrm{k}T}\right) - 1\right)^{-1} \tag{3.13}$$

At low temperature (up to ~ 200 K), the phonon distribution can be approximated by a Boltzman distribution, and the expression above can be simplified: $N_q(T) = \exp(-\hbar\omega_{LO}/\mathrm{k_B}T)$. The heating of carriers being associated with an out

of equilibrium LO phonon distribution, its occupation number becomes large compared to the equilibrium value: $N_q(T_H) \gg N_q(T)$. Equation 3.12 can then be simplified:

$$P_{Th} = \hbar\omega_{LO}\frac{n_q}{2\tau}\exp\left(-\frac{\hbar\omega_{LO}}{\mathrm{k_B}T_H}\right) \tag{3.14}$$

An expression similar to 3.11 is obtained, wich explains that $1/T_H$ follows a linear relation with the logarithm of the absorbed power density (figure 3.22).

The number of coupled phonon modes n_q can be estimated [50]. For a given phonon energy $\hbar\omega_{LO}$, the density of electronic states that satisfy both energy and momentum conservation conditions (see figure 3.23) is determined as a function of the phonon wave vector. Let us consider an initial state for an electron given by its momentum k_1 and its energy E_1, that emits a phonon with wave vector q and energy $\hbar\omega_{LO}$, and ends up in the final state given by momentum k_2 and energy E_2. The conservation of momentum and energy implies that $k_1 - k_2 = q$ and $E_1 - E_2 = \hbar\omega_{LO}$. Considering a parabolic Γ valley only, the energy of the electron is $E_i = \hbar^2 k_i^2/2m^*$, with index i refering to initial or final state. The values of E_1 and E_2 are obtained:

$$\begin{aligned} E_1 &= \frac{\hbar^2}{2m^*}\left(\frac{1}{2}\left(\frac{2m^*\hbar\omega_{LO}}{\hbar^2 q} + q\right)\right)^2 \\ E_2 &= \frac{\hbar^2}{2m^*}\left(\frac{1}{2}\left(\frac{2m^*\hbar\omega_{LO}}{\hbar^2 q} - q\right)\right)^2 \end{aligned} \tag{3.15}$$

The joint density of electronic states $g_e(E_1, E_2)$ is, considering a flat DOS in quantum wells, $m^*/\pi\hbar^2$. The density of phonon states is $g_p(q) = 4\pi q^2$. Finally, the occupation factors for electrons is given by a Fermi-Dirac distribution at energy E_i $f_e(E_i) = 1/(\exp(E_i/\mathrm{k_B}T_H) + 1)$, where T_H is the carrier temperature, and for phonons by a Bose-Einstein distribution $f_q = 1/(\exp(\hbar\omega_{LO}/\mathrm{k_B}T) - 1)$, where T is the temperature of the lattice. The Fröhlich hamiltonian varies as the inverse of the square of the phonon wave vector, so finally, the net phonon emission rate as a function of the phonon wave vector is:

$$W(q) \propto \frac{1}{q^2} g_e(E_1, E_2) g_p(q) \left((1 + f_q) f_e(E_1) f_e(E_2) - f_q f_e(E_2) f_e(E_1)\right) \tag{3.16}$$

This phonon generation function obtained with GaSb at 80 K (lattice temperature) and for different carrier temperatures is plotted in figure 3.24 in arbitrary units. It shows that the phonon modes that are the most strongly coupled with electrons are zone center phonons, in a tenth of the Brillouin zone. The number of phonon modes involved would be given by the number of phonon modes

in the Brillouin zone, modulated by the phonon generation function presented in figure 3.24. Here it will be approximated by the total number of modes inside a sphere with radius q_0, q_0 being the norm of the wave vector for which 90% of the integrated phonon generation function is below this value.

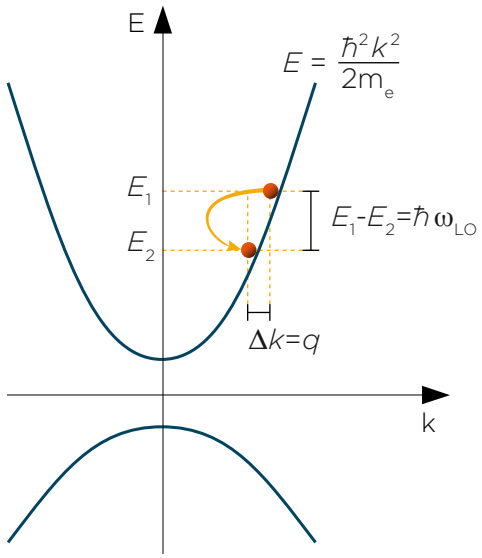

Figure 3.23: Schematic of the electron energy loss process. An electron with energy E_1 relaxes to energy E_2 with emission of a phonon with energy $\hbar\omega_{LO} = E_1 - E_2$. Conservation of momentum implies that the electron momentum variation Δk equals the emitted phonon wave vector q. The conduction band is approximated by a parabolic dispersion relation $E = \frac{\hbar^2 k^2}{2m_e}$, m_e being the electron effective mass.

n_q being determined, the thermalization time can then be expressed as a function of the carrier temperature, in the most general form:

$$\tau = \frac{n_q \hbar\omega_{LO}}{\frac{2}{t}\left(1 - \eta\frac{E_{em}}{E_{abs}}\right) P_{abs}} \left(N_q(T_H) - N_q(T)\right) \tag{3.17}$$

Values close to 5 ps are obtained.

The n_q/τ ratio can be plotted as a function of the carrier temperature, showing a linear relation between n_q/τ and $T_H - T$ (see figure 3.25). With such a linear

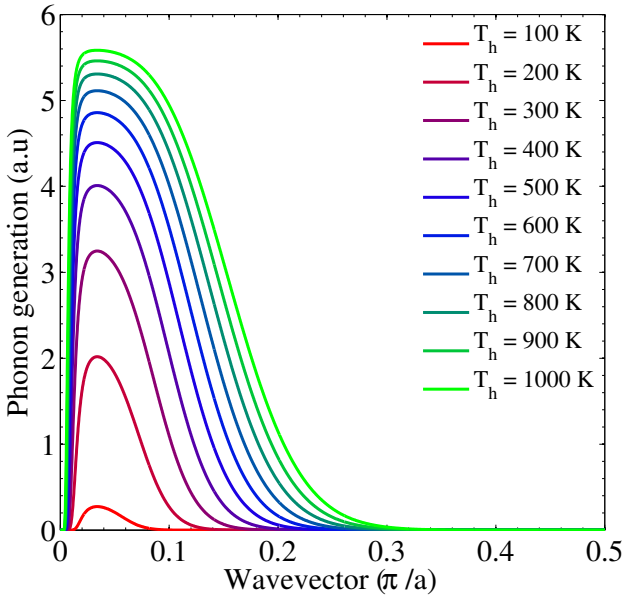

Figure 3.24: Intensity of the phonon generation by carriers in arbitrary units as a function of the norm of the emitted phonon wave vector in GaSb at 80 K, and for different carrier temperatures from 100 K to 1000 K.

relation, the quantity

$$Q = \frac{\hbar\omega_{LO} n_q}{2\tau(T_H - T)} \tag{3.18}$$

is a material constant. It will be called the thermalization coefficient, in $\mathrm{W.K^{-1}.cm^{-2}}$, so that the power lost by carriers to phonons can be expressed:

$$P_{Th} = Q(T_H - T)\exp\left(-\frac{\hbar\omega_{LO}}{\mathrm{k_B} T_H}\right) \tag{3.19}$$

The values of Q obtained with the different samples at different lattice temperatures are listed in table 3.5. It was calculated assuming the non radiative limit (radiatively emitted power is negligible). All these data were obtained using the setup B in high power density configuration. Results from setup A could have been used to investigate the sample behaviour at lower temperatures, but the uncertainty on the incident power density does not allow to determine reliable values of the thermalization coefficient.

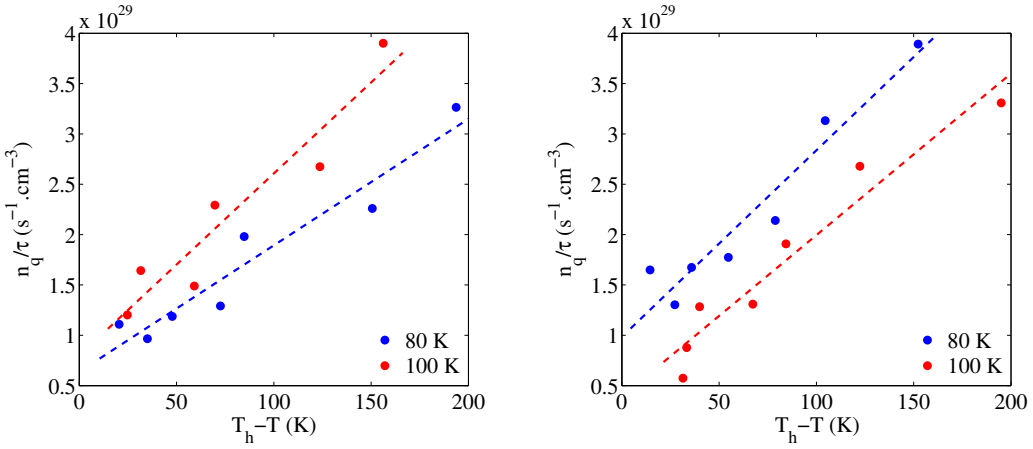

(a) V725 (b) V812

Figure 3.25: The n_q/τ ratio obtained with sample V725 (a) and sample V812 (b) at 80 (blue) and 100 K (red) as a function of the carrier temperature difference with the lattice. Linear relations are visible when the carrier temperature does not exceed 300 K.

sample	80 K	100 K	150 K
V812	72 ± 21	62 ± 23	-
V725	48 ± 14	70 ± 34	47 ± 27
V1231	51 ± 16	56 ± 28	43 ± 24

Table 3.5: Thermalization coefficient Q in $\mathrm{W.K^{-1}.cm^{-2}}$ obtained from continuous photoluminescence experiments on sample V725, V812 and V1231, at different lattice temperatures, and its standard deviation σ_Q.

From the data in table 3.5, one can say that all samples give comparable thermalization properties. No specific trend is observed with the lattice temperature. It has to be noted that no value could be obtained with sample V812 at 150 K, because at this temperature, the signal from the well and the barrier overlap and no carrier temperature could be found. With the other samples, the two peaks are still distinct, even if at high power density, a small overlapping could be responsible for an overestimation of the carrier temperature, and thus to an underestimation of the thermalization coefficient. This could explain why Q is smaller at 150 K

than at 100 or 80 K with sample V725 and V1231.

It also appears that the uncertainty on the estimated thermalization coefficient, represented by its standard deviation, is very large and comparable to the value of Q itself. Several factors can explain this very high uncertainty:

- Detector sensibility: as was said in section 3.3, the detector used did not allow to go to low power density, and the spectra obtained with it are noisy, which results in large uncertainty in the carrier temperature determination. Similar experiments with a nitrogen cooled spectrometer for instance could reduce the uncertainty.
- Stability of the laser source: the power density on the sample was determined once without filters, and then calculated using neutral density filters with a known transmission, assuming a stable power delivered by the laser. An unstable laser source would lead to an error on the incident power density which adds uncertainty in the thermalization coefficient determination. A stabilized laser and/or a signal acquisition with a simultaneous measurement of the laser power would be desirable.
- Number of experimental data: photoluminescence was acquired at few different incident power (between 5 and 8 usable spectra at each lattice temperature), and at few different lattice temperatures (80, 100 and 150 K). Additional measurements could be performed at lower, intermediate, and higher power density (provided a higher detector sensitivity and laser power are possible).

In these conditions, it is difficult to have quantitative information on these samples. However, this study provides an order of magnitude for the thermalization coefficient and validates the model used in chapter 4, with a power lost by thermalization of the form of equation 3.19.

Considering results at 80 K, which are the most reliable, sample V812 seems to exhibit a faster thermalization than the lattice matched samples. No clear difference is visible between quantum wells (V725) and a thick (50 nm) layer (V1231). Quantization does not seem to reduce the thermalization rate. Further work is needed to better understand the phonon dynamics and lifetime in quantum structure, in order to propose an optimized structure, with compositions and thicknesses that are designed to favor the formation of a LO phonon bottleneck.

3.4.4 Influence of the lattice temperature

The thermalization properties were investigated at different lattice temperatures. Below a threshold around 40 K, the carrier energy loss mechanism is different, with no LO phonons involved. Other mechanisms, involving less energetic

acoustic phonons, are dominant at very low temperature. If this process is less efficient than the coupling to LO phonon, resulting in a slower thermalization at low power densities, the generation of a hot phonon population leading to phonon reabsorption compensating phonon emission is not possible.

Above 40 K, the energy loss rate reduction with increased power density can be explained by a phonon bottleneck effect. The LO phonon lifetime depends on the lattice temperature: at higher temperature, the phonon occupation is higher, and the probability for a LO phonon to be scattered though anharmonic interaction is increased. It is thus expected that the carrier energy loss rate will be increased at higher temperature.

One notice in figure 3.22 a down shift of the experimental data of $1/T_H$ between experiments at 80 K and 100 K. From equation 3.11, this can be related to a reduction of the thermalization time τ. In the case of a thermalization limited by LO phonon decay, because of a phonon bottleneck, the thermalization time is expected to be the LO phonon lifetime. The evolution of the phonon lifetime with the lattice temperature was given in [26]:

$$\tau_{LO}(T) = \tau_{LO}(0)\left[1 + 2\left(\exp\frac{\hbar\omega_{LO}}{2k_B T} - 1\right)^{-1}\right]^{-1} \tag{3.20}$$

The ratio of phonon lifetimes at different temperatures can then be calculated:

$$\frac{\tau_{LO}(T_1)}{\tau_{LO}(T_2)} = \frac{1 + 2\left(\exp\frac{\hbar\omega_{LO}}{2k_B T_2} - 1\right)^{-1}}{1 + 2\left(\exp\frac{\hbar\omega_{LO}}{2k_B T_1} - 1\right)^{-1}} \tag{3.21}$$

which only depends on the two temperatures T_1 and T_2.

Finally, the ratio of the thermalization coefficients is simply the inverse of the ratio of the phonon lifetimes:

$$\frac{Q(T_1)}{Q(T_2)} = \frac{\tau_{LO}(T_2)}{\tau_{LO}(T_1)} \tag{3.22}$$

From the thermalization coefficient calculated at 80 K, it is possible to determine a theoretical value at 100 K, 150 K, and even to extrapolate at 300 K. Results are displayed in table 3.6.

Theoretical values are within the experimental uncertainty. At 150 K, the experimental value is always below the theoretical value. This may come from an overestimation of the experimental thermalization coefficient when the lattice temperature is increased because of an increased overlapping between the well and

sample	100 K		150 K		300 K
	exp	theory	exp	theory	
V812	62	75	-	85	116
V725	70	50	47	57	77
V1231	56	53	43	60	82

Table 3.6: Experimental and theoretical values of the thermalization coefficient in $W.K^{-1}.cm^{-2}$ at different temperatures deduced from the 80 K value, for samples V812, V725 ad V1231, and extrapolation at ambient temperature.

substrate signal. A resolution of the two peaks would be necessary to have a better estimation of the carrier temperature, which would require a precise measurement of the material absorptivity at the different lattice temperatures.

It can be noted that the model considered at 80 K, in which the power lost by interaction with the lattice is given by equation 3.19, does not apply at ambient temperature, since the phonon occupation number can not be approximated by a Maxwell-Boltzmann distribution. The extrapolated value of the thermalization coefficient at 300 K will be considered nevertheless, with a Bose-Einstein distribution instead of the Maxwell-Boltzmann distribution in equation 3.19.

When this model is applied to time-resolved photoluminescence results on GaAs multi quantum wells proposed in [19], a thermalization coefficient of about 10 $W.K^{-1}.cm^{-2}$ is found. Considering that the steady state value is about ten times the transient state value, a typical value of 100 $W.K^{-1}.cm^{-2}$ is obtained for GaAs at ambient temperature in continuous excitation conditions. The GaSb-based samples investigated here have therefore a thermalization rate that is comparable, and even lower for V725 and V1231, to that of GaAs samples.

3.5 Conclusion

The thermalization properties of test samples were investigated using continuous wave photoluminescence rather than time-resolved photoluminescence, in order to obtain relevant information for a steady-state operating device.

The first noticeable result is the importance of claddings for the establishment of a hot carrier distribution. They are necessary for photoluminescence experiments, but also in the operating device architecture to prevent the scattering of non equilibrium carriers outside of the absorber.

A second important finding is that lattice-matched samples may provide slower

carrier thermalization that strained samples. The design and synthesis of lattice-matched structure is also simplified, giving the possibility to grow thick layers. For these reasons, lattice-matched materials should be preferred.

Finally, no clear effect of the material quantization on the thermalization properties is visible. Quantized and non quantized structures with the same material thickness give very similar thermalization rates. This contradicts previous work on GaAs quantum well structures. Here, it seems that without specific optimization of the structure regarding the phonon dynamics, quantum structures do not provide slower thermalization.

The thermalization rate that are observed on GaSb-based samples are comparable, and even slightly lower, than what is found in previous work on GaAs. A thermalization coefficient of $Q = 80$ W/K/cm^2 will be considered at ambient temperature in the next chapter.

Bibliography

[1] J. Shah and R.C.C Leite. Radiative recombination from photoexcited hot carriers in GaAs. *Phys. Rev. Lett.*, 22:1304, 1969.

[2] P. Würfel. The chemical potential of radiation. *J. Phys. C: Solid State Phys.*, 15:3967–3985, 1982.

[3] S.A. Lyon. Spectroscopy of hot carriers in semiconductors. *Journal of Luminescence*, 35:121, 1986.

[4] J. Shah. Photoexcited hot carriers: from cw to fs in 20 years. *Solid State Electronics*, 32:1051, 1989.

[5] R. Ulbrich. Low density photoexcitation phenomena in semiconductors: Aspects of theory and experiment. *Solid State Electronics*, 21:51, 1978.

[6] DN. Mirlin, IJ. Karlik, LP. Nikitin, II. Reshina, and VF. Sapega. Hot electron photoluminescence in GaAs crystals. *Solid State Communications*, 37(9):757–760, 1981.

[7] G. Fasol, W. Hackenberg, H.P. Hughes, K. Ploog, E. Bauser, and H. Kano. Continuous-wave spectroscopy of femtosecond carrier scattering in GaAs. *Phys. Rev. B*, 41:1461, 1990.

[8] A. Othonos. Probing ultrafast carrier and phonon dynamics in semiconductors. *Applied Physics Reviews*, 83:1789, 1998.

[9] R. Ulbrich. Energy relaxation of photoexcited hot electrons in GaAs. *Phys. Rev. B*, 8:5719, 1973.

[10] J. Shah, RF Leheny, and W. Wiegmann. Low-temperature absorption spectrum in GaAs in the presence of optical pumping. *Physical Review B*, 16(4):1577–1580, 1977.

[11] C.V. Shank, R.L. Fork, R.F. Leheny, and J. Shah. Dynamics of photoexcited GaAs band-edge absorption with subpicosecond resolution. *Phys. Rev. Lett.*, 42:112, 1979.

[12] D. Von Der Linde and R. Lambrich. Direct measurement of hot-electron relaxation by picosecond spectroscopy. *Phys. Rev. Lett.*, 42:1090, 1979.

[13] S. Tanaka, H. Kobayashi, H. Saito, and S. Shionoya. Luminescence of high density electron-hole plasma in GaAs. *J. Phys. Soc. Japan*, 49:1051, 1980.

[14] K. Kash and J. Shah. Carrier energy relaxation in $In_{0.53}Ga_{0.47}As$ determined from picosecond luminescence studies. *Applied Physics letters*, 45(4):401–403, 1984.

[15] J. Shah, TC Damen, B. Deveaud, and D. Block. Subpicosecond luminescence spectroscopy using sum frequency generation. *Applied Physics Letters*, 50(19):1307–1309, 1987.

[16] J. Shah, B. Deveaud, TC Damen, WT Tsang, AC Gossard, and P. Lugli. Determination of intervalley scattering rates in GaAs by subpicosecond luminescence spectroscopy. *Physical review letters*, 59(19):2222–2225, 1987.

[17] T. Elsaesser, J. Shah, L. Rota, and P. Lugli. Initial thermalization of photoexcited carriers in GaAs studied by femtosecond luminescence spectroscopy. *Physical review letters*, 66(13):1757–1760, 1991.

[18] R.F. Leheny, J. Shah, R.L. Fork, and C.V. Shank. Dynamics of hot carrier cooling in photoexcited GaAs. *Solid State Commun.*, 31:809, 1979.

[19] Y. Rosenwaks, M.C. Hanna, D.H. Levi, D.M. Szmyd, R.K. Ahrenkiel, and A.J. Nozik. Hot-carrier cooling in GaAs: Quantum wells vs bulk. *Phys. Rev. B*, 48:14675, 1993.

[20] RJ. Seymour, MR. Junnarkar, and RR. Alfano. Slowed picosecond kinetics of hot photogenerated carriers in GaAs. *Solid State Communications*, 41(9):657–660, 1982.

[21] W. Graudszus and EO. G
"obel. Free carrier screening of the Fr
"ohlich interaction in GaAs. *Physica B+C*, 117:555–557, 1983.

[22] M. Pugnet, J. Collet, and A. Cornet. Cooling of hot electron-hole plasmas in the presence of screened electron-phonon interactions. *Solid State Comm.*, 38:531–536, 1981.

[23] R.C.C. Leite. Radiative spectra from hot photocarriers. *Solid-State Electronics*, 21(1):177–178, 1978.

[24] D. Von der Linde, J. Kuhl, and H. Klingenberg. Raman scattering from nonequilibrium LO phonons with picosecond resolution. *Physical Review Letters*, 44(23):1505–1508, 1980.

[25] J. Collet, A. Cornet, M. Pugnet, and T. Amand. Cooling of high density electron-hole plasma. *Solid State Communications*, 42(12):883–887, 1982.

[26] W. Pötz and P. Kocevar. Electronic power transfer in pulsed laser excitation of polar semiconductors. *Phys. Rev. B*, 28:7040, 1983.

[27] P. Kocevar. Hot phonon dynamics. *Physica B+C*, 134(1-3):155–163, 1985.

[28] C. V. Shank, R. L. Fork, R. Yen, J. Shah, B. I. Greene, A. C. Gossard, and C. Weisbuch. Picosecond dynamics of hot carrier relaxation in highly excited multi-quantum well structures. *Solid State Comm.*, 47:981, 1983.

[29] ZY Xu and CL Tang. Picosecond relaxation of hot carriers in highly photoexcited bulk GaAs and GaAs-AlGaAs multiple quantum wells. *Applied Physics Letters*, 44(7):692–694, 1984.

[30] JF. Ryan, RA. Taylor, AJ. Tuberfield, A. Maciel, JM. Worlock, AC. Gossard, and W. Wiegmann. Time-resolved photoluminescence of two-dimensional hot carriers in GaAs-AlGaAs heterostructures. *Physical Review Letters*, 53(19):1841–1844, 1984.

[31] J. Shah, P. Pinczuk, A.C. Gossard, and W. Wiegmann. Energy-loss rates for hot electron and holes in GaAs quantum wells. *Phys. Rev. Lett.*, 18:2045, 1985.

[32] K. Leo, W.W. Rühle, H.J. Queisser, and K. Ploog. Reduced dimensionality of hot-carrier relaxation in GaAs quantum wells. *Phys. Rev. B*, 37:7121, 1988.

[33] K. Leo, W.W. Rühle, and K. Ploog. Hot carrier energy loss rate in $GaAs/Al_xGa_{1-x}As$ quantum wells. *Phys. Rev. B*, 38:1947, 1988.

[34] B. K. Ridley. Electron scattering by confined lo polar phonons in a quantum well. *Phys. Rev. B*, 39(8):5282–5286, Mar 1989.

[35] J. K. Jain and S. Das Sarma. Role of discrete slab phonons in carrier relaxation in semiconductor quantum wells. *Phys. Rev. Lett.*, 62(19):2305–2308, May 1989.

[36] P. Lugli and S.M. Goodnick. Nonequilibrium longitudinal-optical phonon effects in GaAs/AlGaAs quantum wells. *Phys. Rev. Lett.*, 59:716, 1987.

[37] W.S. Pelouch, R.J. Ellington, P.E. Powers, and C.L. Tang. Comparison of hot-carrier relaxation in quantum wells and bulk GaAs at high carrier densities. *Phys. Rev. B*, 45:1450, 1992.

[38] DJ. Westland, JF. Ryan, MD. Scott, JI. Davies, and JR. Riffat. Hot carrier energy loss rates in GaInAs/InP quantum wells. *Solid-State Electronics*, 31(3-4):431–434, 1988.

[39] A.V. Akimov, S.A. Cavill, A.J. Kent, N.M. Stanton, T. Wag, and S. Sakai. Phonon emission by photoexcited carriers in InGaN/GaN multiple quantum wells. *J. Phys. : Condens Matter*, 14:3445, 2002.

[40] P.G. Klemens. Anharmonic decay of optical phonons. *Physical Review*, 148:845–848, 1966.

[41] G. Conibeer, D. König, M.A. Green, and J.F. Guillemoles. Slowing of carrier cooling in hot carrier solar cells. *Thin Solid Films*, 516:6948, 2008.

[42] R. Patterson, M. Kirkengen, B. Puthen Veettil, D. Konig, MA Green, and G. Conibeer. Phonon lifetimes in model quantum dot superlattice systems with applications to the hot carrier solar cell. *Solar Energy Materials and Solar Cells*, 2010.

[43] V. Klimov, P. Haring Bolivar, and H. Kurz. Hot-phonon effects in femtosecond luminescence spectra of electron-hole plasmas in CdS. *Phys. Rev. B*, 52:4728, 1995.

[44] J.B. Rodriguez, P. Christol, L. Cerutti, F. Chevrier, and A. Joullié. MBE growth and characterization of type-II InAs/GaSb superlattices for mid-infrared detection. *Journal of Crystal Growth*, 274:6–13, 2005.

[45] A. Joullié, P. Christol, A.N Baranov, and A. Vicet. Mid-infrared 2-5 μm heterojunction laser diodes. *Topics in Applied Physics*, 89:1–59, 2003.

[46] M. Born and E. Wolf. *Principles of Optics: Electromagnetic Theory of Propagation, Interference and Diffraction of Light.* Pergamon Press Ltd, 1959.

[47] R. Ferrini, M. Patrini, and S. Franchi. Optical functions from 0.02 to 6 eV of AlGaSb/GaSb epitaxial layers. *Journal of Applied Physics*, 84:4517, 1998.

[48] IOFFE. http://www.ioffe.ru/SVA/NSM/Semicond/.

[49] I. Vurgaftman, J. R. Meyer, and L. R. Ram-Mohan. Band parameters for III-V compound semiconductors and their alloys. *Journ. Appl. Phys.*, 89:5815, 2001.

[50] B.K. Ridley. *Quantum processes in semiconductors.* Oxford University Press, 1999.

Chapter 4

Simulation of thermal losses in the absorber

4.1 Basic mechanisms and models

The energy balance equation in chapter 2 introduced a term of heat losses in the absorber P_{Th}. This term was first neglected. In real materials, the thermalization of carriers can not be suppressed, and this term has to be determined to solve the balance equations.

4.1.1 Electron-phonon and phonon-phonon energy transfer

The general frame of electron-phonon interaction has been introduced in section 1.3. In particular, it is said that, in polar semiconductors such as III-V compounds, the Fröhlich interaction coupling electrons to zone center longitudinal optical phonons was dominant over other interactions [1, 2] for temperature above 40 K (depending on the optical phonon energy). In the time scale of the picosecond, it can be considered that

- carrier-carrier scattering is instantaneous (in the femtosecond range at high carrier density) so a thermal distribution is always established
- recombination processes (radiative or not) are very slow, in the order of the nanosecond
- only LO phonon modes are coupled to the electron-hole plasma

In these conditions, the only process involved in the electron-hole plasma energy loss is LO phonon emission. The energy loss rate of carriers is equal to the net variation of the phonon occupation number $N_{\vec{q}}$ due to electron-phonon interaction

mutliplied by the phonon energy $\hbar\omega_{\vec{q}}$ [3]:

$$\left[\frac{dE}{dt}\right]_e = -\sum_{\vec{q}} \hbar\omega_{\vec{q}} \left[\frac{dN_{\vec{q}}(t)}{dt}\right]_c \tag{4.1}$$

where $\vec{q}$ is the wave vector of one LO phonon mode, and $N_{\vec{q}}$ is the occupation number of that phonon mode, given by a Bose-Eintein distribution function at equilibrium. Index c stands for interaction with carriers. LO phonons are also coupled to other phonon modes through anharmonic interactions.

This occupation number varies first because of emission and absorption by electrons, second because of LO phonon decay into other modes. The variation of the occupation number is the sum of the variation due to these two different interactions:

$$\left[\frac{dN_{\vec{q}}(t)}{dt}\right] = \left[\frac{dN_{\vec{q}}(t)}{dt}\right]_c + \left[\frac{dN_{\vec{q}}(t)}{dt}\right]_{ph} \tag{4.2}$$

where index ph stands for interactions with other phonons.

The occupation number evolution due to interactions with electrons can be written:

$$\left[\frac{dN_{\vec{q}}(t)}{dt}\right]_c = \sum_{s}^{e,h} \left[\left(N_{\vec{q}}(t)+1\right) E_{\vec{q}}^{(s)} - N_{\vec{q}}(t) A_{\vec{q}}^{(s)}\right] \tag{4.3}$$

where $E_{\vec{q}}^{(s)}$ is the emission rate of mode $\vec{q}$ due to carrier s (superscript s indicates either an electron or a hole), and $A_{\vec{q}}^{(s)}$ is the absorption rate of mode $\vec{q}$ due to carrier s. The absorption and emission rates depend on the carrier temperature and chemical potential. They were calculated for a Fermi-Dirac distribution in [4]. From this expression, one can define a carrier-phonon scattering time, which is the inverse of the net emission rate.

$$\frac{1}{\tau_{\vec{q}-c}(t)} = \sum_{s}^{e,h} \left[A_{\vec{q}}^{(s)}(t) - E_{\vec{q}}^{(s)}(t)\right] \tag{4.4}$$

This scattering time can be considered independent of the phonon wave vector, considering that only a small region of the Brillouin zone is involved, and it will be called τ_{c-LO}.

The anharmonic term in the phonon occupation evolution is well described by a relaxation-time model from an occupation $N_{\vec{q}}$ towards the equilibrium Planck distribution $N_{\vec{q}}^{(0)}$ at lattice temperature T_L [3]:

$$\left[\frac{dN_{\vec{q}}(t)}{dt}\right]_{ph} = -\frac{N_{\vec{q}}(t) - N_{\vec{q}}^{(0)}}{\tau_{\vec{q}}(T_L)} \tag{4.5}$$

where $\tau_{\vec{q}}(T_L)$ is the optical phonon lifetime. It can be considered independent of $\vec{q}$, and is given by a semi-empirical interpolation formula in [5]:

$$\tau_{LO}(T_L) = \tau_{LO}(0)\left[1 + 2\left[\exp\frac{\hbar\omega_{LO}}{2\mathrm{k_B}T_L} - 1\right]^{-1}\right]^{-1} \tag{4.6}$$

Finally, the total scattering rate is the sum of the electron-phonon scattering rate and the phonon decay rate:

$$\frac{1}{\tau} = \frac{1}{\tau_{c-LO}(t)} + \frac{1}{\tau_{LO}} \tag{4.7}$$

A part of the power absorbed by the carriers is transferred to LO phonon modes, and then dissipated as heat as these modes decay into acoustic modes. The rate of these two processes is given by the two scattering time that are defined above. In GaAs, a typical experimental value of the LO phonon lifetime is 10 ps [6, 7] (depending on the lattice temperature, 10 ps at cryogenic temperature, 4 ps or less at room temperature). The characteristic time of the electron-phonon interaction is the result of the balance between phonon emission and absorption, so it depends on the phonon occupation number. The typical value is below the picosecond (0.1 ps in [8]).

Knowing the rate at which carriers loose their energy, it is possible to estimate the energy loss before carriers are extracted from the absorber. If the extraction time is comparable or smaller than this scattering time, the carriers are extracted before they are fully thermalized, and an additional energy can be collected per electron-hole pair.

4.1.2 The phonon bottleneck effect

In equation 4.2, the time evolution of the LO phonon occupation number is the result of the net emission rate by carriers and the phonon decay by anharmonic interaction. If the carrier density is large enough so the phonon emission rate is higher than the decay rate, LO phonons will accumulate and deviate from the equilibrium distribution. This effect is called the phonon bottleneck effect. As they accumulate, the absorption coefficient increases, so the net phonon emission rate is reduced. A steady state equilibrium is reached for an occupation number that equilibrates the phonon emission rate by carriers and the phonon decay rate.

Several experimental studies have shown the feasibility of generating and monitoring non equilibrium phonon population by optical pumping [6, 9, 10]. The formation and time evolution of this phonon distribution was studied theoretically

and experimentally in [8], showing that information about the band structure (band parabolicity, indirect band gaps...) could be determined from the dependence of the occupation number on the incident photon energy.

The existence of a phonon bottleneck was specifically investigated in quantum structures. The reduction of the carrier energy loss rate observed in quantum wells compared to bulk [11, 12, 13] was attributed to a bottleneck effect that is more efficient than in bulk, because of a longer phonon lifetime [14, 15]. Long life LO phonon can be obtained in quantum structures because of phonon band gaps that may inhibit specific phonon decay paths [16, 17]. The role of phonon interface modes in the scattering of carriers was also pointed out in the case of thin wells ($<$150Å) [18, 19], showing that phonon selection rules can be responsible for a reduction of relaxation rates.

In quantum dots, the discrete nature of the electronic energy levels is expected to have an impact on the electron-phonon coupling, by changing the energy and momentum conservation condition. If the spacing between two energy levels is larger than the LO phonon energy, the fastest scattering process by one LO phonon will be forbidden (processes involving at least two phonons are necessary) and the electron scattering rate is expected to be reduced [20, 21]. The existence of a phonon bottleneck was confirmed experimentally in InGaAs/GaAs QD structures [22, 23] with a measured relaxation time of 7.7 ns at low temperature.

4.1.3 Carrier energy loss rate reduction

It was shown in [3] that the phonon bottleneck effect was indeed responsible for the carrier energy loss rate reduction at high carrier density. Thus, in order to restrain heat losses in the absorber, one has to reinforce this effect. It is actually stronger in quantum structures such as quantum wells and quantum dots, so nanostructured materials should be preferred. Quantum dots however may not be suitable, since carrier extraction from confined states would raise additional issues.

In quantum wells, two different arguments have been proposed to explain the reduced carrier cooling rate: the influence of the selection rules in electron-phonon interaction, and the increase of the LO phonon lifetime. With the former, the effect depends on the well thickness and would play a decisive role with thin wells [18, 19]. The increase of the phonon lifetime would arise from the opening of a band gap in the phonon dispersion relation. The Klemens mechanism that is considered dominant in the LO phonon decay process involves two acoustic modes with energy being half of the LO phonon energy and with opposite $\vec{q}$ vectors. If there is no existing mode that match these conditions, this process is inhibited and the LO phonon decay can be slowed.

By selecting materials with an important atomic mass contrast, for instance indium phosphide, it is possible to have a dispersion relation such that the density of states at half the LO phonon energy is zero. In such material, the carrier energy loss rate is expected to be reduced compared to GaAs, which is verified theoretically and experimentally [24]. The use of nanostructured materials could enable to design a structure having the desired phononic band gap with a large variety of material. Such phononic engineering is proposed in [16, 17]. However, obtaining a 3D phononic band gap may not be achievable with quantum wells, and would require a three dimensional quantization of the material.

4.2 Introduction of heat losses in the energy balance

4.2.1 Constant characteristic time for thermalization

A first approach to introduce heat losses in hot carrier solar cell models was to consider an exponential decrease of the carrier energy with a characteristic time τ_{th} [25, 26]. The energy that is available for extraction is considered here to be the energy of the photogenerated electron-hole pair ε, decreased to be $\tilde{\varepsilon}$ due to thermalization, where $\tilde{\varepsilon}$ is given by

$$\begin{aligned} \tilde{\varepsilon} &= \varepsilon F + (1-F)(\varepsilon_g + 3\mathrm{k_B}T_C) \\ F &= exp\left(\frac{\tau_{re}}{\tau_{th}}\right) \end{aligned} \tag{4.8}$$

where ε_g is the band gap energy, τ_{re} is the carrier retention time (time before extraction), and τ_{th} is the thermalization time constant. T_C is the temperature of the lattice. F is here the probability for a carrier to be not thermalized after retention time τ_{re}, so the energy distribution of carriers is an average between a non equilibrium population (with probability F) and a equilibrium population at temperature T_C (with probability $1-F$).

Another approach was then proposed [27] in which the power transfer from carriers to phonons is proportional to the energy difference between the excited state and the equilibrium state. The energy loss rate of one carrier is then obtained by taking the difference between the average energy of a non equilibrium carrier population at temperature T_H and the average energy of a fully equilibrated population with the cold temperature of the lattice T_c, divided by a thermalization time constant. The power lost by thermalization is then the sum of the energy

loss rate of individual electrons and holes multiplied by their respective densities:

$$P_{th} = n_e d\frac{\varepsilon(\mu_e, T_H) - \varepsilon(\mu_e, T_C)}{\tau} + n_h d\frac{\varepsilon(\mu_h, T_H) - \varepsilon(\mu_h, T_C)}{\tau} \tag{4.9}$$

where $\varepsilon(\mu, T)$ is the average energy of a Fermi-Dirac distribution at potential μ and temperature T, τ is the thermalization time constant, d is the thickness of the absorbing layer, and n_e and n_h are the electron and hole densities. This model enables to consider different temperatures and chemical potentials for electrons and holes, and also different thermalization times. The power lost by thermalization is a function of T_e, T_h, μ_e and μ_h.

A major issue is raised by these approaches, where the characteristic time for carrier thermalization is considered independent of carrier density and temperature. It has been demonstrated, in particular, that the thermalization rate was reduced at high carrier density [3, 13]. An other model, that takes into account the saturation of the thermalization rate at high carrier density, could be more relevant in this situation.

4.2.2 Thermalization coefficient

A model of the carrier energy loss rate is proposed in [28]:

$$\frac{dE}{dt} = \frac{\hbar\omega_{LO}}{\tau}\exp\left(-\frac{\hbar\omega_{LO}}{\mathrm{k_B}T_H}\right) \tag{4.10}$$

with a thermalization time τ that is a function of the carrier temperature T_H and of the carrier density n. The part of the incident areal power density that is lost by thermalization is then obtained by multiplying this quantity by the carrier density, and by the thickness d of the absorbing layer. It is shown in chapter 3 that this power density loss, related to the LO phonon decay rate, could be written when a phonon bottleneck occurs, with a thermalization coefficient Q:

$$P_{th} = Q(T_H - T)\exp\left(-\frac{\hbar\omega_{LO}}{\mathrm{k_B}T_H}\right) \tag{4.11}$$

where Q is a material constant, independent of the carrier temperature or density. This expression is fitted to experimental data, and an experimental determination of Q is possible.

In high injection regime ($P_{abs} \gg Q\Delta T$), the carrier temperature tends to increase, which then leads to an increase of the heat dissipation. This increase then acts as a negative feedback on the carrier temperature. In low injection regime, a

carrier temperature close to the lattice temperature is found because P_{th} is necessarily lower than P_{abs}. P_{th} is the power lost by carriers by thermalization in steady state that can be introduced in the energy balance of the sytem.

4.2.3 Charge and energy balance

The same formalism as in chapter 2 can be used for the energy and charge balance equation, with an additional term due to the power lost by thermalization (equation 4.12). These equations can be solved with exactly the same method, since P_{th} in equation 4.11 is only a function of the carrier temperature for a given incident power.

$$\begin{cases} J_e^+(\mu_e, T_e) - J_e^-(\mu_n, T) = J_h^+(\mu_h, T_h) - J_h^-(\mu_p, T) \\ \qquad\qquad\qquad\qquad\qquad\quad = J_{abs} - J_{em}(\Delta\mu_H, T_H) \\ P_e^+(\mu_e, T_e) - P_e^-(\mu_n, T) + P_h^+(\mu_h, T_h) - P_h^-(\mu_p, T) \\ \qquad\qquad\qquad\qquad\qquad\quad = P_{abs} - P_{em}(\Delta\mu_H, T_H) - P_{th}(T_H) \end{cases} \tag{4.12}$$

The same polynomial formulation as in chapter 2 is obtained, with the carrier temperature and quasi Fermi level splitting determined after finding the roots of the polynomial:

$$\alpha(T_H)X^2 + \beta(T_H)X + \gamma(T_H) = 0 \tag{4.13}$$

$\alpha(T_H)$ and $\beta(T_H)$ being defined similarly. The difference is that γ is now a function of T_H, defined by

$$\gamma(T_H) = \frac{P_{th}(T_H) - P_{abs}}{f_4(T)} + \frac{Jabs}{f_3(T)} \tag{4.14}$$

The system can then be solved and the cell efficiency is determined as a function of the thermalization coefficient Q.

4.3 Results and discussion

4.3.1 Validation of the model

It is possible to compare the results given by this model with previous models. It was shown in section 2.3.1 that it is in agreement with the Ross-Nozik model for ideal hot carrier solar cells. With the introduction of heat losses in the absorber, it is now possible to compare with a model of fully thermalized conventionnal solar cells.

Results are presented in figure 4.1. Here, the efficiency and losses given by the model of hot carrier solar cells that includes both non ideal selective contacts and thermalization in the absorber as a function of the absorber band gap are presented in solid lines, compared with the Shockley-Queisser model for solar cell efficiency, represented by empty circles. Conditions for the first model are a fast thermalization ($Q > 100\ W/K/\mathrm{cm}^2$), so the carriers are close to thermal equilibrium, and non selective contacts ($\delta E \gg \mathrm{k}T_H$ and $E_{ext} = E_g$) to match the conditions of conventionnal solar cells.

A very good agreement is found between the two models over the whole band gap range, on efficiency as well as on the different types of losses.

4.3.2 Influence of thermalization in the absorber

The carrier chemical potential $\Delta\mu_H$ and temperature T_H, as well as the current density and power density delivered by the cell are plotted as a function of the output voltage in figure 4.2, for extraction energies ranging from 1.2 eV to 3 eV, and in the same conditions as in figure 2.10 ($E_g = 1$ eV, full concentration) but with a thermalization coefficient $Q = 1\ \mathrm{W/K/cm}^2$.

The high temperature and negative chemical potential are still observed when the current density is maximal, for E_{ext} below 1.8 eV. The carrier temperature is however strongly reduced compared to the situation in which carrier thermalization was neglected. Here, when the carrier temperature increases, the heat loss increases and acts as a negative feedback on the carrier temperature. Much more realistic T_H values are found, even with a rather low thermalization coefficient. At E_{ext} values above 1.8 eV, the cell behaves comparably to the case of neglected thermalization, with a lower carrier temperature and lower efficiency.

In order to evaluate the effect of thermalization alone, and the thermalization rate that has to be targeted to enable an efficiency enhancement, the efficiency and losses are calculated as a function of the thermalization coefficient Q in the conditions of very selective contacts and under fully concentrated sun light. The band gap is taken 1 eV. Results are shown in figure 4.3.

As expected, the efficiency is close to the optimal efficiency of an ideal unthermalized hot carrier solar cell when the thermalization coefficient tends to very small values, and is close to the Shockley-Queisser efficiency for large thermalization coefficient. The transition between fully thermalized and unthermalized behaviour occurs in a Q range between 10^{-1} and $10^2\ \mathrm{W/K/cm}^2$. The short circuit current is unchanged by the change of thermalization rate, and the variation of efficiency is related to the open circuit voltage. At low thermalization rates, large open circuit voltages are achievable, thanks to a higher temperature which enables

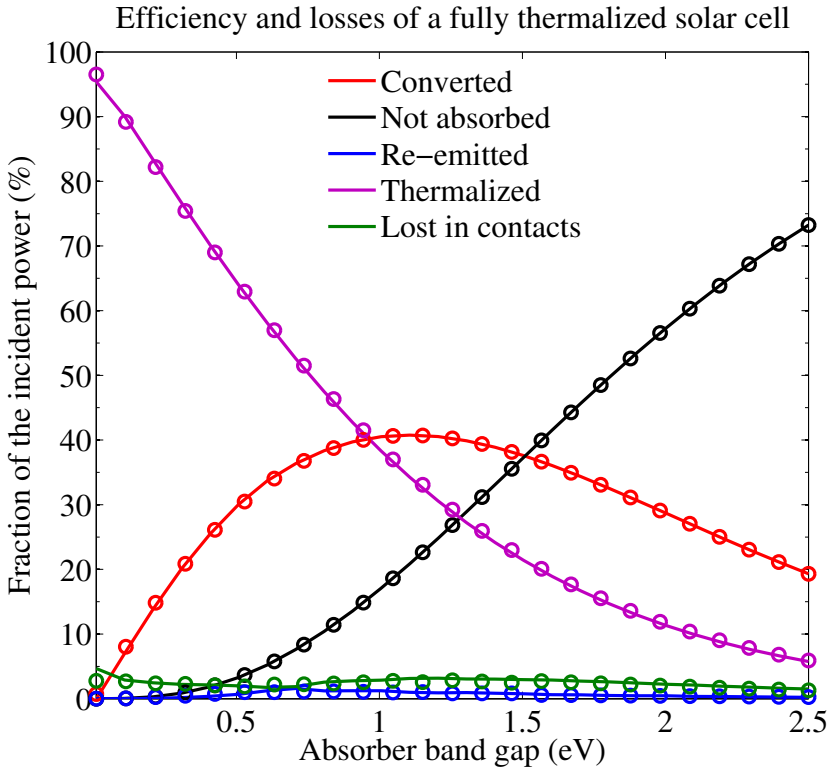

Figure 4.1: Fraction of the incident power that is converted (red), not absorbed (black), lost by radiative recombination (blue), lost in the selective contacts (green), and lost by thermalization (purple), obtained using the Shockley-Queisser model (empty circles), or with the hot carrier solar cell (solid lines) in the case of non selective contacts ($\delta E \gg \mathrm{k}T_H$), extraction energy being the absorber band gap, and fast thermalization ($Q > 100$ W/K/cm^2), under full concentration of the incident sun light. Very good agreement is obtained between the two models.

to use a larger extraction energy. The raise of the carrier thermalization rate leads to an increase of the heat loss in the absorber, which is visible in figure 4.3.

The thermalization coefficient range for which the transition occurs from negligible themalization (below 10^{-1} W/K/cm^2) to a fully thermalized situation (above 10^2 W/K/cm^2) has to be compared with the experimental values of this thermalization coefficient obtained in chapter 3. The lowest values measured at low temperature (80 K) were close to 50 W/K/cm^2, and extrapolations at ambient temperature indicate a predictible thermalization coefficient of 80 W/K/cm^2. The

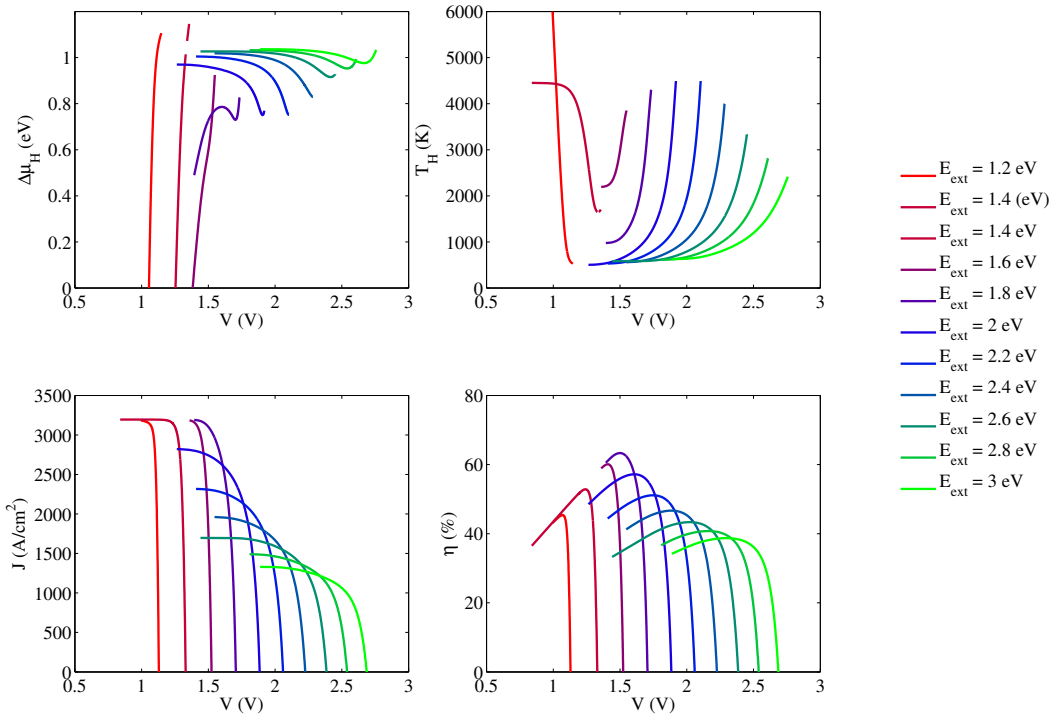

Figure 4.2: Carrier chemical potential, carrier temperature, current and power versus voltage with a 1 eV band gap absorber, highly selective contacts ($\delta E = 1$ meV), under full concentration and with a thermalization coefficient $Q = 1$ W/K/cm^2, with different extraction energy from 1.2 eV to 3 eV.

samples tested here would then be almost fully thermalized under full concentration, providing only a 46% upper efficiency limit, compared to the 41% Shockley-Queisser limit. In fact, the actual potential efficiency improvement would be better because of band gap is 0.65 eV and not 1 eV in this example. With a 0.65 eV band gap absorber, the potential efficiency with $Q = 80$ W/K/cm^2 is 44% compared to 35% in the case of a fully thermalized absorber, which represents a 26% improvement. With a 1 eV band gap absorber, only a 12% improvement is obtained (46% compared to 41%).

According to simulations, the samples that have been studied in chapter 3, do not enable a strong efficiency improvement, even in full concentration conditions,

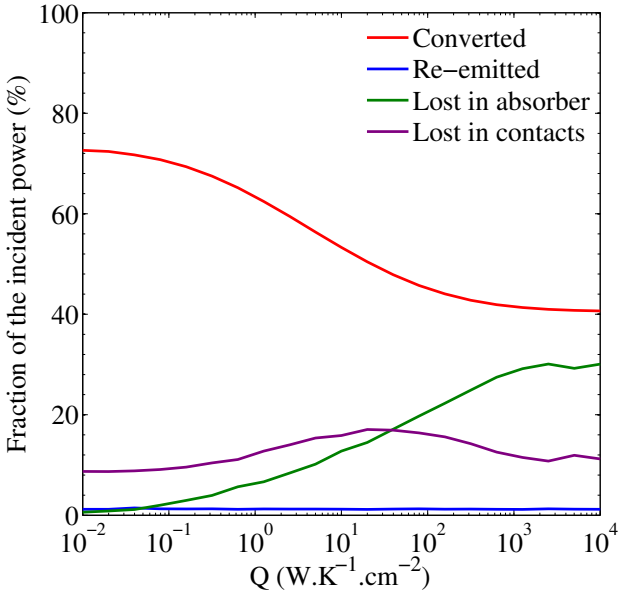

Figure 4.3: Efficiency (red), radiative losses (blue), heat losses in the absorber (green) and heat losses in contacts (purple) as a function of the thermalization coefficient, with a 1 eV band gap absorber under full concentration and with perfectly selective contacts. Below 0.1 W.K^{-1}.cm^{-2}, the thermalization becomes negligible. Above 100 W.K^{-1}.cm^{-2}, the cell can be considered fully thermalized.

and only a limited effect is expected. Optimized structures are necessary to reach lower thermalization rates, and thus to achieve ultra high efficiency.

4.3.3 Thermalization and concentration

A reduced thermalization rate is observed when the power injected in the carrier plasma by photon absorption exceeds the capacity of the material to dissipate this power by phonon emission. It was shown above that for a given incident power corresponding to maximal concentration of sun light, the heating of the plasma requires a thermalization coefficient below 10^2 W/K/cm^2. At lower, and more realistic, incident power, a similar behaviour would still be possible, but would require a lower thermalization rate. In other words, the lower the thermalization rate can be, the less one has to concentrate the incident power to trigger the carrier heating and efficiency enhancement.

The efficiency of a hot carrier solar cell as a function of its thermalization coefficient is presented in figure 4.4 for different concentration ratios, from 100 suns to full concentration (46 000 suns). The cell that is considered has a 1 eV band gap absorber and perfectly selective contacts.

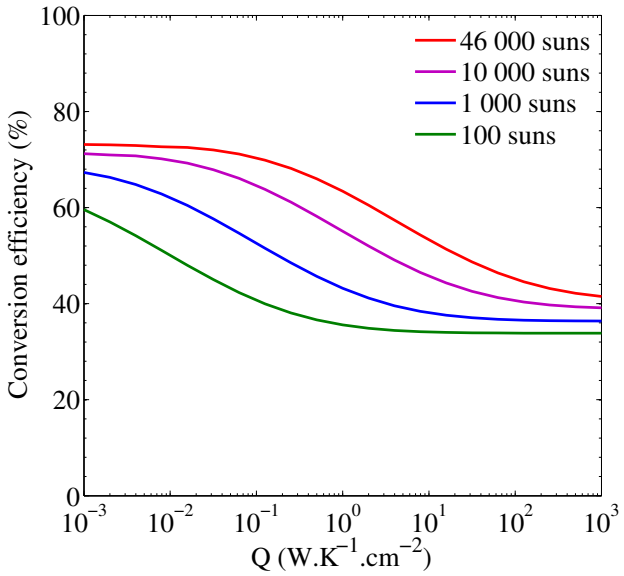

Figure 4.4: Conversion efficiency as a function of the thermalization coefficient, with a 1 eV band gap absorber and perfectly selective contacts, with concentration ranging from 100 to 46000 suns.

First, the potential efficiency of the cell, in the whole Q range, is larger with a higher concentration ratio. This is a common result for all types of cells, from conventional single junction to ideal hot carrier solar cells, as long as resistive losses due to the large current densities involved are neglected. One can notice that, for a given value of Q, the difference in efficiency between two different concentrations is larger in the transition range ($Q \in [10^{-1}, 10^{2}]$ W/K/cm^2 for instance in the full concentration case) than in the limiting cases where thermalization can be considered either negligible or complete. In the two limit cases, a 2% efficiency improvement per decade of concentration is observed, compared to approximately 10% increase in the transition range. This means that the efficiency enhancement due to concentration can be stronger with hot carrier solar cells in this range, than for conventional cells.

A second noticeable effect is the shift of the transition range towards lower

values of Q when the concentration is reduced. For a concentration ratio of 10000 suns, which is the order of magnitude of the highest achievable concentration today, a thermalization coefficient below 10 $W.K^{-1}.cm^{-2}$ is necessary to observe an efficiency enhancement. For a 1000 suns concentration (the best concentration achievable in large scale application), one has to go to Q values below 1 $W.K^{-1}.cm^{-2}$, much below the thermalization rates measured so far.

Very large concentration can be achieved using lasers, so the hot carrier effect can be tested with existing samples. However, before industrial application can be considered, a lot of effort has to be put into finding new materials, and designing new structures, that would strongly reduce the carrier thermalization rate. A thermalization coefficient between 0.1 and 1 $W.K^{-1}.cm^{-2}$ has to be targeted.

4.3.4 Thermalization and selective contacts

In the previous sections, the selective contacts were considered ideal. In practical conditions, however, heat losses will occur in the absorber as well as in the contacts. The efficiency of a cell as a function of the contact transmission width is presented in figure 4.5 for different values of the thermalization.

For low Q, the efficiency evolves with the transmission range similarly to what was observed in chapter 2 in the case of neglected thermalization, from a perfectly selective limit below 10 meV to a semi-selective limit above 500 meV. The efficiency drop between these two limits is approximately 12% absolute efficiency. When the thermalization rate is increased, the cell efficiency is reduced in the whole range of transmission width. However the efficiency drop is more pronounced in the high selectivity range. The efficiency is still higher with narrower contacts, but the efficiency difference is reduced. It is 6% with $Q = 1$ $W.K^{-1}.cm^{-2}$, and only 1% with $Q = 100$ $W.K^{-1}.cm^{-2}$.

It was pointed out in chapter 2 that the benefit that can be expected with highly selective contacts was in fact not great compared to semi-selective contacts, and that it would not compensate the technological challenge that they would represent. It is even more striking with realistic hot carrier solar cell whose thermalization rate is not negligible, for which the efficiency drop between highly selective and semi-selective contacts is strongly reduced.

This can be explained when one looks at heat losses through contacts (figure 4.6) and heat losses in the absorber (figure 4.7) as a function of the contact transmission width. When the transmission width is increased, the heat losses in the contacts increases as expected, and for all values of the thermalization coefficient. The raise is less pronounced with fast thermalization, but still visible.

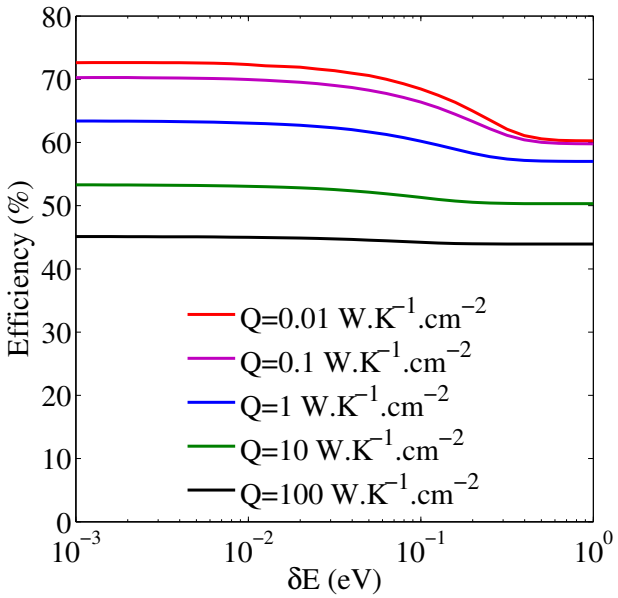

Figure 4.5: Efficiency of a 1 eV band gap hot carrier solar cell under full concentration and with thermalization coefficient ranging from 0.01 to 100 W.K^{-1}.cm^{-2}, as a function of the contact transmission width. The efficiency decrases with increased thermalization rate. The reduction is stronger with highly selective contacts than with semi-selective contacts ($\delta E > 0.5$ eV).

At the same time, the heat losses in the absorber (*ie* due to carrier thermalization) decrease with the transmission range increase, and the drop is more and more visible when Q increases. This heat loss reduction compensates the heat flow at the contacts, so the overall losses become almost constant at large thermalization coefficient.

On these two figures, the curves are noisy. This come from a convergence issue: these quantities are strongly dependent on the extraction energy. When δE is changed, a new optimal extraction energy is found that gives the best efficiency. With a small variation of the extraction energy, the total heat loss is unchanged (the sum of losses in contacts and in the absorber give smooth curves), but its distribution between contacts and the absorber may be modified. A small variation on the optimal extraction energy can then result in a noticeable and opposite variation of the two different types of heat losses. It has no consequence on the cell efficiency represented by smooth curves in figure 4.5.

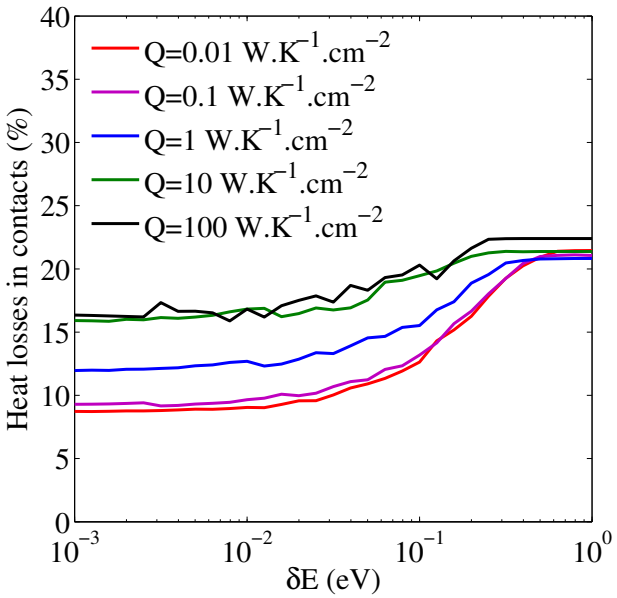

Figure 4.6: Heat losses in contacts of a 1 eV band gap hot carrier soalr cell under full concentration and with thermalization coefficient ranging from 0.01 to 100 W.K^{-1}.cm^{-2}, as a function of the contact transmission width. The heat flow increases with increased thermalization rate with highly selective contacts ($\delta E < 100$ meV). It is fairly independent of the thermalization coefficient with non selective contacts ($\delta E > 500$ meV).

The reduction of the heat losses in the absorber with non selective contacts comes from the reduction of the carrier temperature. With a large contact transmission range, an important part of the incident power flows outside of the absorber as carriers are extracted, which reduces the residual energy in the electron-hole plasma. The carrier temperature is therefore lower. The heat losses in the absorber, given by expression 4.11, depends on the carrier temperature, and is maximal at high temperature. The lower temperatures that are attained with non selective contacts result in a reduced thermalization loss. The heat flow through contacts do not add to the heat losses in the absorber, but a part of the thermalization losses are replaced by an increased heat flux.

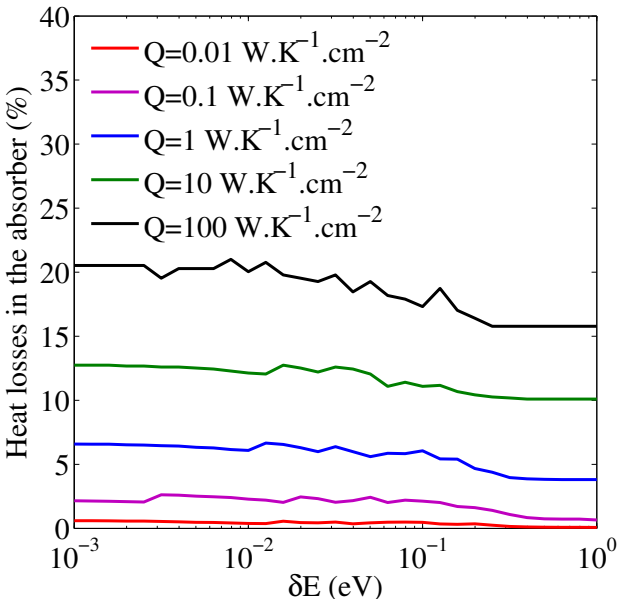

Figure 4.7: Heat losses in the absorber of a 1 eV band gap hot carrier solar cell under full concentration and with thermalization coefficent ranging from 0.01 to 100 W.K^{-1}.cm^{-2}, as a function of the contact transmission width. The heat loss decreases with increased transmission width counterbalancing the increase of the heat flow at the contacts, for all values of Q. The heat loss reduction is more pronounced with fast thermalization.

4.4 Conclusion

Based on the electron energy loss mechanisms, a simple model for thermalization losses is integrated in the hot carrier solar cell model. The influence of the thermalization rate on the cell efficiency can be investigated. This study allows to estimate the required thermalization rate that would enable a hot carrier effect and an efficiency enhancement.

It turns out that cooling rates lower than the experimental values obtained on GaSb-based samples should be targeted. At 46000 suns (full concentration), a 26% relative efficiency improvement is expected on the upper limit of efficiency between a cell having a thermalization rate as measured in chapter 3 and a fully thermalized cell (44% vs 35%).

The situation is even more unfavourable with a more realistic concentration

ratio. At 1000 suns, a thermalization coefficient Q below 1 $W.K^{-1}.cm^{-2}$ would be necessary to enable an efficiency improvement.

When thermalization is considered, the efficiency difference between perfectly selective and semi-selective contacts is reduced, and the faster the thermalization is, the smaller the difference will be. This is another argument in favor of semi-selective contacts.

Bibliography

[1] B.K. Ridley. *Quantum processes in semiconductors.* Oxford University Press, 1999.

[2] P.Y. Yu and M. Cardona. *Fundamentals of Semiconductors, Physics and Material Properties.* Springer-Verlag, 2001.

[3] W. Pötz and P. Kocevar. Electronic power transfer in pulsed laser excitation of polar semiconductors. *Phys. Rev. B*, 28:7040, 1983.

[4] S.M. Kogan. On the theory of hot electrons in semiconductors. *Sov. Phys. Solid State*, 4:1813–1819, 1963.

[5] P.G. Klemens. Anharmonic decay of optical phonons. *Physical Review*, 148:845–848, 1966.

[6] D. Von der Linde, J. Kuhl, and H. Klingenberg. Raman scattering from nonequilibrium LO phonons with picosecond resolution. *Physical Review Letters*, 44(23):1505–1508, 1980.

[7] A. Othonos. Probing ultrafast carrier and phonon dynamics in semiconductors. *Applied Physics Reviews*, 83:1789, 1998.

[8] C.L. Collins and Y.Yu. Generation of nonequilibrium optical phonons in GaAs and their application in studying intervalley electron-phonon scattering. *Phys. Rev. B*, 30:4501, 1984.

[9] J. Shah, R.C.C. Leite, and JF Scott. Photoexcited hot LO phonons in GaAs. *Solid State Communications*, 8(14):1089–1093, 1970.

[10] J.C.V. Mattos and R.C.C. Leite. Non equilibrium phonon distribution and electron-phonon coupling in semiconductors. *Solid State Communications*, 12(6):465–468, 1973.

[11] J. Shah, P. Pinczuk, A.C. Gossard, and W. Wiegmann. Energy-loss rates for hot electron and holes in GaAs quantum wells. *Phys. Rev. Lett.*, 18:2045, 1985.

[12] W.S. Pelouch, R.J. Ellington, P.E. Powers, and C.L. Tang. Comparison of hot-carrier relaxation in quantum wells and bulk GaAs at high carrier densities. *Phys. Rev. B*, 45:1450, 1992.

[13] Y. Rosenwaks, M.C. Hanna, D.H. Levi, D.M. Szmyd, R.K. Ahrenkiel, and A.J. Nozik. Hot-carrier cooling in GaAs: Quantum wells vs bulk. *Phys. Rev. B*, 48:14675, 1993.

[14] W. Cai, MC Marchetti, and M. Lax. Nonequilibrium phonon effect on time-dependent relaxation of hot electrons in semiconductor heterojunctions. *Physical Review B*, 35(3):1369, 1987.

[15] P. Lugli and S.M. Goodnick. Nonequilibrium longitudinal-optical phonon effects in GaAs/AlGaAs quantum wells. *Phys. Rev. Lett.*, 59:716, 1987.

[16] G. Conibeer, D. König, M.A. Green, and J.F. Guillemoles. Slowing of carrier cooling in hot carrier solar cells. *Thin Solid Films*, 516:6948, 2008.

[17] R. Patterson, M. Kirkengen, B. Puthen Veettil, D. Konig, MA Green, and G. Conibeer. Phonon lifetimes in model quantum dot superlattice systems with applications to the hot carrier solar cell. *Solar Energy Materials and Solar Cells*, 2010.

[18] B. K. Ridley. Electron scattering by confined lo polar phonons in a quantum well. *Phys. Rev. B*, 39(8):5282–5286, Mar 1989.

[19] J. K. Jain and S. Das Sarma. Role of discrete slab phonons in carrier relaxation in semiconductor quantum wells. *Phys. Rev. Lett.*, 62(19):2305–2308, May 1989.

[20] U. Bockelmann and G. Bastard. Phonon scattering and energy relaxation in two-, one-, and zero-dimensional electron gases. *Physical Review B*, 42(14):8947, 1990.

[21] X.Q. Li, H. Nakayama, and Y. Arakawa. Phonon bottleneck in quantum dots: Role of lifetime of the confined optical phonons. *Physical Review B*, 59(7):5069, 1999.

[22] J. Urayama, T.B. Norris, J. Singh, and P. Bhattacharya. Observation of phonon bottleneck in quantum dot electronic relaxation. *Phys. Rev. Lett.*, 86:4930, 2001.

[23] R. Heitz, H. Born, F. Guffarth, O. Stier, A. Schliwa, A. Hoffmann, and D. Bimberg. Existence of a phonon bottleneck for excitons in quantum dots. *Physical Review B*, 64:241305, 2001.

[24] U. Hohenester, P. Supancic, P. Kocevar, XQ Zhou, W. K
"utt, and H. Kurz. Subpicosecond thermalization and relaxation of highly

photoexcited electrons and holes in intrinsic and p-type GaAs and InP. *Physical Review B*, 47(20):13233, 1993.

[25] Y. Takeda, T. Ito, R. Suzuki, T. Motohiro, S. Shrestha, and G. Conibeer. Impact ionization and auger recombination at high carrier temperature. In 17^{th} *International Photovoltaic Science and Engineering Conference, 3-7 December 2007, Kukuoka, Japan*, 2007.

[26] Y. Takeda, T. Ito, T. Motohiro, T. Nagashima, D. König, S. Shrestha, and G. Conibeer. Solar energy conversion using temperature-controlled carriers. In 22^{nd} *European Photovoltaic Solar Energy Conference, 3-7 september 2007, Milan, Italy*, 2007.

[27] P. Aliberti, Y. Feng, Y. Takeda, SK Shrestha, MA Green, and G. Conibeer. Investigation of theoretical efficiency limit of hot carriers solar cells with a bulk indium nitride absorber. *Journ. Appl. Phys.*, 108:094507, 2010.

[28] S.A. Lyon. Spectroscopy of hot carriers in semiconductors. *Journal of Luminescence*, 35:121, 1986.

Chapter 5

Efficiency of realistic cells

The heat losses in the absorber and in the contacts being accounted for in the hot carrier solar cell model, it is now possible to evaluate the potential efficiency of a realistic solar cell. After evaluating the absorption in a test structure, the achievable efficiency under practical conditions is determined. Finally a roadmap to a 50% efficiency solar cell is proposed.

5.1 Absorption

It was shown that a high carrier density in the absorber is beneficial for the reduction of the carrier thermalization rate. A drop in thermalization rates is observed around 10^{19} cm^{-3} . This can be achieved, first by concentrating the incident photon flux, then by absorbing this photon flux in a small material thickness. Without concentration, the incident photon flux is of the order of 10^{18} s^{-1}cm^{-2}. Assuming it is completely absorbed in a 1 μm absorber, and assuming a time scale of 1 ns for carrier extraction, the carrier density would be of the order of 10^{13} cm^{-3}. The carrier retention time can not be lengthened if one needs to restrain thermalization losses. Some effort needs to be put into light concentration and thickness reduction.

Full concentration of the incident light corresponds to a factor 46000 on the incident power density and photon flux, so 5 orders of magnitude may be gained on the carrier density by going to very high concentration ratio. Beside the technological challenge to reach 10000 suns concentration, this may not be sufficient to meet the requirements in carrier density. A reduction of the absorbing thickness is necessary. A 50 nm absorbing layer is targeted here.

The absorption by a 50 nm GaSb layer on a silver back reflector was calculated

Configuration	Absorption (in %)	
	photons	energy
GaSb + Ag mirror		37.5
SiC AR coating + GaSb + Ag mirror		45.5
ideal AR coating + GaSb + Ag mirror		52.5
resonant structure + GaSb + Ag mirror	54	66

Table 5.1: Compared absorption of a 50 nm GaSb layer on a silver mirror, without antireflection coating, with a SiC antireflection coating, with an ideal antireflection coating and with a resonant structure 5.1, with a $1/\sqrt{2}$ numerical aperture.

as a function of the concentration ratio. With a numerical aperture $NA = 1/\sqrt{2}$ (*ie* under concentration corresponding to about 13000 suns), only 37.5% of the incident energy flux is absorbed [1]. The addition of an antireflection (AR) SiC layer on top allows to reach 45.5% absorption. Even an ideal antireflection coating (no losses in the AR layer, no reflection at the air/AR layer and AR layer/absorbing layer interfaces) would only give 52.5% absorption (results listed in table 5.1). It means that, without specific care attached to light absorption, already half of the incident power is lost because the layer is to thin to absorb it.

The power absorbed locally in a material depends on the product $\alpha(\varepsilon) \times E^2$ where E is the local electric field, $\alpha(\varepsilon)$ is the material absorption coefficient as a function of the energy ε, that is related to the imaginary part of the complex refractive index by $\alpha(\varepsilon) = \dfrac{4\pi\Im(n(\varepsilon))}{\lambda}$. This is true for the attenuation of a plane wave. For nanostructures with complicated field patterns, the relevant quantity is no longer that one but $\dfrac{4\pi\Im(n(\varepsilon))}{\lambda}\Re(n(\varepsilon))\dfrac{\varepsilon_0 c E^2}{2}$, where $\Re(n(\varepsilon))$ is the real part of the refractive index [2].

The refractive index is a material constant and is not a tunable parameter. The enhancement of the absorption implies therefore an increase of the local electromagnetic field intensity. In other words, the incident light has to be focused and trapped in the absorbing layer.

A first idea to manage light trapping is the use of a Fabry-Perot resonator. It can lead to a very high light intensity in the cavity of the resonator, but the enhancement is strongly wavelength and incident angle dependant. The incident spectrum being polychromatic and coming from different directions when concentrated, this solution is not ideal.

Another solution is proposed [1] that consists in an asymmetric SiC grating

(see figure 5.1). The effect of such grating is double: the triangle shape of the grating acts as an equivalent graded index layer resulting in a good impedance matching between air and the GaSb layer, and it also generates a large number of modes in the structure that cover the (ω, k) plane. A broadband and wide-angle resonance is obtained that way. The resulting absorption enhancement is stronger than with an ideal AR coating. Absorption reaches 66% of the incident photon flux at $NA = 1/\sqrt{2}$, which represents a 26% improvement compared to the perfect AR case, and 76% improvement compared to the reference case of a GaSb layer on a silver mirror.

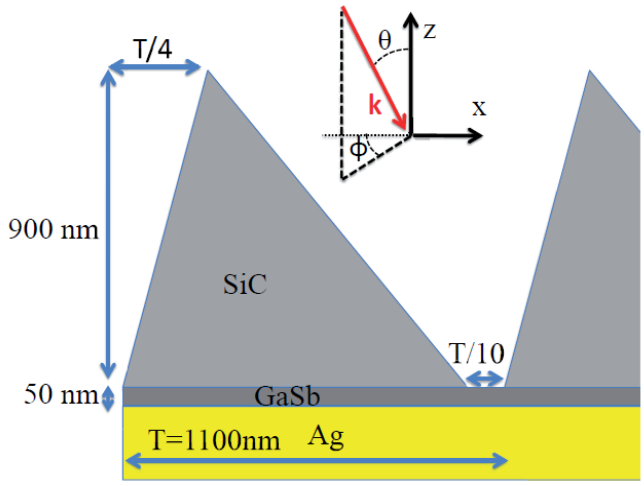

Figure 5.1: Dielectric structure designed for absorption enhancement in a 50 nm thick GaSb layer on a silver back reflector.

The absorptivity of this structure is computed, using the GaSb absorption coefficient [3], as a function of the incident direction (θ, φ, see figure 5.1) and of the photon wavelength (λ). For each $[\theta, \varphi, \lambda]$ triplet, the fraction of the incident power density that is absorbed in the GaSb layer is computed. An example of the result obtained in the case of $\varphi = 0$ is proposed in figure 5.2.

The integrated absorptivity over directions for a solid angle corresponding to a numerical aperture $NA = 1/\sqrt{2}$ as a function of the wavelength is presented in figure 5.3. It represents the part of the light incident on the surface inside a cone of half-angle $\theta = \frac{\pi}{4}$ that is absorbed. The photon and energy distributions that correspond to a black body spectrum at 6000 K are also plotted. The absorptivity of the structure matches quite well the shape of the incident spectrum for optimal

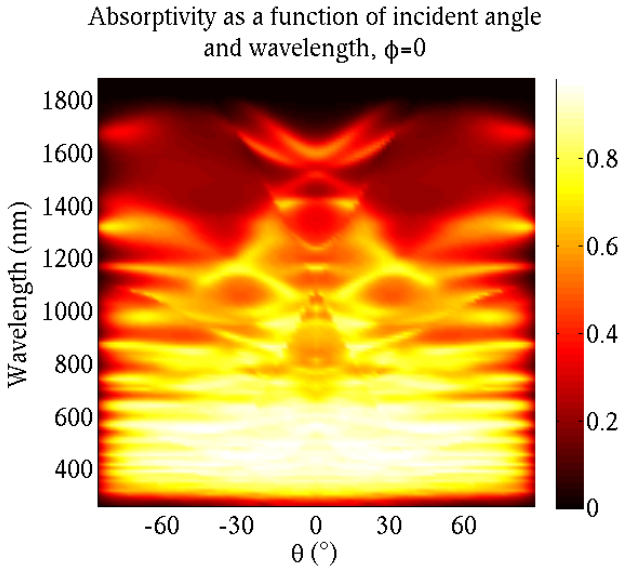

Figure 5.2: Computed absorptivity as a function of incident angle and wavelength.

absorption. High energy photons are more efficiently absorbed which results in an absorbed fraction of incident energy of 66%, higher than the 54% absorbed fraction of incident photons.

The absorbed fraction of incident photon flux β^p, and the absorbed fraction of incident energy flux β^E are given by:

$$\beta^p(NA) = \frac{\int_\lambda \int_0^{\theta_0} \int_0^{2\pi} a(\lambda,\theta,\varphi) f(\lambda) d\lambda d\theta d\phi}{\int_\lambda \int_0^{\theta_0} \int_0^{2\pi} f(\lambda) d\lambda \sin(\theta) d\theta d\phi} \tag{5.1}$$

and

$$\beta^E(NA) = \frac{\int_\lambda \int_0^{\theta_0} \int_0^{2\pi} a(\lambda,\theta,\varphi) f(\lambda) \frac{hc}{\lambda} d\lambda d\theta d\phi}{\int_\lambda \int_0^{\theta_0} \int_0^{2\pi} f(\lambda) \frac{hc}{\lambda} d\lambda \sin(\theta) d\theta d\phi} \tag{5.2}$$

where $f(\lambda)$ is the isotropic black body photon density per solid angle wavelength. θ_0 is the half angle of the cone with numerical aperture $NA = \sin(\theta_0)$. These quantities are plotted in figure 5.4.

The absorptivity is found to be weakly dependant on the numerical aperture, even at very large angles. For instance, a concentration of 10000 suns corresponds to a numerical aperture of 0.62, which gives 68% of the energy flux absorbed.

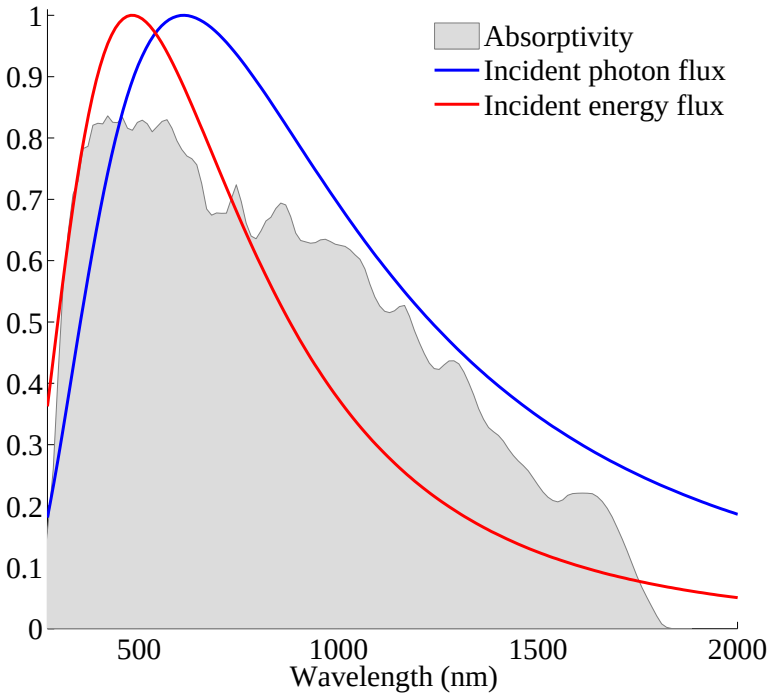

Figure 5.3: Computed absorptivity integrated over a solid angle $\Omega = 2\pi(1 - cos(\theta))$, $\theta = \pi/4$ ($NA = 1/\sqrt{2}$) as a function of the wavelength (in grey), and the normalized incident photon (blue) and energy (red) flux corresponding to a black body spectrum at 6000 K.

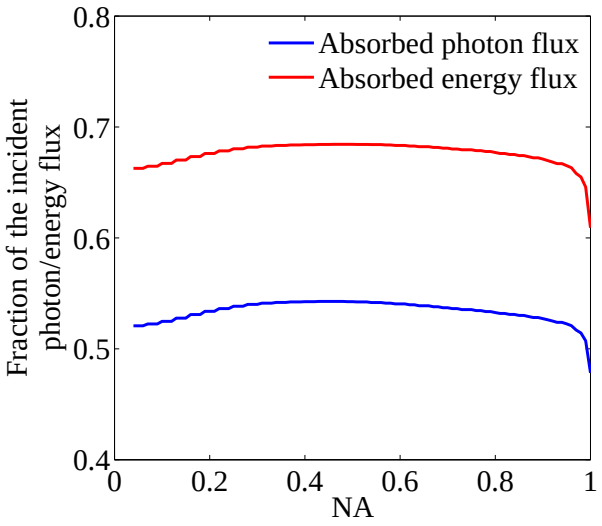

Figure 5.4: Fraction of the incident photon (blue) and energy (red) flux that is absorbed, integrated over wavelength and directions, as a function of the numerical aperture and for a 6000 K black body incident spectrum.

The technological feasibility of such triangle grating may be a problem. An option would be to replace the triangle with a stack of several SiC layers with decreasing fill factor (see figure 5.5). Such stacked layers would be an approximation of the triangle shape. The number and thicknesses of these layers can be tuned: the more and the thinner they are, the closer it gets to the optimal triangle shape, and the more complex and expensive the technological process will be.

5.2 The hot carrier solar cell in practical conditions: achievable efficiency

5.2.1 Numerical resolution

In this section, the method for the determination of a cell efficiency in practical condition is presented. The method proposed in section 2.2.2 is not applicable since it requires an analytical expression for the different terms in the energy and charge balance. In particular, the absorptivity was taken constant and equal to one above the band gap to obtain a solvable expression. Here, the absorptivity is computed

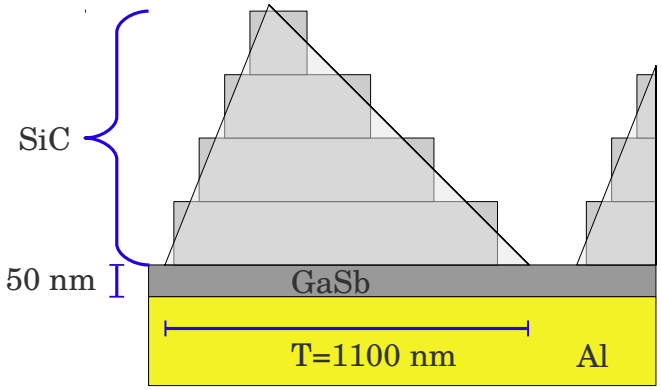

Figure 5.5: Dielectric structure designed for absorption enhancement in a 50 nm thick GaSb layer on a silver back reflector.

in very specific conditions (section 5.1). No analytical expression can be obtained for the absorbed and emitted power and another approach is necessary.

Equations 2.22 are still valid for the charge and energy balance, adding in it the power lost by thermalization in the absorber, that is a function of the carrier temperature $P_{th}(T_H)$:

$$\begin{cases} J_e^+(\mu_e, T_e) - J_e^-(\mu_n, T) = J_h^+(\mu_h, T_h) - J_h^-(\mu_p, T) \\ \qquad\qquad\qquad\qquad\qquad\quad = J_{abs} - J_{em}(\Delta\mu_H, T_H) \\ P_e^+(\mu_e, T_e) - P_e^-(\mu_n, T) + P_h^+(\mu_h, T_h) - P_h^-(\mu_p, T) \\ \qquad\qquad\qquad\qquad\qquad\quad = P_{abs} - P_{em}(\Delta\mu_H, T_H) - P_{th}(T_H) \end{cases} \tag{5.3}$$

The hypotheses of symmetrical valence and conduction bands are conserved, so the problem can be expressed with only three variables:

- $\Delta\mu_H = \frac{\mu_e}{2} = -\frac{\mu_h}{2}$
- $V = \frac{\mu_n}{2q} = -\frac{\mu_p}{2q}$
- $T_H = T_e = T_h$

For a given ouput voltage V and the ambient temperature being 300 K, the problem is simply the search of the zero of two functions F and G of $\Delta\mu_H$ and T_H:

$$\begin{cases} F(\Delta\mu_H, T_H) = J_{abs} - J_{em}(\Delta\mu_H, T_H) - \left(J_e^+(\Delta\mu_H/2, T_H) - J_e^-(qV/2, T)\right) \\ G(\Delta\mu_H, T_H) = P_{abs} - P_{em}(\Delta\mu_H, T_H) - P_{th}(T_H) \\ \qquad\qquad - 2\left(P_e^+(\Delta\mu_H/2, T_H) - P_e^-(qV/2, T)\right) \end{cases} \tag{5.4}$$

Physically, the unicity of the $(\Delta\mu_H, T_H)$ couple that cancels out both fonctions at a given value of V is ensured: the external voltage being fixed, only one stable state can exist for the system. Once the solution is found, the determination of the current is straightforward using the charge balance equation in system 5.4. The losses in the absorber are given by $P_{th}(T_H)$, and the losses in the contacts are given by the difference between the power that crosses the contacts and the electrical power delivered:

$$P_{contact}(\Delta\mu_H, T_H) = 2\left(P_e^+(\Delta\mu_H/2, T_H) - P_e^-(qV/2, T)\right) - J \times V \tag{5.5}$$

5.2.2 Validation

This method can be compared with the analytical problem described in 2.2.2. Considering a constant absorptivity (equal to 1), the results can be compared in the same conditions of thermalization and carrier extraction. The results obtained in the limit case of an ideal hot carrier solar cell (negligible thermalization and perfectly selective contacts) given by the two different models can be compared (see figure 5.6), showing very good agreement except for very small band gaps (below 0.5 eV).

Both models give the same efficiency and losses for band gaps higher than 0.5 eV, which is also the efficiency and losses given by the Ross-Nozik model for ideal hot carrier solar cells. This guarantees the accuracy of the method. For band gaps below 0.5 eV, the approximation of a Maxwell-Boltzmann distribution for carriers that is made in the analytical model is not valid, and a numerical solution should give more accurate results.

In the case of a fully thermalized cell, the efficiency is difficult to obtain by the numerical method. In particular, variables $\Delta\mu_H$ and T_H that are considered to determine the I-V characteristics are not relevant in that case. The problem being ill-defined, the results are unphysical.

5.2.3 Achievable efficiency

The efficiency of a solar cell with 0.65 eV band gap (GaSb), with the absorptivity determined from simulation on the structure described in figure 5.1 and with the thermalization rate measured in section 3.4 can then be computed with different configuration of the contacts: extraction energy, selectivity; and with varying concentration. PL experiments indicate a minimal thermalization coefficient at ambient temperature of 80 $W.K^{-1}.cm^{-2}$. This value will be taken as a reference.

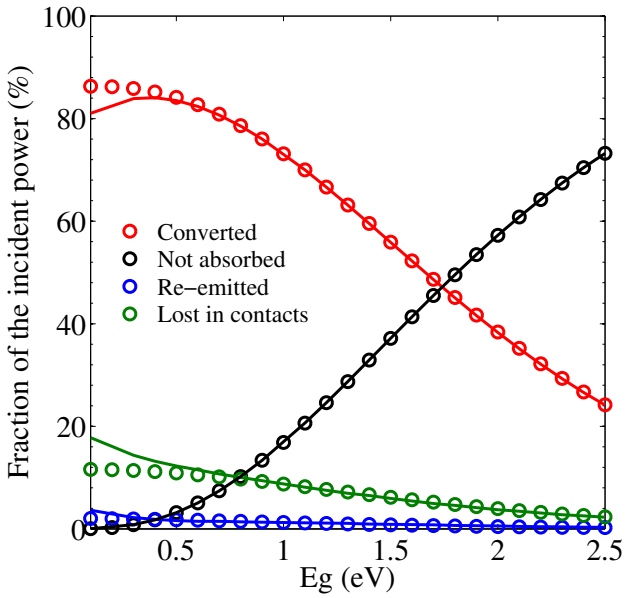

Figure 5.6: Efficiency and losses of an ideal hot carrier solar cell as a function of its band gap, given by the analytical model in chapter 2 (empty circles) compared with the results obtained by numerical resolution. Very good agreement is found, except for band gaps below 0.5 eV. The discrepancy at small band gaps is due to the Boltzman distribution approximation in the analytical model that is no longer valid.

The two limit cases of perfectly selective and semi-selective contacts are first considered. The optimal extraction energy and contact conductance are determined, and the efficiency is calculated. Results for these two cases are represented in figure 5.7.

In this figure, the efficiency of a hot carrier solar cell is plotted as a function of its band gap, with different values of the thermalization rate, from an ideal cell to a fully thermalized cell (solid lines). The position of the GaSb-based samples in the efficiency-band gap plane is represented by the circles and squares. The filled symbols correspond to a perfectly selective contact case, and the empty symbols to a semi-selective contact case. The circles correspond to an absorber with a thermalization coefficient $Q = 80$ W/K/cm^2, and the simulated efficiency is 26.3% with perfectly slective contacts, and 24.5% with semi-selective contacts.

The thermalization coefficient $Q = 80$ W/K/cm^2 was determined from PL ex-

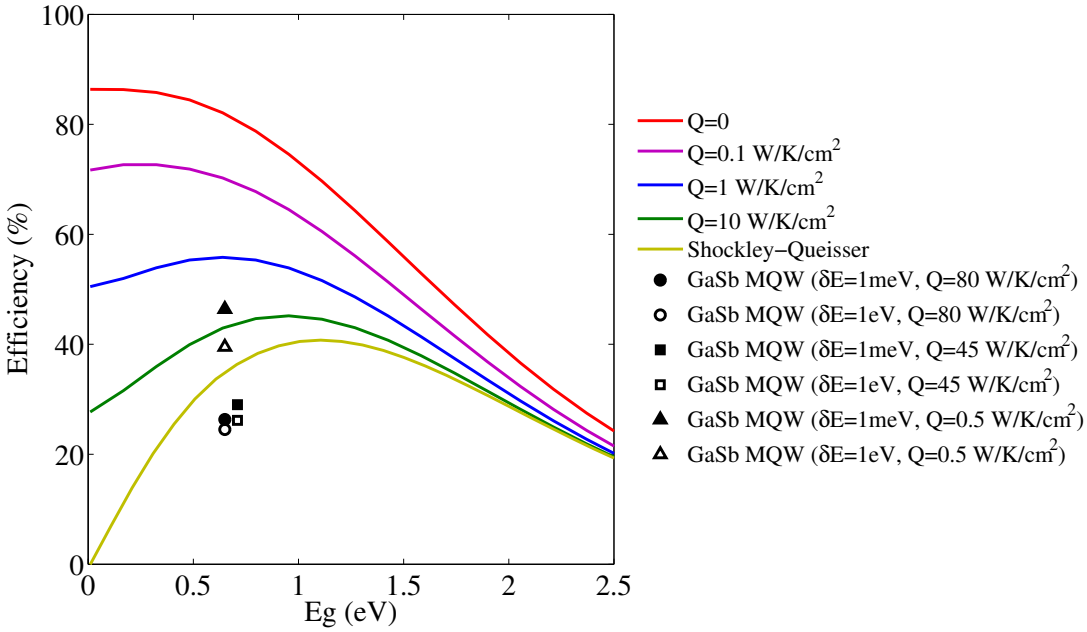

Figure 5.7: Efficiency of hot carrier solar cells with different thermalization rates for the absorber. Solid lines correspond to ideal absorptivity and selective contacts, with different thermalization coefficient, from negligible thermalization (red) to a fully thermalized cell (light green). Filled symbols represent a GaSb absorber with absorptivity determined in section 5.1 and perfectly selective contacts. Empty symbols represent similar absorbers with semi-selective contacts. Three different thermalization coefficients are considered: 80 (circles), 45 (squares) and 0.5 W/K/cm^2 (triangles).

periments on MQW samples without a resonant structure for absorption enhancement. With a dielectric grating grown on top of the surface, a better absorption can be achieved, which would result in a higher carrier density, thus in a reduced energy loss rate. If 76% absorption enhancement can be achieved , then a 43% energy loss rate reduction can be expected ($1/1.76 = 0.57 = 1 - 0.43$). One can then estimate that, in similar conditions of excitation, the GaSb absorber capped by a dielectric grating would have a thermalization coefficient $Q = 80(1 - 0.43) = 45$ W/K/cm^2. This situation is represented by the squares, with a simulated efficiency of 29.0% with perfectly selective contacts and 26.1% with semi-selective contacts.

The efficiencies reported here are below the Shockley-Queisser limit. This

comes from the fact that only 66% of the incident power is absorbed by the cell, while perfect absorption is considered in the Shockley-Queisser limit, which leads to an absorbed power that is 95% of the incident power. The efficiency of a conventional solar cell, without hot carrier effect, can be determined with the same absorptivity as in section 5.1. Only 18.9% efficiency can be obtained in these conditions, so a predicted efficiency of 26% is a 37% improvement compared to a conventional cell.

Finally, the efficiency of a cell having the same properties (band gap, absorptivity, contacts) but with a reduced thermalization coefficient $Q = 0.5$ W/K/cm^2 is represented by triangles. An efficiency of 46% is obtained with perfectly selective contacts. This shows that, in these conditions of concentration, for a targeted efficiency above 50%, at least two orders of magnitude have to be gained on the thermalization rate. The situation is even more unfavourable at lower concentration (slighlty compensated by a better absorptivity). At 10000 suns, the efficiency is comparable to the full concentration case when the thermalization rate is large. However, it requires a thermalization coefficient $Q = 0.1$ W/K/cm^2 to reach 50%.

5.3 A roadmap to 50% efficiency

5.3.1 Control of thermalization

It was stated in chapter 4 that the thermalization rate that were determined from continuous wave photoluminescence on GaSb-based samples were too large for a strong efficiency improvement to be obtained. Only a 26% improvement on the efficiency limit could be expected compared to the fully thermalized case in full concentration condition. The thermalization rate has to be reduced further to achieve a substantial breakthrough in the solar cell conversion efficiency.

In particular, the phonon dynamics can be modified by nanostructuring the material, which should affect the carrier energy loss rate. Quantum wells samples were synthesized in which a reduction of the energy loss rate was expected. However, the material compositions and thicknesses were not optimized, and no measurable effect was obtained. Improving the experimental method is necessary to get a more reliable and accurate measurement of the thermalization rate. More important, an optimal material composition and structure can be found using simulation tools that could help to synthesize better samples.

The phonon density of states can be studied in nanostructures using *ab initio* simulations. The time evolution of these phonon modes can then be simulated by molecular dynamics, knowing the anharmonic terms in the system hamiltonian.

This method is in current development, and shows promising results. Bulk properties such as phonon lifetimes were found in agreement with available experimental data. By studying the influence of the dimensionality (dots, wires, wells), the composition (silicon, III-V...) and the size of the nanostructures on the phonon lifetime, an optimal structure could be determined. Early results indicates a LO phonon lifetime that is doubled in Si-Ge nanostructures (dots) compared to bulk. Other materials with a larger mass contrast (InN, InP) are expected to exhibit a longer LO phonon lifetime.

By coupling this model for the phonon dynamics to a Monte-Carlo simulation of the carrier dynamics that takes into account electron-phonon interaction, it would be possible to simulate the whole electron-phonon system under continuous excitation. The establishment of a coupled non equilibrium carrier-LO phonon system can be studied when the excitation intensity is increased. Other effects such as Auger recombinations, impact ionization can be included in such model, which enables to simulate the real electron and hole distribution function in an operating hot carrier solar cell. Such information could then be used in a hot carrier solar cell model to predict its efficiency.

5.3.2 Carrier extraction

Results of chapter 2 indicate that semi-selective contacts are more suitable than highly selective contacts to have a working hot carrier solar cell, especially in high concentration regime. Highly selective contacts only provide a small efficiency enhancement, while they add drastic constraints on the contact conductivity.

A rather simple architecture was already proposed in this chapter, with large band gaps materials sandwiching the absorber working as electron (hole) semi-selective contact and hole (electron) blocking layer (see figure 2.8) could provide a substantial efficiency improvement, provided thermalization losses can be controlled. Extraction of unthermalized carriers should not be a major issue.

5.3.3 Cell design and synthesis

Once a convenient structure that would give optimal thermalization properties is defined, a prototype can be synthesized. Considering the thermalization rate, the optimal extraction energy can be determined by simulating the hot carrier solar cell efficiency, from which convenient materials for the electron and hole contacts can be identified. The resulting stack, grown by MBE, is then reported on a metallic substrate that acts as a back reflector and rear contact, and the substrate is removed. A resonant structure is then grown on the front surface. It is composed

of a dielectric grating, with a fill factor inferior to one. A metallic grid could then be evaporated on the uncovered surface of the sample as a front contact. Another solution would be to use a transparent conductive oxide as a resonant structure instead of an insulator, that would directly collect the charges. The front grid has to be designed for the large current density involved. A complete cell is finally obtained, that can be tested.

5.4 Conclusion

The achievable efficiency of a hot carrier solar cell in practical conditions was discussed here. Considering a simulated absorption and a thermalization rate determined from photoluminescence experiments, the cell behaviour accounting for different losses such as non absorption, heat losses in the absorber and heat losses in the contacts was simulated and the cell efficiency was computed.

The 26% predicted achievable efficiency is much below the limit of efficiency of ideal hot carrier solar cells, and does not exceed the efficiency of best existing single junction solar cells [4]. The main issue is the heat loss in the absorber that is too important to get a substantial efficiency enhancement. In order to approach the 50% efficiency target, it is necessary to drastically reduce the thermalization rate in the absorber. The limited absorption in an ultra thin layer, even using inovative photon management techniques, is also responsible for important losses that limit the conversion efficiency. A compromise has to be found on the absorber thickness between the reduction of the cooling rate and the losses due to non absorption of the incident power.

Provided a material structure is found where the thermalization rate is reduced, a method for the design and synthesis of a hot carrier solar cell prototype is proposed.

Bibliography

[1] R. Esteban, M. Laroche, and JJ. Greffet. Dielectric gratings for wide-angle, broadband absorption by thin film photovoltaic cells. *Appl. Phys. Lett.*, 2010.

[2] J.D. Jackson. *Classical electrodynamics*. John Wiley & Sons, Inc., 1999.

[3] R. Ferrini, M. Patrini, and S. Franchi. Optical functions from 0.02 to 6 eV of AlGaSb/GaSb epitaxial layers. *Journal of Applied Physics*, 84:4517, 1998.

[4] M.A. Green, K. Emery, Y. Hishikawa, and W. Warta. Solar cell efficiency tables (version 37). *Prog. Photovolt: Res. Appl.*, 19:84 – 92, 2011.

Conclusion

Main results

Several major results have been obtained. First of all, the role of contact selectivity on the cell efficiency has been investigated for the first time. It appears that, contrary to what was commonly admitted, a very high selectivity of the contacts is actually not crucial. Efficiency of 60% was obtained with semi-selective contacts allowing carrier transmission above an energy threshold, under full concentration and with negligible thermalization. It is lower than the 73% efficiency obtained with ideal contacts in the same conditions, but is still a 50% relative efficiency improvement compared to the Shockley-Queisser limit. Such a high pass filter can be obtained with a bulk large band gap layer, and may be much easier to fabricate than selective contacts using discrete levels (defects, quantum dot arrays) or tunnel junction, that proved themselves technologically challenging and incompatible with large current densities.

The question of contact conductivity is the second major limitation regarding selective contacts. The different ideas proposed to achieve carrier selectivity for contacts all involve tunneling, which would not favor large current densities expected for a device working under high concentration. It was pointed out that the contact conductivity decreases with the transmission range. Highly selective contacts would then strongly limit the extracted current, and would not be compatible with high conversion efficiencies. This is another argument in favor of semi-selective contacts.

The phenomenon of carrier thermalization has also been investigated experimentally. Contrary to previous studies where time-resolved experiments were performed to investigate the carrier thermalization properties, continuous wave photoluminescence was here preferred to match in a more relevant way the operating conditions of a solar cell. A hot carrier population was demonstrated under continuous excitation, and carrier temperatures exceeding the lattice temperature by a few hundreds of Kelvin was observed under excitation power densities corre-

sponding to 10,000 suns.

An empirical model for the power transfer from carriers to the lattice is proposed, fitted to experimental data, and heat losses are considered in the device energy balance. Results indicate that thermalization in the samples under investigation is rather fast, so they would only give a small, but still sizeable efficiency improvement compared to a conventional single junction. 26% conversion efficiency is simulated, which does not exceed the efficiency of best single junction solar cells today, but sill represents a 37% relative improvement compared to the single junction limit for the same band gap. A strong potential efficiency improvement can be expected if the thermalization rate can be reduced. Solutions are proposed regarding light trapping that may reduce the carrier cooling rate and improve the efficiency.

Perspectives

Considering a simplified structure with semi-selective contacts, a complete device can be obtained and tested rapidly. The heigth of the potential barrier for electron and hole contacts will have to be optimized though. The optimal extraction energy depends on the thermalization rate and on the concentration ratio. The hot carrier solar cell model proposed here can be used for that purpose. However, it would only give a rough estimation of this optimal extraction energy. In particular, this model treats electrons and holes symmetrically. One can expect a faster thermalization for holes, so the hole barrier may have to be lower, perhaps not selective at all. A more comprehensive model would be necessary for a better estimation of these parameters.

The structure and the composition of the absorber itself may also have to be optimized. If the carrier thermalization rate could be reduced by one order of magnitude, ten points could be gained on the cell efficiency. This could be done by phononic engineering, where the phonon dispersion relation is modified by nanostructuring the material, which can strongly affect the carrier energy loss process.

The carrier thermalization can also be tackled by increasing the carrier density in a very small material volume. Very efficient absorption of a highly concentrated incident light (close to 70% of the incident power) in a strongly reduced material thickness (25 to 50 nm) was simulated and an experimental validation is needed.

Appendix A

Band gaps of III-V multinary compounds

Here, the band gaps of III-V multinary compounds are determined as a function of the lattice temperature using data for the different binary compounds that can be found in [1]. Details are given for the well, barrier and cladding materials in sample V725, but the method can be applied for any compound.

First, the expected value of the well ($Ga_{0.86}In_{0.14}As_{0.12}Sb_{0.88}$) band gap and barrier ($Al_{0.25}Ga_{0.75}As_{0.03}Sb_{0.97}$) band gap at 80 K can be predicted by interpolating the known band gap of the binary compounds GaSb, GaAs, InAs, and InSb. These values are obtained as a function of the lattice temperature T in Kelvin and follow a law of the form [1]:

$$E_g(T) = E_g(T = 0\ K) - \frac{\alpha T^2}{T + \beta} \tag{A.1}$$

where α is a coefficient expressed in eV/K and β is a constant in K. The values of α and β for several III-V compounds are given in table A.1, as well as their band gap at 0 K, 80 K and 300 K.

The band gap of a ternary compound, composed of two binary compounds, is then a linear combination of the band gaps of these binary compounds, corrected by a bowing parameter. The same goes for quaternary compounds considering that it is composed of one ternary and one binary compound (see below for details). Standard values of these bowing parameters found in the litterature [1] are given in table A.2. The band gap of a material $A_xB_{1-x}C$ is then obtained as follows:

$$E_{g,A_xB_{1-x}C} = xE_{g,AC} + (1-x)E_{g,BC} - c \times x(1-x) \tag{A.2}$$

c being the bowing parameter for material $A_xB_{1-x}C$ in eV.

material	α^{Γ} (mev/K)	β^{Γ} (K)	E_g^{Γ} (eV)		
			T=0 K	T=80 K	300 K
GaAs	0.5405	204	1.519	1.51	1.42
GaSb	0.417	140	0.812	0.80	0.73
InAs	0.276	93	0.417	0.41	0.39
InSb	0.32	170	0.235	0.23	0.17
AlAs	0.885	530	3.10	3.10	3.00
AlSb	0.42	140	2.386	2.37	2.30

Table A.1: Band structure parameters of different binary III-V compounds and their band gap at 0 K, 80 K, 300 K. In the case of AlSb and AlAs, which have indirect band gaps, the value E_g^{Γ} that is given corresponds to the energy difference between conduction band and valence band at the Γ point of the brillouin zone, and not to the indirect band gap of the material.

Compound	Bowing parameters (eV)	
	on E_g	on Δ_{so}
$InAs_{0.91}Sb_{0.09}$	0.67	1.2
$AlAs_{0.08}Sb_{0.92}$	0.8	0.15
$(GaSb)_{0.86}(InAs_{0.91}Sb_{0.09})_{0.14}$	0.75	0.25
$(GaSb)_{0.75}(AlAs_{0.08}Sb_{0.92})_{0.25}$	0.48	-
$(GaSb)_{0.1}(AlAs_{0.08}Sb_{0.92})_{0.9}$	0.48	-

Table A.2: Bowing parameters for determining the band gap and the spin orbit splitting of different ternary and quaternary compounds.

The band gap of GaSb-lattice-matched GaInAsSb can be derived from GaSb and $InAs_{0.91}Sb_{0.09}$ band gaps considering the alloy $(GaSb)_{1-z}(InAs_{0.91}Sb_{0.09})_z$, with a bowing parameter $c_1 = 0.75$ eV (table A.2). The band gap for the well compound

Compound	E_g (eV)		
	T=0 K	T=80 K	T=300 K
$InAs_{0.91}Sb_{0.09}$	0.34	0.34	0.32
$AlAs_{0.08}Sb_{0.92}$	2.38	2.37	2.30
$(GaSb)_{0.86}(InAs_{0.91}Sb_{0.09})_{0.14}$	0.66	0.65	0.58
$(GaSb)_{0.75}(AlAs_{0.08}Sb_{0.92})_{0.25}$	1.12	1.10	1.03
$(GaSb)_{0.1}(AlAs_{0.08}Sb_{0.92})_{0.9}$	2.18	2.17	2.10

Table A.3: Band gaps of different ternary and quaternary compounds at 0 K, 80 K and 300 K.

$Ga_{0.86}In_{0.14}As_{0.12}Sb_{0.88}$ at 80 K can then be obtained setting $z = 0.14$:

$$\begin{aligned} E_{g,well} &= (1-z) \times E_{g,\mathrm{GaSb}} + z \times E_{g,\mathrm{InAs_{0.91}Sb_{0.09}}} - c_1 \times z(1-z) \\ &= 0.65 \text{ eV} \end{aligned} \tag{A.3}$$

Similarly, the band gap for GaSb-lattice-matched AlGaAsSb can be derived from GaSb and $AlAs_{0.08}Sb_{0.92}$ band gaps considering the alloy of a binary and ternary GaSb-lattice-matched compound $(GaSb)_{1-z}(AlAs_{0.08}Sb_{0.92})_z$, with a bowing parameter $c_2 = 0.48$ eV. The band gap for the quaternary barrier compound $Al_{0.25}Ga_{0.75}As_{0.03}Sb_{0.97}$ is obtained setting $z = 0.25$:

$$\begin{aligned} E_{g,barrier} &= (1-z) \times E_{g,\mathrm{GaSb}} + z \times E_{g,\mathrm{AlAs_{0.08}Sb_{0.92}}} - c_2 \times z(1-z) \\ &= 1.10 \text{ eV} \end{aligned} \tag{A.4}$$

Finally, the band gap of the cladding layer $Al_{0.9}Ga_{0.1}As_{0.07}Sb_{0.93}$ is obtained setting $z = 0.9$ eV:

$$\begin{aligned} E_{g,barrier} &= (1-z) \times E_{g,\mathrm{GaSb}} + z \times E_{g,\mathrm{AlAs_{0.08}Sb_{0.92}}} - c_2 \times z(1-z) \\ &= 2.17 \text{ eV} \end{aligned} \tag{A.5}$$

The values obtained at 0 K, 80 K and 300 K are compiled in table A.3. These are the band gaps of the bulk materials. The position of the electron and hole states in quantum well structures have to be calculated, using a finite potential well model [2]. Effective masses in those quaternary compounds are necessary.

They are determined by the same method as for the band gap and derived from the effective masses of the binary compounds.

The electron effective masses at the Γ point m_e^* are defined by the following expression [1]:

$$\frac{m_0}{m_e^*} = (1+2F) + \frac{E_P(E_g + 2\Delta_{so}/3)}{E_g(E_g+\Delta_{so})} \tag{A.6}$$

where m_0 is the electron mass, E_P is a matrix element between an s-like conduction band and a p-like valence band, F is the Kane parameter that parametrizes higher-band contribution to the conduction band, and Δ_{so} is the spin-orbit splitting. These parameters are considered independant of the temperature, so the temperature dependance of the electron effective mass arises only through the temperature dependance of the band gap E_g.

The heavy hole effective masses in the different crystallographic orientation [100], [110] and [111] are given by:

$$\left(\frac{m_0}{m_{hh}^*}\right)^{[100]} = \gamma_1 - 2\gamma_2 \tag{A.7}$$

$$\left(\frac{m_0}{m_{hh}^*}\right)^{[110]} = \frac{1}{2}(2\gamma_1 - \gamma_2 - 3\gamma_3) \tag{A.8}$$

$$\left(\frac{m_0}{m_{hh}^*}\right)^{[111]} = \gamma_1 - 2\gamma_3 \tag{A.9}$$

where γ_1, γ_2 and γ_3 are the Luttinger parameters.

Similarly for light holes:

$$\left(\frac{m_0}{m_{lh}^*}\right)^{[100]} = \gamma_1 + 2\gamma_2 \tag{A.10}$$

$$\left(\frac{m_0}{m_{lh}^*}\right)^{[110]} = \frac{1}{2}(2\gamma_1 + \gamma_2 + 3\gamma_3) \tag{A.11}$$

$$\left(\frac{m_0}{m_{lh}^*}\right)^{[111]} = \gamma_1 + 2\gamma_3 \tag{A.12}$$

Finally, the split-off hole effective mass is:

$$\frac{m_0}{m_{so}^*} = \gamma_1 - \frac{E_P\Delta_{so}}{3E_g(E_g+\Delta_{so})} \tag{A.13}$$

The values of F, E_P, Δ_{so}, γ_1, γ_2 and γ_3 that determine the effective masses in common binary compounds, and the obtained effective masses are compiled in

table A.4. Only hole effective masses in the [100] direction corresponding to the well orientation is reported here. The electron effective mass is given at 80 K, and all effective masses are given at the Γ point (including for the indirect band gap material AlSb and AlAs).

Parameter	GaAs	GaSb	InAs	InSb	AlAs	AlSb
F	-1.94	-1.63	-2.90	-0.23	-0.48	-0.56
E_P (eV)	28.8	27.0	21.5	23.3	21.1	18.7
Δ_{so} (eV)	0.341	0.76	0.39	0.81	0.28	0.676
γ_1	6.98	13.4	20.0	34.8	3.76	5.18
γ_2	2.06	4.7	8.5	15.5	0.82	1.19
γ_3	2.93	6.0	9.2	16.5	1.42	1.97
m_e^*	0.067	0.038	0.026	0.013	0.150	0.139
m_{hh}^*	0.350	0.250	0.333	0.263	0.472	0.357
m_{lh}^*	0.090	0.044	0.027	0.015	0.185	0.132
m_{so}^*	0.172	0.126	0.087	0.118	0.280	0.218

Table A.4: Band parameters of common III-V compounds. Effective masses are given at 80 K and at the Γ point.

The method to determine the ternary and quaternary effective masses is then to:

- interpolate linearly the F and E_p parameters
- use the bowing parameter specified in table A.2 for the alloy to derive E_g and Δ_{so}
- obtain the temperature-dependent electron effective mass from equation A.6

Linear interpolations are possible to determine heavy hole and light hole effective masses in the [100] direction. In other directions, an interpolation on the difference $\gamma_3 - \gamma_2$ rather than a direct interpolation of the Luttinger parameter is recommanded [1]. The results for ternary and quaternary compounds are compiled in table A.5.

Finally, the conduction and valence band offsets between wells and barriers are required. The valence band offset (VBO) in heterojunction can be reasonably ap-

Compound	F	E_p (eV)	Δ_{so} (eV)	m_e^*	m_{hh}^*	m_{lh}^*
$InAs_{0.91}Sb_{0.09}$	-2.66	21.7	0.33	0.020	0.327	0.026
$AlAs_{0.08}Sb_{0.92}$	-0.55	18.9	0.63	0.137	0.366	0.136
well	-1.77	26.3	0.67	0.032	0.261	0.042
barrier	-1.36	25.0	0.73	0.056	0.279	0.067
cladding	-0.66	19.7	0.64	0.124	0.354	0.127

Table A.5: Band parameters and effective masses of different ternary and quaternary compounds at 80 K.

proximated by the bulk valence band position of each idividual material [1]. Also, the valence band offset will be considered independent of the temperature. The conduction band offset (CBO) is then directly determined knowing the material band gap. Taking the barrier valence band position as reference, the position of the well and barrier valence and conduction bands are reported in table A.6. The energy of the fundamental electronic state to the fundamental hole state transition e1hh1 is also reported.

Temperature		well	barrier	cladding	e1hh1 (eV)
T=0 K	VBO (eV)	0.07	0	-0.26	0.715
	CBO (eV)	0.73	1.12	1.92	
T=80 K	VBO (eV)	0.07	0	-0.26	0.704
	CBO (eV)	0.72	1.10	1.91	
T=300 K	VBO (eV)	0.07	0	-0.26	0.637
	CBO (eV)	0.65	1.03	1.84	

Table A.6: Band offsets of the well, barrier and cladding in the V725 sample at 0 K, 80 K, and 300 K. Electron and hole states are determined using these band offsets and effective masses in table A.5. The fundamental transition e1hh1 is reported here.

Bibliography

[1] I. Vurgaftman, J. R. Meyer, and L. R. Ram-Mohan. Band parameters for III-V compound semiconductors and their alloys. *Journ. Appl. Phys.*, 89:5815, 2001.

[2] C. Weisbuch and B. Vinter. *Quantum semiconductor structures, fundamentals and applications*. Academic Press, 1991.

Appendix B

Propagation of light in a layered medium

The absorption of the incident light in the experimental section was determined using a transfer matrix approach. The sample is described as a stack of parallel layers, each layer being charaterized by a wavelength dependent refractive index and absorbtion coefficient, and the propagation of a plane wave is simulated for a given wavelength and incident angle.

Let us consider a plane interface between medium 1 and medium 2, and an electromagnetic plane wave with wavelength λ propagating in medium 1 and hitting the interface with incident angle θ. The amplitude of the electric field of the incident wave is E_1^i. The amplitude of the reflected wave is E_1^r, and the amplitude of the transmitted wave in medium 2 is E_2^t. The reflection and transmission coefficients $R_{1,2}$ and $T_{1,2}$ are defined by [1]:

$$r_{1,2} = \frac{E_1^r}{E_1^i} = \frac{n_1 \cos(\theta) - \sqrt{n_2^2 - n_1^2 \sin(\theta)}}{n_1 \cos(\theta) + \sqrt{n_2^2 - n_1^2 \sin(\theta)}} \tag{B.1}$$

$$t_{1,2} = \frac{E_2^t}{E_1^i} = \frac{2n_1 \cos(\theta)}{n_1 \cos(\theta) + \sqrt{n_2^2 - n_1^2 \sin(\theta)}} \tag{B.2}$$

for the s polarization (electric field perpendicular to the plane of incidence), and

$$r_{1,2} = \frac{E_1^r}{E_1^i} = \frac{n_2^2 \cos(\theta) - n_1 \sqrt{n_2^2 - n_1^2 \sin(\theta)}}{n_2^2 \cos(\theta) + n_1 \sqrt{n_2^2 - n_1^2 \sin(\theta)}} \tag{B.3}$$

$$t_{1,2} = \frac{E_2^t}{E_1^i} = \frac{2n_1 n_2 \cos(\theta)}{n_2^2 \cos(\theta) + n_1 \sqrt{n_2^2 - n_1^2 \sin(\theta)}} \tag{B.4}$$

for the p polarization (electric field parallel to the plane of incidence), where n_1 nad n_2 are the complex refractive index in media 1 and 2 respectively.

At the interface, the component of the wave vector of the reflected and transmitted waves that is parallel to the interface is conserved. In the case of multiple interfaces, all the waves (incident, reflected and transmitted) propagating in the multilayer share this same component of the wave vector. The problem can then be treated as a one dimensional problem and the light propagating in medium i can be described as one electromagnetic wave propagating in the direction of the x axis, with wave vector $k_{x_i} = \dfrac{2\pi n_i}{\lambda}\cos\theta_i$, and amplitude of the electric field E_i^+, and one propagating in the opposite direction with wave vector $-k_{x_i}$ and amplitude of the electric field E_i^- [2]. θ_i is the angle between the normal to the parallel interfaces and the direction of propagation, and is obtained by Snell's law.

The following relations then apply between the amplitudes of the wave in media i and $i+1$, considering the reflection and transmission coefficients defined above:

$$\begin{aligned} E_{i+1,i}^+ &= t_{i,i+1}E_{i,i}^+ + r_{i+1,i}E_{i+1,i}^- \\ E_{i,i}^- &= t_{i+1,i}E_{i+1,i}^- + r_{i,i+1}E_{i,i}^+ \end{aligned} \tag{B.5}$$

where, in $E_{j,k}$, index j refers to the medium and index k refers to the interface.

One can then define a matrix M_i for interface i, so that the amplitudes in media $i+1$ at interface i are given by the product of matrix M_i by the amplitudes in media i at interface i:

$$\underbrace{\begin{pmatrix} E_{i+1,i}^+ \\ E_{i+1,i}^- \end{pmatrix}}_{E_{i+1}} = \underbrace{\begin{pmatrix} m_{i,11} & m_{i,12} \\ m_{i,21} & m_{i,22} \end{pmatrix}}_{M_i} \underbrace{\begin{pmatrix} E_{i,i}^+ \\ E_{i,i}^- \end{pmatrix}}_{E_i} \tag{B.6}$$

with:

$$\begin{aligned} m_{i,11} &= t_{1,2} - \frac{r_{1,2}r_{2,1}}{t_{2,1}} \\ m_{i,12} &= \frac{r_{2,1}}{t_{2,1}} \\ m_{i,21} &= -\frac{r_{1,2}}{t_{2,1}} \\ m_{i_2 2} &= \frac{1}{t_{2,1}} \end{aligned} \tag{B.7}$$

The amplitudes in media $i+1$ at interface $i+1$ are then related to the amplitudes in media $i+1$ at interface i by:

$$\begin{aligned} E_{i+1,i+1}^+ &= \exp\left(k_{x_{i+1}}d_{i+1}\right)\exp\left(-\alpha_{i+1}d_{i+1}\right)E_{i+1,i}^+ \\ E_{i+1,i+1}^- &= \exp\left(-k_{x_{i+1}}d_{i+1}\right)\exp\left(\alpha_{i+1}d_{i+1}\right)E_{i+1,i}^- \end{aligned} \tag{B.8}$$

where α_{i+1} is the absorption coefficient in medium $i+1$, and d_{i+1} is the optical thickness of layer $i+1$ equal to $t_i/\cos\theta_i$ where t_i is the actual thickness. Writing $E_i = E_{i,i}$ the amplitudes in medium i at interface i, one can write:

$$E_{i+1} = N_i \times E_i \tag{B.9}$$

where

$$N_i = \begin{pmatrix} \exp(-\alpha_{i+1} d_{i+1}) & 0 \\ 0 & \exp(\alpha_{i+1} d_{i+1}) \end{pmatrix} \times M_i \tag{B.10}$$

Finally, the amplitudes in any layer can be expressed as a function of the amplitudes in any other layer by a product of the matrices N_i. In particular, one can relate the amplitudes of the waves that are reflected and transmitted by the whole stack E_r and E_t as a function of the amplitude of the incident wave E_i:

$$\begin{pmatrix} E_t \\ 0 \end{pmatrix} = \underbrace{\prod_i N_i}_{N} \times \begin{pmatrix} E_i \\ E_r \end{pmatrix} = N \times \begin{pmatrix} E_i \\ E_r \end{pmatrix} \tag{B.11}$$

assuming there is no light coming from the back of the stack.

The total reflection and transmission coefficients are defined:

$$\begin{aligned} r^{s,p} &= \frac{E_r}{E_i} \\ t^{s,p} &= \frac{E_t}{E_i} \end{aligned} \tag{B.12}$$

for each polarization s or p. In the case of an unpolarized incident light, the reflection and transmission coefficient are $r = (r^s + r^p)/2$ and $t = (t^s + t^p)/2$. For an amplitude of the electric field E, the intensity is then $I = \frac{cn}{4\pi}\cos(\theta)\langle E\rangle^2$, c being the speed of light in vacuum, n the refractive index in the medium in which the light is propagating and θ the angle between the propagation direction and the normal to the interface. The reflection and transmission coefficients in energy are then defined:

$$R = r^2, \qquad T = \frac{n_s \cos(\theta_s)}{n_0 \cos(\theta_0)} t^2 \tag{B.13}$$

where n_0 is the refractive index of the medium from which the light is coming (in general air) and θ_0 is the incident angle, and n_s is the refractive index of the substrate and θ_s the angle of the transmitted beam with the normal.

These coefficient are functions of the incident angle θ and wavelength λ, because of the wavelength dependent refractive index and absorption coefficient. In the

case of a laser as the incident wave, one can consider a monochromatic wave and constant optical parameters are used. These parameters were found in [3]. The reflection and transmission coefficient are computed as a function of the incident angle.

An example of the result obtained with a 750 nm laser incident on sample V725 is presented in figure B.1, showing the transmitted (a), reflected (b) and absorbed (c) fraction of an incident plane wave as a function of the incident angle, for different polarization: s, p, and unpolarized.

Considering an incident beam coming from solid angle $\Omega = 2\pi(1 - \cos\theta)$ with power density P_0, the total reflected and transmitted power P_R and P_T are computed by integrating the energy reflection and transmission coefficient over incident angles:

$$P_R = 2\pi \int_0^\theta I_0 \sin(\theta') R(\theta') d\theta' \tag{B.14}$$

$$P_T = 2\pi \int_0^\theta I_0 \sin(\theta') T(\theta') d\theta' \tag{B.15}$$

where I_0 is the power density per solid angle unit, and is equal to P_0/Ω . The power absorbed P_A is then directly obtained:

$$P_A = P_0 - P_R - P_T \tag{B.16}$$

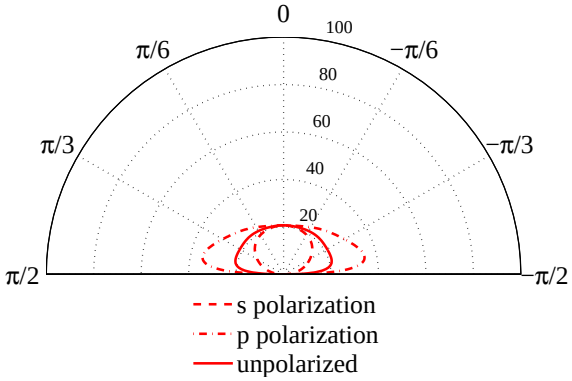

(a) Transmission

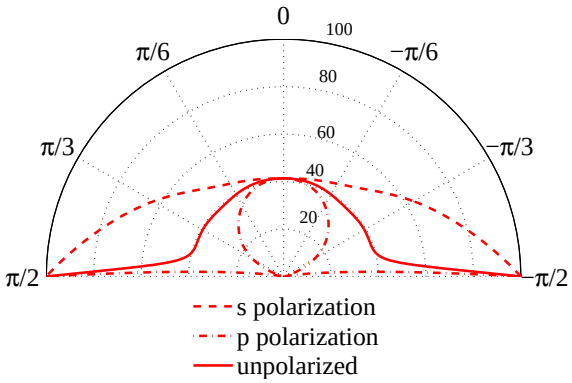

(b) Reflection

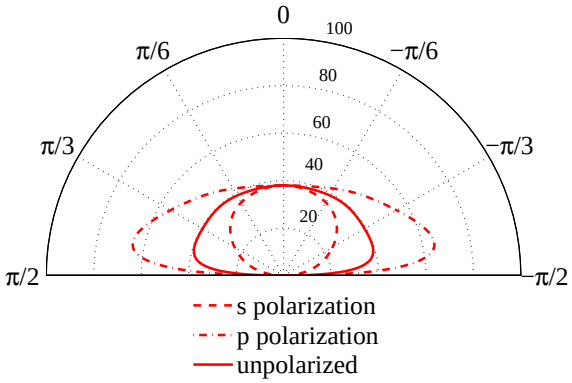

(c) Absorption

Figure B.1: Fraction (in %) of a plane wave intensity that is transmitted (a), reflected (b) and absorbed (c) by sample V725 as a function of its incident angle, for s-polarized, p-polarized and unpolarized incident light

Bibliography

[1] J.D. Jackson. *Classical electrodynamics*. John Wiley & Sons, Inc., 1999.

[2] M. Born and E. Wolf. *Principles of Optics: Electromagnetic Theory of Propagation, Interference and Diffraction of Light*. Pergamon Press Ltd, 1959.

[3] IOFFE. http://www.ioffe.ru/SVA/NSM/Semicond/.

Publications and conference communications

Reviewed publications:

1. A. Le Bris and J.-F. Guillemoles, Hot-carrier solar cells: achievable efficiency accounting for heat losses in the absorber and through contacts, *Appl. Phys. Lett.* **97**, 113506-113508 (2010)
2. A. Le Bris, L. Lombez, S. Laribi, G. Boissier, P. Christol and JF. Guillemoles, Thermalization rate study of GaSb-based heterostructures by continuous wave photoluminescence ad their potential as hot carrier solar cell absorbers, *Physical Review B*, submitted.
3. A. Le Bris, C. Colin, S. Collin, JL. Pelouard, R. Esteban, M. Laroche, JJ. Greffet and JF. Guillemoles, Hot carrier solar cells: controlling thermalization in ultra thin devices, *Journal of Photovoltaics*, submitted.

Book

1. JF. Guillemoles, S. Laribi, A. Le Bris, LM. Huang and P. Olsson, Phononic Engineering within the Hot Carrier Solar Cells, chapter 12 of the book: Advanced solar cell materials, technology, modelling and simulation, Editors: L. Fara and M. Yamaguchi, *in press*

Oral presentations:

1. A. Le Bris and JF. Guillemoles, Hot carrier solar cell efficiency simulation with realistic electronic contacts, *PV Technical Conference 2010 (Aix)*
2. A. Le Bris and JF. Guillemoles, Hot carrier solar cell efficiency simulation with carrier extraction through non ideal selective contacts, *35^{th} IEEE PV Specialists Conference 2010 (Hawai'i)*
3. M.A. Green, G.J. Conibeer, D. König, S. Shrestha, S. Huang, P. Aliberti, L. Treiber, R. Patterson, B. Puthen Veettil, A. Hsieh, A. Luque, A. Martí Vega, P. García-Linares, E. Cánovas, E. Antolín, D. Fuertes Marrón, C. Tablero,

E. Hernández, JF. Guillemoles, L. Huang, A. Le Bris, T.W. Schmidt, R. Clady, M.J.Y. Tayebjee, Recent progress with hot carrier solar cells, *25th EUPVSEC 2010 (Valence)*

4. JF. Guillemoles, A. Le Bris, L. Lombez, M. Paire, S. Laribi, D. Lincot, C. Colin, S. Collin, JL. Pelouard, M. Laroche, R.Esteban, JJ. Greffet, G. Boissier and P. Christol, Hot-Carrier solar cells, *SPIE 2011 (San Francisco)*
5. L. Hirst, M. Führer, A. Le Bris, JF. Guillemoles, M. Tayebjee, R. Clady, T. Schmidt, M. Sugiyama, Y. Wang and N.J. Ekins-Daukes, Quantum wells for hot carrier solar cells, *7th Photovoltaic Science Application and Technology Conference and Exhibition 2011 (Edimbourg)*
6. A. Le Bris, L. Lombez, S. Laribi, G. Boissier, P. Christol, R. Esteban, JJ. Greffet and JF. Guillemoles, A path to realization of hot carreir solar cells, *E-MRS 2011 Spring Meeting (Nice)*
7. A. Le Bris, L. Lombez, S. Laribi, C. Colin, S. Collin, JL. Pelouard, R.Esteban, JJ. Greffet, G. Boissier, P. Christol and JF. Guillemoles, Hot carrier solar cells: controlling thermalization in ultra thin devices, *37th IEEE PV Specialists Conference 2011 (Seattle)*
8. L. Hirst, M. Führer, A. Le Bris, JF. Guillemoles, M. Tayebjee, R. Clady, T. Schmidt, M. Sugiyama, Y. Wang and N.J. Ekins-Daukes, Hot carriers dynamics in InGaAs/GaAsP qunatum well solar cells, *37th IEEE PV Specialists Conference 2011 (Seattle)*

Visual presentations:

1. A. Le Bris, JF. Guillemoles, G. Boissier, P. Christol, S. Ivanova, P. Aschehoug, Hot carrier solar cell efficiency simulations with partial thermalization, *24th EUPVSEC 2009 (Hamburg)*
2. A. Le Bris, L. Lombez, JF. Guillemoles, R. Esteban, M. Laroche, JJ. Greffet, G. Boissier, P. Christol, S. Collin, JL. Pelouard, P. Aschehoug, F. Pellé, Hot carrier solar cells: in the making, *25th EUPVSEC 2010 (Valence)*

Proceedings:

1. A. Le Bris, JF. Guillemoles, G. Boissier, P. Christol, S. Ivanova, P. Aschehoug, Hot carrier solar cell efficiency simulations with partial thermalization, *EUPVSEC Proceedings (2009)*
2. A. Le Bris and JF. Guillemoles, Hot carrier solar cell efficiency simulation with carrier extraction through non ideal selective contacts, *IEEE PV Specialists Conference Proceedings (2010)*

3. A. Le Bris, L. Lombez, JF. Guillemoles, R. Esteban, M. Laroche, JJ. Greffet, G. Boissier, P. Christol, S. Collin, JL. Pelouard, P. Aschehoug, F. Pellé, Hot carrier solar cells: in the making, *EUPVSEC Proceedings (2010)*
4. JF. Guillemoles, A. Le Bris, L. Lombez, M. Paire, S. Laribi, D. Lincot, C. Colin, S. Collin, JL. Pelouard, M. Laroche, R.Esteban, JJ. Greffet, G. Boissier and P. Christol, Hot-Carrier solar cells, *SPIE Conference Proceedings (2011)*
5. M.A. Green, G.J. Conibeer, D. König, S. Shrestha, S. Huang, P. Aliberti, L. Treiber, R. Patterson, B. Puthen Veettil, A. Hsieh, A. Luque, A. Martí Vega, P. García-Linares, E. Cánovas, E. Antolín, D. Fuertes Marrón, C. Tablero, E. Hernández, JF. Guillemoles, L. Huang, A. Le Bris, T.W. Schmidt, R. Clady, M.J.Y. Tayebjee, Hot carrier solar cells: challenges and recent progress, *IEEE PV Specialists Conference Proceedings (2010)*